Study of Power System Disturbances

Thesis submitted by
Chandan Jana

Doctor of Philosophy (Engineering)

Department of Electrical Engineering
Faculty Council of Engineering & Technology
Jadavpur University
Kolkata, India

2025

JADAVPUR UNIVERSITY
FACULTY OF ENGINEERING AND TECHNOLOGY

INDEX NO. **261/23/E**

1. **Title of the Thesis**: Study of Power System Disturbances

2. **Name, Designation and Institution of the Supervisor/s:**

   (a) **Prof. (Dr.) Sovan Dalai**
   Professor, Department of Electrical Engineering,
   Jadavpur University, Kolkata –700032

3. **List of Publications:**

   (a) **Journals**

   i. C. Jana, S. Banerjee, S. Maur, and S. Dalai, "Customized CNN-based classification of power system disturbances using recurrence plots," Electric Power Systems Research, Elsevier, vol. 241, no. 111370, 2025.

   ii. C. Jana, S. Banerjee, S. Maur, and S. Dalai, "Mathematical morphology based sensing of power system disturbances using PCA aided support vector machine," IEEE Sensors Journal, vol. 24, no. 11, 2024.

   iii. C. Jana, S. Banerjee, S. Maur, and S. Dalai, "Power system disturbance classification using CWT-guided tailor-made AlexNet CNN," IEEE Sensors Letters, vol. 8, no. 6, 2024.

   iv. C. Jana, S. Banerjee, S. Maur, and S. Dalai, "Sensing of power system disturbances using CNN-aided tailored BiLSTM model," IEEE Sensors Journal, vol. 24, no. 21, 2024.

(b) **International Conferences**

i. C. Jana, S. Banerjee, S. Maur, and S. Dalai, "Wavelet-aided KNN based power system disturbances classification," IEEE International Conference ASPCON 2023.

4. **List of Patents:** Nil

5. **List of Presentations in National/International Conferences and Workshops:**

(a) C. Jana, S. Banerjee, S. Maur, and S. Dalai, "Wavelet-aided KNN based power system disturbances classification," IEEE International Conference ASPCON 2023.

JADAVPUR UNIVERSITY
FACULTY OF ENGINEERING AND TECHNOLOGY

STATEMENT OF ORIGINALITY

I, **Shri Chandan Jana** registered on **10th April, 2023**, do hereby declare that this thesis entitled **"Study of Power System Disturbances"** contains literature survey and original research work done by the undersigned candidate as part of Doctoral studies.

All information in this thesis have been obtained and presented in accordance with existing academic rules and ethical conduct. I declare that, as required by these rules and conduct, I have fully cited and referred all materials and results that are not original to this work.

I also declare that I have checked this thesis as per the Policy on Anti Plagiarism, Jadavpur University, 2019, and the level of similarity as checked by iThenticate software is 3%.

Chandan Jana.
Signature of the Candidate:

Date : 24.06.2025.

Certified by Supervisors:
(Signature with date, seal)

24.06.2025

(Prof. (Dr.) Sovan Dalai)

Dr. Sovan Dalai
Professor
Electrical Engineering Department
Jadavpur University
Kolkata-700032

JADAVPUR UNIVERSITY
FACULTY OF ENGINEERING AND
TECHNOLOGY

CERTIFICATE FROM THE SUPERVISOR/S

This is to certify that the thesis entitled **"Study of Power System Disturbances"** submitted by **Shri Chandan Jana**, who got his name registered on 10^{th} **April, 2023** for the award of **Ph.D. (Engg.)** degree of Jadavpur University is absolutely based upon his own work under the supervision of **Prof. (Dr.) Sovan Dalai** and that neither his thesis nor any part of the thesis has been submitted for any degree/diploma or any other academic award anywhere before.

24.06.2025

(Prof. (Dr.) Sovan Dalai)
Signature of the Supervisor
and date with Official seal

Dr. Sovan Dalai
Professor
Electrical Engineering Department
Jadavpur University
Kolkata-700032

. . . . . .

Dedicated

to

Baba and Maa

. . . . . .

Acknowledgements

The author expresses his sincere appreciation and deep gratitude to his esteemed guide, Prof. (Dr.) Sovan Dalai for his invaluable guidance and advice in carrying out the thesis work. The author was allowed to have the necessary freedom during his work, and at the same time, the intense supervision by the supervisor guided the work towards perfection. His untiring endeavour, unparalleled firmness of knowledge and vision, perpetual encouragement, and precious advice made the daunting task possible for the author.

The author expresses his deep sense of gratitude to the HOD of the Electrical Engineering Department, Jadavpur University, for his kind agreement in providing the necessary laboratory facilities for the implementation of this work.

It is the author's pleasure to acknowledge his respected teachers, Prof. Swapan Kr. Goswami and Prof. Sugata Munshi, his colleague, Dr. Sannistha Banerjee, and the PhD scholar, Dr. Subhajit Maur, for their advice, encouragement, and assistance in completing the research work.

The author is also grateful to the faculty members Dr. Biswendu Chatterjee and Dr. Debangshu Dey for their academic support and constructive suggestions, which have greatly enhanced the quality of this thesis.

The author is indebted to his mother, Smt. Saraswati Jana, wife, Dr. Mousumi Jana Bala, and daughter, Chalormi Jana, for providing much-needed emotional support, love, and, above all for encouragement.

The author would also like to express his heartfelt gratitude to all his family members for their never-ending support, love and blessings, without which it would have been impossible to complete the work.

A special thanks to fellow researchers and colleagues for their collaboration, discussions, and motivation during this journey. Their companionship made this endeavour more enriching and enjoyable.

This thesis is the result of the collective efforts of many, and I sincerely appreciate everyone who contributed to this journey in any way.

Chandan Jana
PhD Fellow, Jadavpur University

Abstract

From the early days of electrical power systems to today's systems, many infrastructural developments and policy-related rules and regulations have come into play. Accordingly, its operation, planning, monitoring and protection scheme have also been updated to meet the system requirements.

From manual to semi-automated, from semi-automated to fully automated system configuration has evolved and it took more than 140 years to get to its present state.

All three major sections in the power system– generation, transmission, and distribution—are advancing rapidly towards the smart digitized system. This helps power engineers monitor, control and protect the whole network very efficiently. Recently, researchers in the power system field have been very much concerned about different sensing devices that reliably fetch required signals to analyze in a better way using different computational and analysing tools. Different intelligent algorithms have been proposed in the past with the aim of controlling the whole system smoothly. Researchers are changing and revising these existing algorithms as a result of the increased complexity of the system due to the inclusion of various entities. Better controlling, monitoring, and protection of the system require a clear understanding of all feasible power system abnormalities. The deviation of any quantity, such as current, voltage, power, etc., from its normal operating condition is termed a power system disturbance. The immediate effect due to these disturbances is faced by all electrical equipment and appliances connected to the system. Anything from maloperation to permanent damage may happen. Consequently, voltage and current quantities get distorted. These abnormalities may persist for a few microseconds to a few cycles and even for hours. In this work, voltage and current during

all possible disturbances have been investigated. The causes of disturbance creation, termed as events, have also been studied. Even these disturbances may be of a cumulative type due to the occurrences of two or more events. Two or more events may occur simultaneously or one after another. These probabilities have also been considered. Finally, the identification of events has been studied. Fast and accurate identification is essential for adopting suitable measures to restore the system quickly.

An experimental setup with all feasible disturbance-creating event arrangements and sensing devices has been fabricated for producing power system events. Instrument transformers have been used to sense line currents and node voltages, and a data acquisition system has been arranged to record those sensed signals. These acquired signals have been filtered to eliminate noise using mathematical tools and unsupervised machine learning techniques before the data have been normalized. These normalized filtered data have been processed using different signal-processing techniques to extract their particular features. Processed data have been represented in different formats to make them compatible with the various machine learning techniques. At different stages of this work, various advanced machine-learning techniques were used to classify the events.

Throughout the work, the number of events and their types were revised and modified by including new investigated events, and subsequently, different classifiers were modelled. These models have been equipped with a laboratory-based system to observe their working in case of any real-time event.

Chapter 1 of this thesis provides an overall concept of system disturbances and the origin of the disturbance. Some adverse situations arising due to these disturbances have also been illustrated to realize their effects. A few research works in this area have also been highlighted.

Chapter 2 has been organized to illustrate the laboratory-based experimental arrangements for conducting some tests on power system

events. Their original photographs have shown each part of this experimental setup.

Chapter 3 deals with a few very commonly occurring single event-based disturbances and a few classifiers for their classification.

In Chapter 4, a few multi-event-based disturbances were considered along with the single-event disturbances. Finally, a few deep learning-based classifiers have been proposed depending on the number and type of cases considered. In addition to these, a special type of classifier has been proposed to visually classify all disturbance categories using 2D plotting of data.

In Chapter 5, an overall conclusion has been drawn, and a few future scopes in accordance with the power system advancement in the field of system monitoring and protection have been proposed.

Contents

List of Figures

List of Tables

List of Abbreviations

A	
ANN	Artificial Neural Network
B	
BD	Big Data
C	
CB	Circuit Breaker
CCF	Common Cause Failure
CF	Cascading Failure
CMF	Common Mode Failure
CNN	Convolution Neural Network
CP	Classification Process
CS	Child Signals
CVT	Constant Voltage Transformer
CWT	Continuous Wavelet Transform
D	
DAA	Data Acquisition Arrangement

DAE	Deep Auto Encoder
DAS	Data Acquisition System
DFA	Detrended Fluctuation Analysis
DG	Distributed Generators
DL	Deep Learning
DSO	Digital Storage Oscilloscope
DT	Decision Tree
DVR	Dynamic Voltage Restore
DWT	Discrete Wavelet Transform
E	
ED	Euclidean Distances
EMD	Empirical Mode Decomposition
EPEEMD	Energy-Preserving Ensemble Empirical Mode Decomposition
F	
FEP	Feature Extraction Process
FFT	Fast Fourier Transform
FPGA	Field Programmable Gate Array
H	
HHT	Hilbert Huang Transform
HIF	High Impedance Faul
I	
IGWO	Improved Grey Wolf Optimization

IRT	Infrared Thermal
ISO	Independent System Operators
K	
KELM	Kernel Extreme Learning Machine
KNN	K-Nearest Neighbors
L	
LLG	Line-Line To The Ground
LLL	Three Phase Fault
LSSVM	Least Square Support Vector Machine
M	
MC	Mystery Curve
ML	Machine Learning
MM	Mathematical Morphology
MPC	Main Power Circuit
MS	Mother Signal
MST	Multi-Resolution S-Transform
N	
ND	Negative Dependence
NLDC	National Load Dispatch Center
P	
PC	Principal Components
PCA	Principal Component Analysis

PCC	Point Of Common Coupling
PGCIL	Power Grid Corporation Of India Ltd
PMU	Phasor Measurement Units
PQD	Power Quality Disturbances
PSD	Power System Disturbances
R	
RCT	Relative Computational Time
RF	Random Forest
RLDC	Regional Load Despatch Centre
S	
SF	Shape Factor
SFS	Sequence Forward Search
SLG	Single Line To Ground
SNR	Signal-To-Noise Ratio
SSR	Solid-State Relay
ST	Stockwell Transform
SVM	Support Vector Machine
T	
TF	Transfer Learning
U	
UI	Unscheduled Interchage
UMAP	Uniform Manifold Approximation and Projection

V

VFD	Variable Frequency Drive
VMD	Variational Mode Decomposition

W

WT	Wavelet Transform

List of Symbols

A list of all the symbols, their representative quantities and units have been provided below to familiarize the readers with the frequently used symbols within this thesis.

Symbols

E_n	Power system n^{th} event
$f_n(t)$	Response at n^{th} node at time t
α	Coefficient of reflection
β	Coefficient of transmission
$\bullet$	Closing operation
$\circ$	Opening operation
λ	Eigen value
$\mathcal{F}$	Fourier operator
$\mathcal{F}^{-1}$	Inverse Fourier
$\mathcal{L}$	*Lagrange function*
$\ominus$	Erosion
$\oplus$	Dilation
$\psi[n]$	Mother wavelet

$\mathbf{B}$	Structural element
$\mathbf{b}$	Bias vector
$\mathbf{W}$	Weight vector
$\mathbf{X}^T$	Transpose of matrix $\mathbf{X}$
cov or Σ	Covariance
W_ϕ	Approximate coefficien
W_ψ	Detail coefficients
$*$	Convolusion operation
CB	Circuit breaker
j	$\sqrt{-1}$
SW	Switch
W(t)	Window function

Symbols and units

δ	Phase of voltage with respect to reference phasor	degree
ϕ	Phase of current with respect to reference phasor	degree
$\mathbf{I}_{ij}$	RMS current flowing fromi^{th} node to j^{th} node	amps
$\mathbf{V}_i$	RMS voltage at ith*node*	*volts*
$\mathbf{Z}_{ij}$	Line impedance of the line between i^{th} and j^{th} node	ohms
C_{gen}	Generator stray capacitor	μF
C_{trans}	Transformer stray capacitor	μF
f	Frequency	Hz
i_{ij}	Instanteneous current flowing from i^{th} node to j^{tj} node	amps
p_{ij}	Instanteneous power flow from i^{th} node to j^{tj} node	watts

v_i	Instanteneous voltage at i^{th} node	volts
ω	Angular frequency of oscillation	rad/sec
ϕ	Flux	wb
V_{peak}	Peak voltage	volts
Z_{ph}	Per phase impedance	ohms
B	Flux density	wb/m^2
H	Magnetic field intensity	AT/m
L	Inductance	henry

CHAPTER 1

Introduction

1.1 Power System Disturbances

For any well-designed and planned power system, the power flow, voltages at different nodes and line currents are obtained by using load flow analysis. If the harmonics are ignored, the power flow at any point in the power system is sinusoidal in nature. This power flow is steady, and for a healthy system at any instant of time, the total generation will be exactly equal to the sum of the total load demand and network loss, maintaining the voltage and frequency within their tolerable limits. However, any change in the system condition will cause the power flow at all the locations to deviate from its previous steady value [1]. Power system disturbances, defined as the waveform distortion of a power system under normal or abnormal conditions, contain considerable system and equipment state information. Obtaining equipment and system state information from a power disturbance is very important to ensure the safety of power grids. A power disturbance generally refers to the phenomenon or event of three-phase voltage/current waveform distortion and deviation from an expected value, which includes steady-state voltage/current deviations, such as voltage/current imbalance and harmon-

ics, and transient waveform abnormalities, such as load switching and fault disturbance.

Power system disturbance is a major concern among utility engineers. Consumers and utilities both suffer due to PSD. Nowadays, power semiconductor-based devices are being used by power industries and consumers. For their proper functioning, quality power has to be assured. Even this is the cause for relaying system to be malfunctioned. The immediate effects of these disturbances are voltage sag, voltage swell, frequency change, voltage fluctuations etc. These disturbances are caused by different power system phenomenon viz. switching, sudden load change, line fault, generator fault etc.

Early detection of these disturbances are highly recommended for the relaying system to take correct decision within a couple of cycles. This helps system to act correctly and protect all connected equipment from being damaged.

The progress in adaptive protection systems heavily relies on signal processing, where the key measurable parameters include the magnitude and phase angle of voltage and current signals, as well as the system frequency during disturbances, etc. Accurate extraction of these attributes is crucial for identifying PSDs correctly.

Before the in-depth study, the causes of PSD, their effects, and types were dealt with at the initial stage, as given in the following section.

1.2 Causes of Power System Disturbances

Switching on or off is very common phenomenon in power systems. The switching operations are conducted when loads, generators, lines, transformers, capacitor banks, reactors, etc. are required to be energized or de-energized. Other than switching operations, a lightning stroke on the line or adjacent object also induces a unipolar transient wave known

as the impulse, which propagates along the line in both directions from the point of strike .

Typically, transients are generated when there is a rapid change in circuit conditions. These are summarized below.

☐ Closing of a switch (electromechanical or solid-state)

☐ Opening of a switch

☐ Associated with Connection/Disconnection of an energy source, transformer, overhead line, cable or load to the circuit

☐ Occurrence/Clearing of a circuit fault

☐ Occurrence of lightning strike

Here, all the transients are electromagnetic in nature. Other than these, any mechanical energy deviation occurring in rotating machines integrated with the system also causes **electromechanical transients** in the system.

1.3 Effects of Power System Disturbances

Initially, all feasible distorted signals were investigated, and their natures were studied thoroughly. Around 90% disturbances are of short duration, less than 1 second. One complete cycle or a more distorted wave is specified by the rms value, and a wave less than one cycle is expressed by its fundamental sinusoidal peak. power quality issues depending on the duration and depth of disturbance, as stated in the IEEE Standard 1159-2009 [2], are summarized in Table 1.1. In general, these are classified into the following broad categories.

1.3.1 Sag

Voltage sags are a major source of power quality problems for the electric power sector. It has been observed that voltage sag happens due to the following reasons:

Table 1.1: Category-wise probability of the major power quality disturbances

Power Quality Variations	Duration and disturbance depth wise categories	Events	Abnormal Events: Short circuit Faults	Open Circuit Fault	Improper Ground	Lightning	Resonance	Power Unbalance	Power Mismatch	Line Tripping	Shaft power Interruption	Generator Outage	Nornal Events: Non-linear Load	Battery Charging	Transformer Energizing	Islanding	Grid Synchronization	Inductive Load Switching	Capacitor Switching	Motor Inrush	Line Energizing	Auto reclosing
	Transient /Instanteneous Disturbance depth : 0.1-0.9 pu (5 ms to 600 ms)	Oscillatory	√				√				√						√		√		√	√
		Impulsive				√	√															
		Sag	√												√				√	√		
		Swell								√								√				
	Short Duration Variation / Momentary Depth : 0.1-0.9 pu (600 ms to 3 sec)	Interruption																				√
		Sag	√												√					√		
		Swell		√						√								√				
	Frequency Variation							√	√		√	√				√	√					√
	Long Duration Variation / Temporary Depth : 0.1-0.9 pu (3 sec to 1 min)	Over Voltage		√	√				√										√			
		Under Voltage							√													
	Steady State Variation Depth : 0.1 to 0.2 pu (> 1 min)	Harmonics											√	√								
		Notch											√	√								
		Flicker																		√		√
		Unbalance			√			√								√						

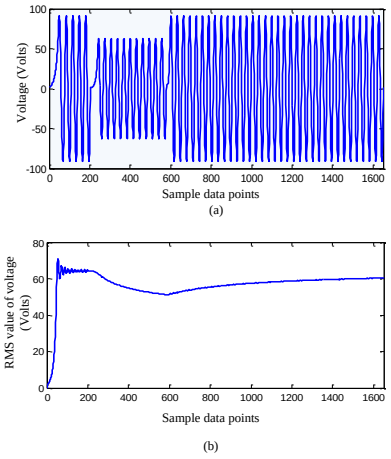

Figure 1.1: (a) Voltage sag due to sudden starting of large load (b) Variation of RMS value of voltage at residential consumer node

- During fault
- When a large load or an induction motor is switched on and
- During energising of a transformer.

This observation has been made through MATLAB simulation, where a single phase supply powers a 70.7 V, 200 W single-phase load. A large load of 2500 W has been suddenly switched on and the RMS value has been measured. The voltage sag and corresponding RMS value have been shown in Figure 1.1. The sag voltage is numerically defined as

$$v(t) = \begin{cases} V_m \sin \omega t & \text{for } \; t \leq t_1 \text{ and } t \geq t_2 \\ \alpha V_m \sin \omega t & \text{for } \; t_1 < t < t_2 \end{cases} \tag{1.1}$$

where, V_m is the maximum value of the voltage signal, α lies between 0.9 to 1.0, and the sag duration may be up to nine cycles. The numerically generated waveform with the sag is shown in Figure 1.2(a).

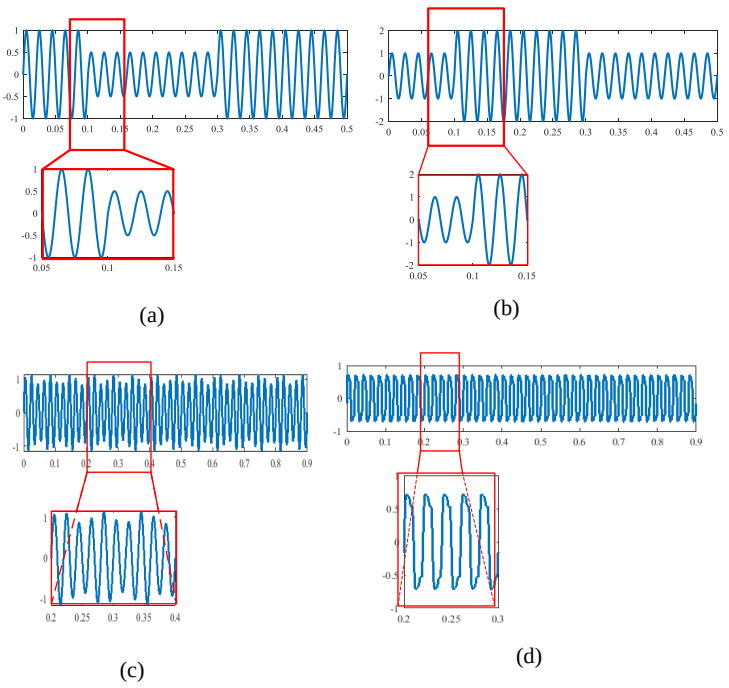

Figure 1.2: Waveforms during (a) sag (b) swell (c) voltage fluctuation (d) harmonics

Table 1.2: Categories and characteristics of sag and swell

Categories	Types	Duration	Magnitude
Instantaneous	Sag Swell	Half cycle to 30 cycles	0.1 to 0.9 pu 1.1 to 1.8 pu
Momentary	Sag Swell	Up to 3 seconds	0.2 to 0.9 pu 1.1 to 1.8 pu
Temporary	Sag Swell	3 seconds to 1 minute	0.3 to 0.9 pu 1.1 to 1.8 pu

1.3.2 Swell

When a large load or power line is suddenly switched off, the node voltage near this load gets increased for a short duration of time as shown in Figure 1.2(b). This is termed as swell. When this increased voltage lasts for a longer period, over voltage occurs. This overvoltage is dangerous for system and equipment insulation. This swell is more pronounced in the ungrounded or delta system. When a phase conductor gets connected with the ground, the sudden voltage rise occurs in unfaulted phases. In case of current interruption, a high voltage is generated due to the inductive effect of the power circuit. To mitigate such voltage swell dynamic voltage restorer (DVR) or constant voltage transformer (CVT) are used. Depending on the duration, voltage sags and swells are of three different types—instantaneous, momentary and temporary—as summarized in Table 1.2.

1.3.3 Voltage fluctuation

Sometimes, the voltage at the load terminal systematically changes for a certain duration. This is termed as voltage fluctuation. Its immediate effect is the flickering of the light loads. It happens due to frequent

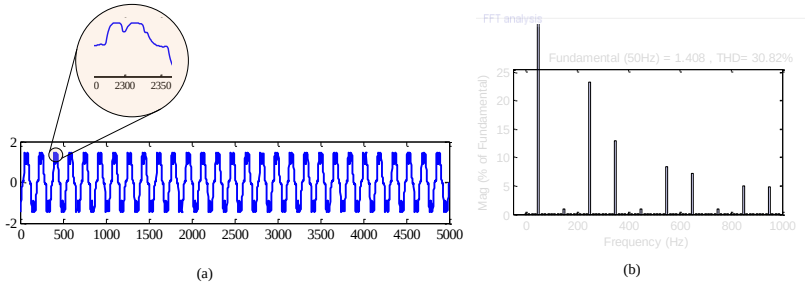

Figure 1.3: (a) Distorted TRIAC current (b) Frequency contents

changes in active and reactive power consumed by large loads in the system. A few sources responsible for voltage fluctuation are:

- arc furnace
- electric welding
- starting of large dynamic load

The voltage typically fluctuates from 0.1% to 7% of the nominal value as given in Figure 1.2(c).

1.3.4 Harmonics

Harmonics is the major cause of power loss in power systems. The presence of some non-linear loads like variable frequency drives (VFD), UPS, battery chargers, etc harmonics current flows in the lines as shown in Figure 1.2(d). The currents containing multiple frequencies or harmonics lead to power losses in transmission lines and electrical equipment. It also produces overheating of transformers. The TRIAC current for a three-phase circuit is shown in Figure 1.3 (a) and its frequency contents along with the fundamental component is shown in Figure 1.3 (b).

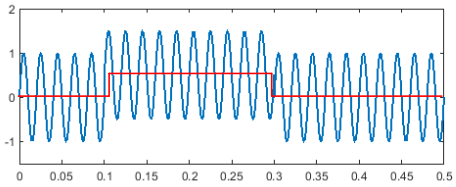

Figure 1.4: DC offset voltage

1.3.5 DC offset

The inductances are being possessed by most of the power system components. As a result, during any increase in current, whatever the cause is, an opposing current is produced as per Faraday's law of electromagnetic induction given by $v_i = L\frac{di}{dt}$. this sudden increment of the opposite current makes the sinusoidal current shift up or down depending on the inception angle when the fault occurs. One numerically generated such DC offset waveform has been shown in Figure 1.4.

1.3.6 Impulsive voltage

The switching operation is a very common phenomenon in power systems. During the making or breaking of a circuit breaker (CB) a short-duration transient voltage arises in the system due to the capacitive effect of the different electrical equipment. This switching surge may last for 1 to several milliseconds. The enlarged view of this surge voltage is shown in Figure 1.5. This voltage is characterized by the rise time and fall time.

1.3.7 Oscillation

When a circuit contains inductance and capacitance, for any switching operation, high transient surge voltage creates an oscillation of energy

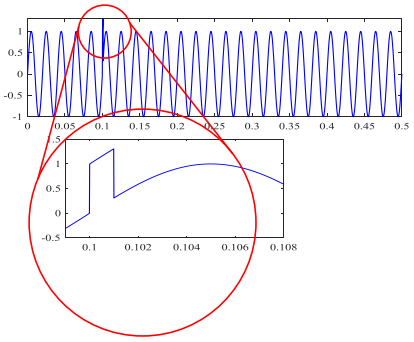

Figure 1.5: Impulsive voltage

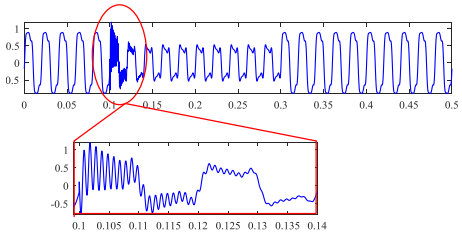

Figure 1.6: Oscillation due to switching of nonlinear load

between these two elements. Here, in Figure 1.6, the non-linear load is varied with the help of a switch. It is seen that the oscillation decays in two cycles.

1.3.8 Notch

When current switches from one phase to another during regular power electronic device operation in a power electronics-based circuit, a short circuit occurs for a few microseconds, which results in a voltage notch. This notching is periodic. Figure 1.7 shows the enlarged view of the notch.

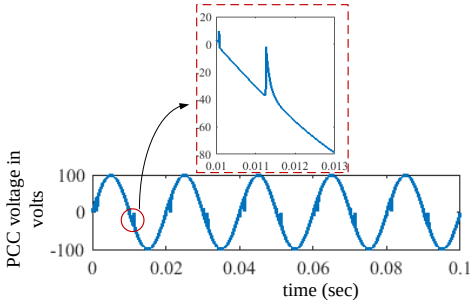

Figure 1.7: Notches during power electronic device switching

1.3.9 Frequency variation

During a fault in a large transmission line, a sudden bulk load change, or a power interruption due to unit outage, the frequency varies as shown in Figure 1.8 (a).

1.3.10 Noise

During the measurement of any signal, an unwanted high-frequency random signal gets superimposed on the actual measurement. The sources that originate this noise, are power electronic devices, control circuits, arcing equipment, loads with solid-state rectifiers, etc. Such noise is shown in Figure 1.8 (b). This problem is mitigated using filters and isolation transformers.

1.4 Types of Power System Disturbances

Here, some single power system events and some dual events that cause PSD, have been investigated, along with their definitions.

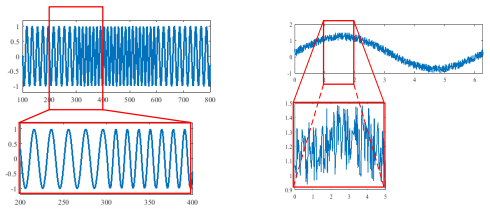

(a) (b)

Figure 1.8: (a) Frequency variation (b) Noise

1.4.1 Single Type Power System Disturbances

Any phenomenon in a power system causes voltage and/or current distortion. For instance, for a power system as shown in Figure 1.9(a), the voltage, current and power at location A change from one steady state condition to another steady state condition for the line tripping at location B. In this power system, the power flow through point A is given by Equation (1.2).

$$p_{ij} = v_i i_{ij} \tag{1.2}$$

The voltage waveforms at i^{th} and j^{th} nodes are $v_i = \sqrt{2}|\mathbf{V}_i| \sin 2\pi ft$ and $v_j = \sqrt{2}|\mathbf{V}_j| \sin(2\pi ft - \delta)$ respectively. The current flowing through point A is $i_{ij} = \sqrt{2}|\mathbf{I}_{ij}| \sin(2\pi ft - \phi)$ which can be obtained using $\mathbf{I}_{ij} = \frac{\mathbf{V}_i - \mathbf{V}_j}{\mathbf{Z}_{ij}}$. The phasor diagrams of all quantities at i^{th} node before and after the trip operation have been shown in Figure 1.9(b) and (c). Figure 1.9 (d) illustrates two sets of the voltage, current and power flow waveforms– $(v_{i1}, i_{i1}, p_{ij1})$ and $(v_{i2}, i_{i2}, p_{ij2})$ for both the circuit conditions, i.e. the conditions before and after the line trip at location B. The time taken by the system to attain a steady state after the line trip is known as the disturbance period. This disturbance time and the nature depend on the type of the event. In Figure 1.9 (d), the irregular transient voltage

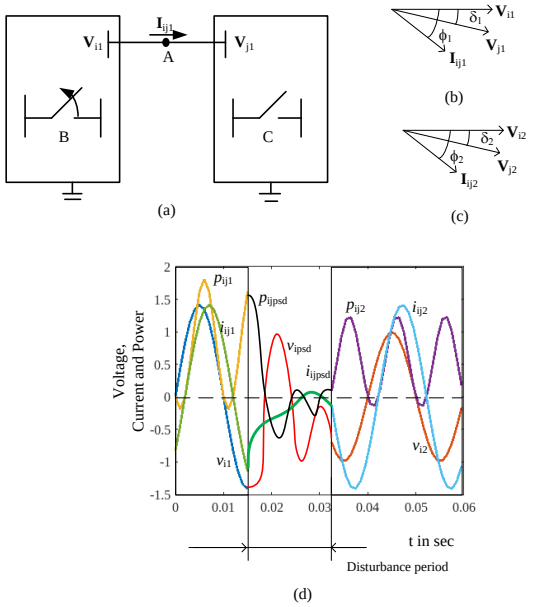

Figure 1.9: Illustration of power system disturbance: (a) complete power system with disturbance (b) Steady-state phasor at the location A before the line tripping at B (c) Steady-state phasor at the same location after the line tripping (d) Voltage, current and power transition from one state to another state

(v_{ipsd}), current (i_{ipsd}) and power flow (p_{ipsd}) have been shown in the disturbance time zone.

1.4.1.1 Timeframe of different phenomena

The techniques for analysing different phenomena depend on the duration for which the event persists, as given below.
□ Steady-State Phasor Analysis
1. Load Flow: more than 1 second
2. Fault: 0.02 second (1 cycle) to 10s of seconds
□ Transient Analysis
1. Lightning: 0.1 microsecond to 1 millisecond
2. Switching: 10 microseconds to 1 second
3. Power Electronics: microseconds to milliseconds
4. Transient Stability: 1 millisecond to 10 seconds

Though power system operations are stable, they are not static. The operating condition continuously changes as loads, lines, transformers, and capacitor banks are switched on or off. This change of state occurs through transients known as switching transients. During this transient, energy changes between capacitors and inductors and dissipates through circuit resistances. These capacitances may comprise a capacitor bank or stray capacitances formed in different power system components as listed below. Three primary components in a power system—alternator, transformer, and transmission line—exhibit stray capacitances, which, along with the inductances, cause energy to oscillate between them during any transient. Switching transients results in large variations of current, voltage, and frequency. These are short-duration events with frequencies between a few hundred Hz and kHz and damped in less than half to one cycle [3]. Transient disturbances were recorded as waveform data. Moreover, with widespread access to distributed generation and

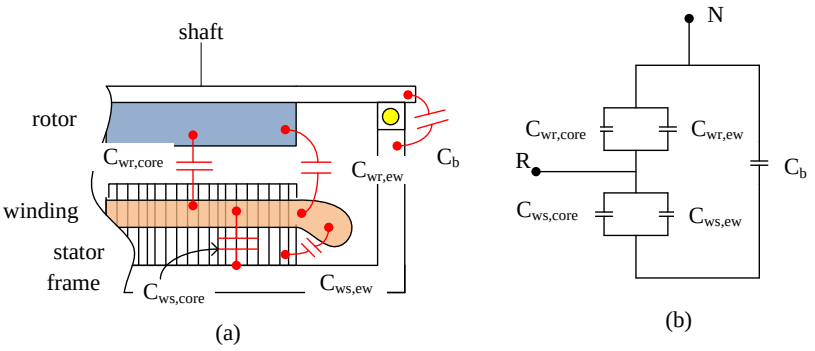

Figure 1.10: Stray capacitance of an alternator (a) all possible stray capacitances formed (b) equivalent circuit connecting all stray capacitances

the application of power electronic devices, disturbances are becoming more complex. Therefore, waveform data are necessary for many power system applications.

1.4.1.2 Stray capacitances

1.4.1.2.1 Generator stray capacitance: From the basic knowledge of capacitance formation, the armature winding of any phase forms an equivalent capacitance with neutral, and this is also a series-parallel combination of five significant capacitances formed between different conducting parts of the generator as shown in Figure 1.10 (a). Here, the inner part and overhang parts of phase winding form capacitances with the rotor and stator separately with different values $C_{wr,core}, C_{wr,ew}$, $C_{ws,core}$ and $C_{ws.ew}$. The stator frame also makes a capacitance with the shaft across the bearing,C_b. The equivalent capacitive circuit has been given in Figure 1.10 (b). The stray capacitance of the generator C_{gen} is obtained using Equations (1.3) and (1.4).

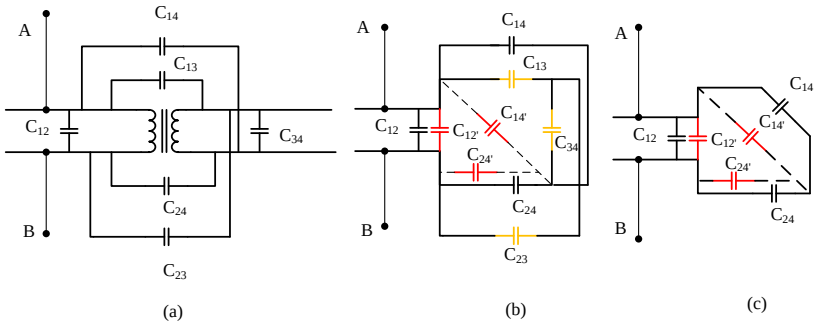

Figure 1.11: Stray capacitance for transformer. (a) all feasible stray capacitances between HV and LV windings (b) star to delta conversion for simplification; (c) simplified circuit to obtain equivalent stray capacitance.

$$C_{Gen} = (C_{wr,core} + C_{wr,ew}) || \{(C_{ws,core} + C_{ws.ew}) \; in \; series \; with \; C_b\} \tag{1.3}$$

$$C_{Gen} = C_{wr,core} + C_{wr,ew} + \frac{(C_{ws,core} + C_{ws.ew})C_b}{C_{ws,core} + C_{ws.ew} + C_b} \tag{1.4}$$

1.4.1.2.2 Transformer stray capacitance: Four conducting terminals of two windings of each phase form six capacitances [4], as shown in Figure 1.11 (a). Here, four terminals are $1, 2, 3$ and 4. capacitance between 1 and 2 is C_{12} and likewise, others have been symbolised. Figure 1.11 (b) and (c) shows the equivalent capacitive circuit. A star delta conversion procedure has been applied to simplify the circuit. The capacitance between 1 and 4 terminals of the converted delta, $C_{14'}$ is obtained using Equation (1.5) and has been simplified using Equation (1.6).

$$\frac{1}{C_{14'}} = \frac{1}{C_{13}} + \frac{1}{C_{34}} + \frac{\frac{1}{C_{13}}\frac{1}{C_{34}}}{\frac{1}{C_{23}}} \tag{1.5}$$

$C_{14'}$ is simplified as

$$C_{14'} = \frac{C_{13}C_{34}}{C_{34} + C_{13} + C_{23}} \tag{1.6}$$

Thus, the other delta-converted capacitances can be derived in the similar manner. The equivalent stray capacitance is obtained using a series-parallel combination as given in Equations (1.7) and (1.8).

$$C_{trans} = (C_{12} + C_{12'})||\{(C_{14} + C_{14'})\ series\ with\ (C_{24} + C_{24'})\} \tag{1.7}$$

$$C_{trans} = (C_{12} + C_{12'}) + \frac{(C_{14} + C_{14'})(C_{24} + C_{24'})}{(C_{14} + C_{14'}) + (C_{24} + C_{24'})} \tag{1.8}$$

1.4.1.2.3 Line stray capacitance: Power lines are usually exposed outside. Therefore, stray capacitance, commonly known as shunt capacitance, plays a major role during any transient and these stray capacitances are distributed along the line.

For any switching ON/OFF or any line tripping, stray capacitance (C), inductance (L) and line resistance (R) will form an oscillatory circuit as shown in Figure 1.12 (a) where V_0 and I_0 are the initial conditions of C and L, respectively. The total energy stored in the C and L (i.e. $0.5CV_0^2 + 0.5LI_0^2$) is being dissipated through the resistance in the form of heat. As shown in Figure 1.12(b), the resulting oscillatory current and power dissipation continue until the circuit energy becomes zero. The frequency of oscillation is determined by $\frac{1}{2\pi\sqrt{LC}}$. Figure 1.12 (c) shows the corresponding energy states of C and L. If t_s be the time when oscillation vanishes, it is determined using Equation (1.10).

$$\int_0^{t_s} p(t)dt = [E_C(t)]_{t=0} + [E_L(t)]_{t=0} \tag{1.9}$$

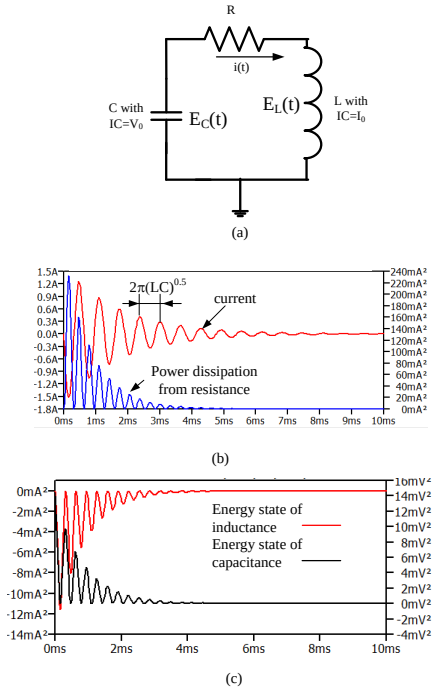

Figure 1.12: (a) Basic RLC oscillatory circuit (b) Circuit current and power dissipation (c) energy state of the components

$$\int_0^{t_s} [i(t)]^2 R dt = [E_C(t)]_{t=0} + [E_L(t)]_{t=0} \tag{1.10}$$

1.4.1.3 Lightning Transient

During lightning, the emf induced in the line travels in both directions from the point of strike. The frequency of occurrence of lightning has been given in Figure 1.13 (a) as mentioned in [5]. It has also been recorded that in 50% cases of lightning, peak current becomes more than 45 kA. The maximum peak may reach up to 200 kA. The typical

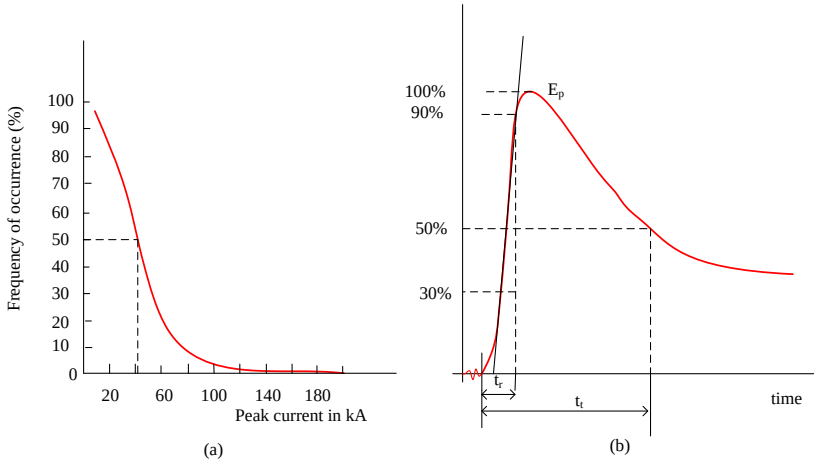

Figure 1.13: (a) Frequency of occurrence of lightning as per [5] (b) Standard characteristics of lightning impulse)

lightning strike rises to peak within 1-10μsec and decays to 50% of peak within 20-100μsec as shown in Figure 1.13 (b).

1.4.1.4 Switching operations

1.4.1.4.1 Single capacitance switching: One of the most common switching events is capacitor switching [6]. Figure 1.14 (a) shows a simplified capacitor switching circuit. The switching instant is a very important factor. The magnitude of the oscillations depends upon the difference between the source voltage and the initial capacitor voltage at the instant of switching. This difference may vary from 0 to double of the peak. At the time of switching, if the capacitor voltage is different from the system voltage, the PCC voltage is pulled to the capacitor voltage, and an oscillation occurs until the capacitor charges to the system voltage. The voltage across the capacitor after the switching is shown in

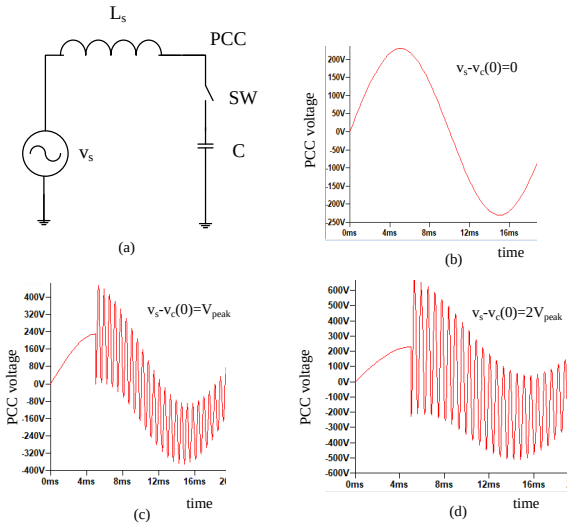

Figure 1.14: Single capacitor switching event (a) switching circuit (b) PCC voltage waveform for the initial capacitor voltage exactly equal to source voltage (c) for the voltage difference of V_{peak} (d) for the voltage difference of $2V_{peak}$ [6]

Equation (1.11).

$$v_c(t) = v_s - (v_s - v_c(0)) \cos \omega_0 t \tag{1.11}$$

where, $\omega_0 = \frac{1}{\sqrt{L_s C}}$

Here, three such instances have been studied. The nature of the waveforms for three different initial values of the capacitor bank has been studied. The waveforms are shown in Figure 1.14 (b), (c), and (d), respectively.

1.4.1.4.2 Capacitor switching off: During switching off the capacitor, the sudden overvoltage in the system depends on the energy stored at that instant. A significant voltage may appear at the PCC as

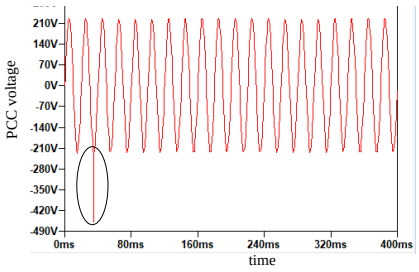

Figure 1.15: PCC voltage during capacitor switching off

shown in Figure 1.15. If the capacitor is not fully discharged after the switching off, it may produce high inrush current when the capacitor is again brought back into service.

1.4.1.4.3 Circuit Breaker (CB) restriking during the switching off capacitor bank or no load line: Restriking in the circuit breaker may take place following the peak of the supply voltage. There will be a sudden arc current causing voltage stress on the capacitor bank or the line. The repetition of such restriking causes this voltage to grow three, five, seven times, and so on, the supply voltage, which is dangerous for insulation. In the Figure 1.16 (a), the capacitor voltage $v_c(t)$ grows up to five times the supply voltage, and the arc current continues to flow with high-frequency oscillations in the first couple of cycles. The corresponding arc current $i_{CB}(t)$ is shown in Figure 1.16 (b).

1.4.1.4.4 Back-to-back capacitor switching: In back-to-back capacitor switching, a fast transient (in the range of kHz) is followed by a slow transient (in the range of several hundreds of Hz) as shown in Figure 1.17.

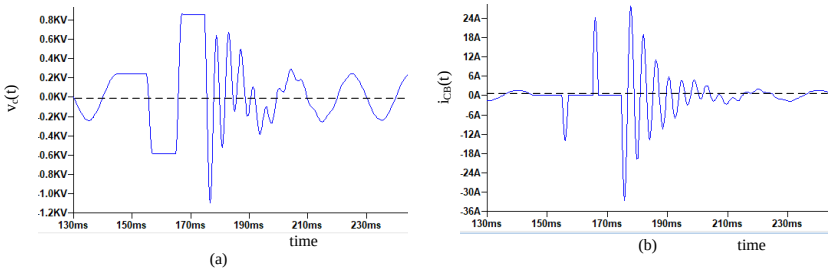

Figure 1.16: (a) Voltage rise across the capacitor bank or line during CB interruption (b) capacitor current interruption and restriking.

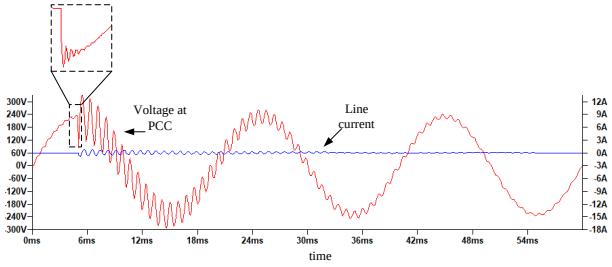

Figure 1.17: PCC voltage and line current waveforms for back-to-back capacitor switching

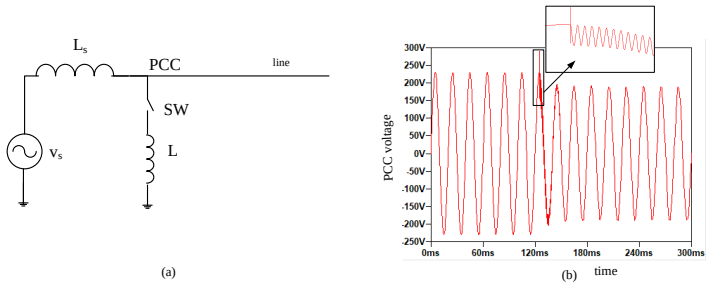

Figure 1.18: Transient due to reactor switching

1.4.1.4.5 Reactor switching: The reactors are brought into circuits to protect the insulation from damage due to overvoltage during lightly loaded or no-loaded conditions. When a shunt reactor is switched on as shown in Figure 1.18(a), a high-frequency oscillation is superimposed with the power-frequency voltage as shown in Figure 1.18(b). The frequency of oscillation is determined by the reactor and the line capacitance.

1.4.1.4.6 No load transformer de-energization: During deenergization of a transformer, if the magnetizing current suddenly falls to zero, as shown in Figure 1.19(a), the energy stored in the winding oscillates between the transformer-stray capacitance and inductance. This may cause the winding current to oscillate and the initial voltage across the primary winding to rise to four to seven times the supply voltage, as shown in Figure 1.19(b). This may initiate CB-current to restrike a couple of times.

1.4.1.4.7 Inrush current in transformer: At a steady-state on-load condition, current through a transformer becomes 'non-sinusoidal' due to the non-linear nature of the magnetic property of the core in the saturation zone Figure 1.20 (a). Also the transformer core is magnetized

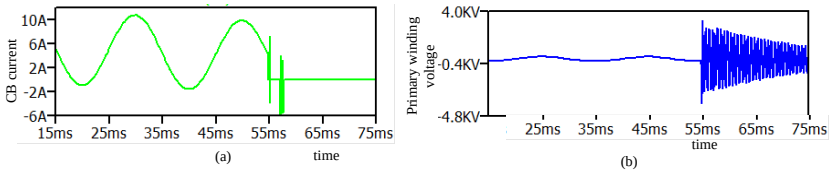

Figure 1.19: (a) current through CB (b) voltage across the winding

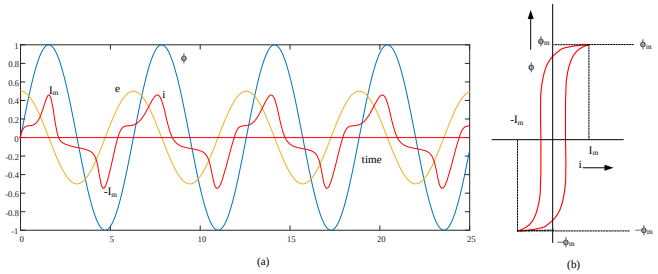

Figure 1.20: Non-linear steady-state current through transformer due to core saturation (a) applied voltage, winding current, and core flux waveforms (b) hysteresis loop.

and demagnetized in different paths due to the retentivity property of the core material. This non-sinusoidal current wave injects harmonics into the system. The B-H curve, as shown in Figure 1.20(b), depicts how flux gets saturated with current increase. During de-energization, the polarity of the remanence flux left in the core depends on the half of the current waveform in which the switch has been made off.

1.4.1.4.8 Ferro-resonance: Another non-linear phenomenon of transformer core causing series resonance involving current dependent inductance and line or cable capacitance is ferro-resonance. This effect is more prominent when a distribution transformer is energized through a distribution cable that possesses high capacitance with ground or neutral.

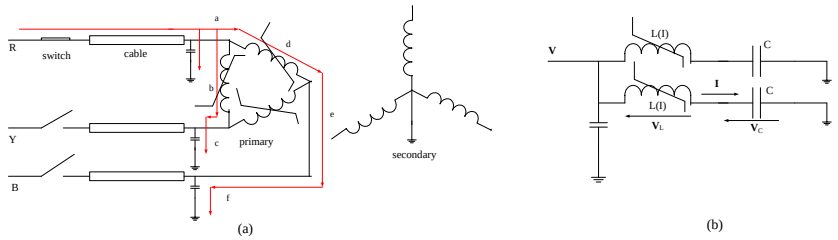

Figure 1.21: Occurrence of ferro-resonance due to maloperation of switching of the transformer (a) current paths when R phase is connected with Y and B phases opened (b) Equivalent circuit

This instant is given in Figure 1.21 (a). Inadvertently, this three-phase transformer is operated in single-phase mode. Supposing that R phase is connected and B and Y lines are open, the equivalent circuit can be represented by two single-phase parallel circuits involving transformer inductance and cable capacitances, as shown in Figure 1.21 (b).

1.4.1.5 Faults

Any component or few components in a zone may fall into a failed state (i.e. fault state) due to natural disasters like lightning, external factors like a tree branch falling, human errors or any equipment failure [7]. These faults are broadly categorized as short-circuit faults and open-circuit faults.

1.4.1.5.1 Shape of three-phase short circuit current: In a practical power system, resistance being negligible compared to the inductance of the system, the dc component during transient becomes maximum if the voltage passes through zero value. In the Figure 1.22, the fault current has been plotted for different inception angles.

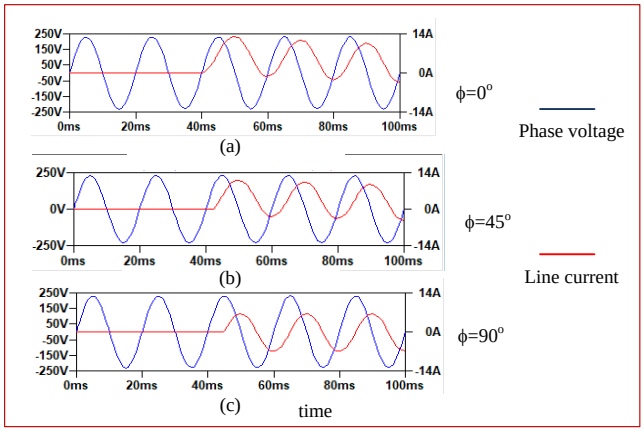

Figure 1.22: Wave shape variation of current for the variation of inception angle

1.4.1.5.2 High Impedance Fault: One of the most challenging issues faced by power engineers in power distribution systems is high impedance fault (HIF). In a few cases, the fault currents during this fault are so small that the relaying system does not operate, especially when the live conductor comes in contact with vegetation, asphalt, sand, etc. However, its consequences may be highly dangerous. The damages caused by the 2009 Victorian bushfires—a devastating one ignited by this type of fault—made it clear how important it is to fix the issue. The picture in Figure 1.23 shows its intensity.

This fault initiates when a live conductor is broken and comes in close contact with the above-mentioned materials. Initially very small fault current does not create any tripping. But, as time passes, the point of contact gets heated up and the material, i.e. insulation degradation starts. During the early stage, the current waveform takes a saw-tooth wave shape, which contains mostly third harmonics compared to second and fourth harmonics. Depending on the impurities and moisture

Figure 1.23: Devastating bushfire caused by high impedance fault at Victorian in 2009 [8]

.

content of the surface material, the conductivity and impedance vary. HIF current has a sequential time-varying wave pattern. In the *build-up* phase, the current gradually increases and reaches to a steady value in the *shoulder* region. This current is *asymmetrical*, and the degree of asymmetry depends on humidity, impurities and porosity level, and their variation in fault path for both cycles. Besides, due to resistivity variations of different layers at the contact surface, this current becomes *non-linear*. In the *intermittent* phase, the arc is extinguished and reignition takes place. This causes discontinuity of current.
In Figure 1.24(a) , a laboratory-based experimental set has been shown, where a bare conductor touches the partially wet soil. With 20 kV phase voltage, a visible arc with a hissing sound was observed (shown in enlarged view) in the same figure. The current waveform as mentioned earlier at different instances, is shown in Figure 1.24 (b). A typical circuit model has been shown in Figure 1.25 (a). The positive and negative half-current paths have two different breakdown voltages with two oppositely connected diodes. Also, two different resistances are connected in these two paths. These two unequal resistances, along with DC opposing voltage sources, produce an asymmetrical current wave and the presence of diodes in the model makes its characteristic non-linear. Figure 1.25 (b) shows asymmetrical and non-linear current waves at two different time stamps. The V-I characteristics obtained from the current waves obtained at different time stamps, as shown in Figure 1.26 show how the arc resistances, depicting the slopes of the characteristic curves in both paths, are decreased as time passes. Besides, a small hysteresis effect is observed, as shown in the inset of the same figure.

1.4.1.6 Electromechanical transients

A few mechanical issues associated with generators creating electrical disturbances have been investigated in this study as given below.

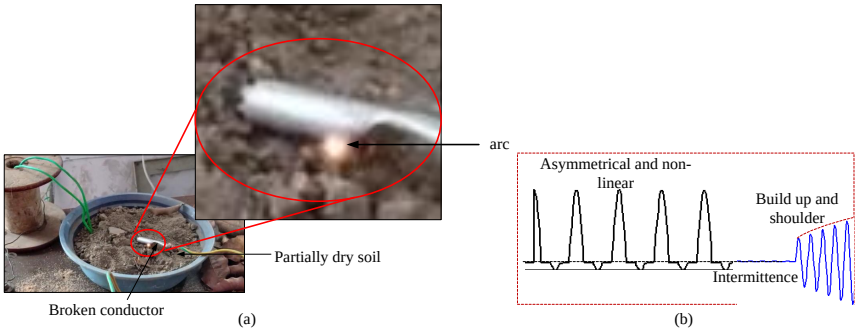

Figure 1.24: HIF test setup for partially wet soil

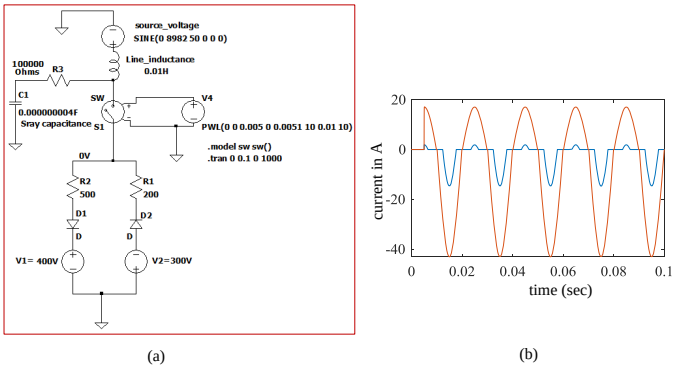

Figure 1.25: (a) Circuit model of HIF with arc (b) fault currents for two different time stamps

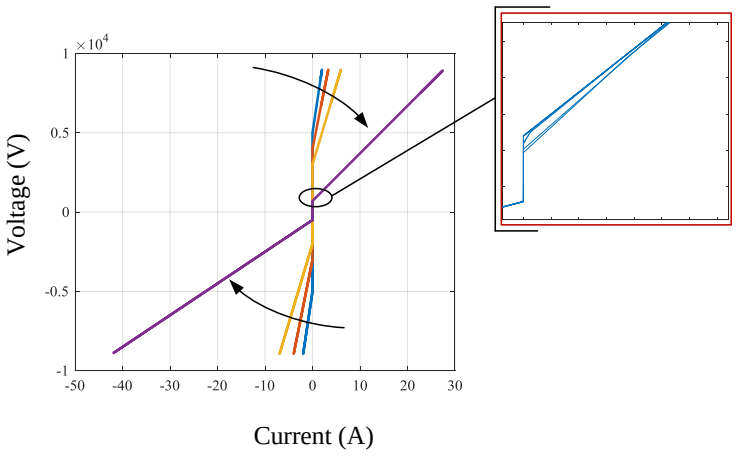

Figure 1.26: V-I characteristics of HIF.

- Turbine malfunction
- Shaft misalignment
- Bearing failure
- Rotor mass imbalance

1.4.2 Multiple Type Power System Disturbances

The possibility of two or more events cannot be ignored for the large power network though the effect or magnitude of disturbance decreases if the point of common coupling (PCC) is far from the point of occurrence. But if two or more events occur simultaneously near the PCC, then their effect has to be studied carefully.

To generalize, we may consider that a few events $E_1, E_2, E_3, ...E_n$ occur near PCC and their responses on any of PCC quantities are $f_1(t)$, $f_2(t)$, $f_3(t)$, ... $f_n(t)$. Applying the **Superposition theorem**, the resultant response can be obtained as the sum of all individual responses

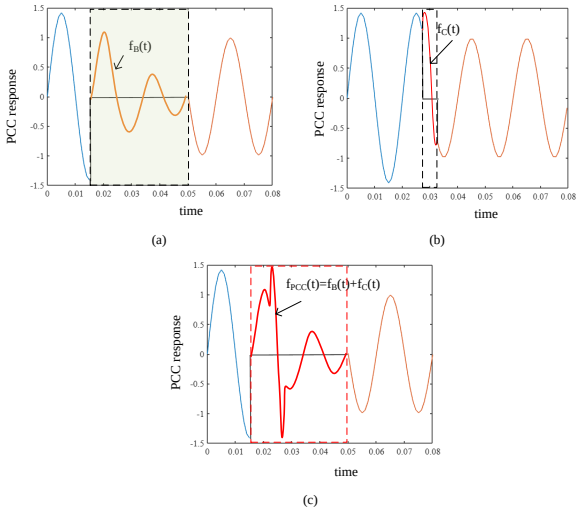

Figure 1.27: Resultant disturbance due to two simultaneous events (a) PCC response for an event at B point (b) PCC response for another event at C point (c) Resultant of both events

using Equation (1.12)

$$f_(t) = f_1(t) + f_2(t) + f_3(t) + ... + f_n(t) \tag{1.12}$$

For example, as shown in Figure 1.9 (a), if two events—E_B and E_C occur at two different locations, B and C, and at different instants of time– t_B and t_C, respectively, the resultant response at PCC, $f_{PCC}(t)$ is evaluated using Equation (1.13).

$$f_{PCC}(t) = f_B(t) + f_C(t) \tag{1.13}$$

Here, in the Figure 1.27(a) and (b), the responses at PCC due to events at B and C, respectively, are shown. The resultant PCC response has been given in Figure 1.27(c).

The wave pattern in the disturbance period (t_D) shown in Figure 1.9 (d) and Figure 1.27(c); and also the t_D are two significant parameters to be studied at the initial stage of investigation. In a classification problem, the first important task is to define the events categorically as per their severity and effects on the system. After going through all the probable causes and their effects, a correlation table showing disturbance patterns caused by any particular event has been prepared and presented in Table 1.1. The t_D may vary from a few nanoseconds to hours or more.

1.5 Importance of Identification of Power System Disturbances

In the previous section, all the power disturbances were discussed and their probable causes were investigated. As mentioned, these disturbances may arise due to the operations of the power system devices, the normal utility operation, the fault clearing process, and the different types of faults.

The detection of these disturbances and their mitigation are more concern among the researchers because of the following adverse effects.

- Metering accuracy gets affected.
- Malfunction of protective relays.
- Increased equipment downtime and decreased life expectancy resulting in loss of production.
- Production of noise.

In this work, initially, this detection process has been carried out for individual single events and then the same has been implemented after the inclusion of a few multi-events.

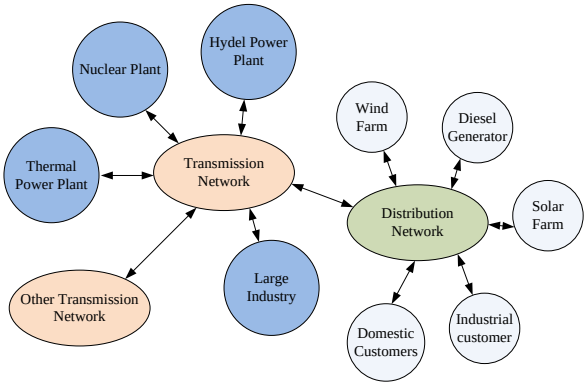

Figure 1.28: A typical modern electric power network[10]

1.6 Difficulties of Identification of Power System Disturbances

After the deregulation of the power industry in many countries, a modern power system can be said to be a network by which energy is exchanged between two customers as shown in Figure 1.28. Environmentally friendly generations are also encouraged to participate in the energy market. Here, each entity acts as a customer. The generators and consumers trade electric energy using the network. In the figure both ways arrows indicate these power exchanges. Independent System Operators (ISO) play a vital role in power and economy management in such a complex network. As per the data published in [9], it is observed that after 1995 the researchers have been working on the power quality, and between 1995 and 2004,several papers have been published.

After the reformation of the power industry over the last few decades, the relevance of distributed generator (DG) based isolated power systems has significantly expanded [11]. To ensure smooth and reliable operation and the uninterrupted provision of high-quality power, it is essential

to examine all the significant disturbances that occurred in power system network. The detection and classification of all the power system disturbances should be very fast and accurate to maintain the proper coordination and restrict the maloperation of protective devices [12]. The magnitude and phase angle of voltage and current signals, and the system frequency during disturbance are the main measuring attributes of this protection system. Therefore it is very much required to extract the accurate attributes of a specific event to identify the power system disturbances[13]. Fast detection and classification of the power system disturbances are necessary to make the relaying system more responsive and selective.

Along with the undesirable phenomena like different short circuit faults, few very obvious events like switching, load changing, starting of inductive loads and islanding have been considered in this work. For all these undesirable and obvious events, the line currents, line voltage and phase voltage get deviated from their normal wave shapes. This necessitates the use of waveform acquisition arrangement. The acquired waveforms are primarily the raw data to be used for the classification of different events. Being the problem to be multiclass type, the conventional time domain waveform analysis is not sufficient to detect the exact class, as some of the waveforms belonging to the different classes seem to be nearly identical.

Influenced by the recent research works on multi-classification problem in various fields, a few advanced classification techniques like Machine Learning (ML), Deep Learning (DL) have been introduced. In subsequent sections of this thesis, the problems, hypothesis, solution techniques, evaluation and finally conclusion have been made.

In [14], A. F. Bastos, *et al*, extracted novel information from the current waveforms acquired by a monitor at a substation. The sampled half-cycle data have been compared with the previous half-cycle data and the similarity scores were recorded. These scores for different cycles

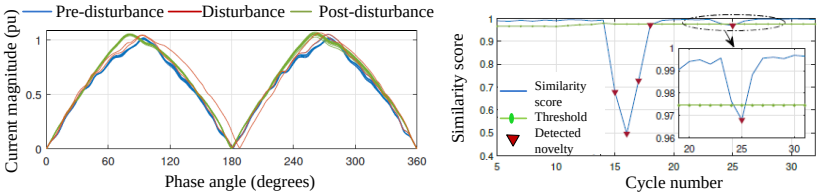

Figure 1.29: (a) Cyclic plot of current waveforms for the disturbance caused by sustained capacitor de-energisation (b) Novelty detection using current data [14]

were observed with an adaptive threshold. Novelty is observed when the similarity scores exceed the threshold value. The challenge in this technique is to be misguided by multiple zero crossings in case of harmonic distortion. This has been well avoided by considering only the fundamental component of the current waveform. When some novelties were observed, the circuit current waveforms before and after the disturbance varied as shown in Figure 1.29 (a). In this figure, the cyclic waveforms of currents before and after the de-energisation of a capacitor have been shown. Besides, in the Figure 1.29(b), a similarity score variation with respect to cycle number has been shown.

P. Khetarpal, *et al*, in [15], considered nine single and seven dual power quality disturbances (PQD) which were generated numerically. The PQD signals were converted to image before they were passed through the Gabor filter where convolution operations were carried out to extract strong features. For deep learning (DL), the *Softmax* classifier has been used. This model is also capable of identifying the initiating and terminating instants of PQD. In addition to this, the authors tested the model in a noisy environment.

In the article [16], nine single and seven dual PQDs have been generated numerically using MATLAB software. These PDQs have been

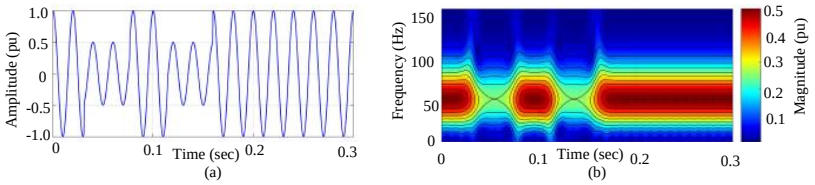

Figure 1.30: (a) Sample waveform during *sag* (b) Time-frequency scalogram for the sample disturbance using MST with optimum window size [16]

classified using the decision tree (DT) method. For feature extraction, the authors used multiresolution S-transform (MST) where the width of the window function has been modified using an adjustment factor (σ_f) given by Equation (1.14).

$$\sigma_f = \frac{1}{af^b + c} \tag{1.14}$$

The modified window function, (g_{mod}) has been given by Equation (1.15)

$$g_{mod}(t, f) = \frac{\sigma_f}{\sqrt{2\pi}} e^{\frac{t^2\sigma_f^2}{2}} \tag{1.15}$$

The Gaussian window depth, $\left(\sigma_f = \frac{1}{|f|}\right)$ is restricted by the Heisenberg uncertainty principle where it is said that time and frequency resolution cannot reach the optimum at a same time. A *sag* type disturbance and its time-frequency scalogram as shown in the article [16] are depicted in Figure 1.30(a) and (b), respectively.

In [17], the IEEE 13 bus system has been considered as a test system, and one Photovoltaic and one wind power generation are connected with PCC (i.e., node number 680). A total of nine disturbances (from C1 to C9) were created in MATLAB Simulink as given in Table 1.3. Out of these nine disturbances, C7, C8 and C9 may be assigned as dual events

Table 1.3: Events due to switch ON/OFF of DGs

Code	Event name
C1	Sudden connection of wind turbine
C2	Sudden outage of wind turbine
C3	Islanding of wind turbine
C4	Sudden PV plant connection
C5	Outage of PV plant
C6	PV plant islanding
C7	PV and wind both connected suddenly
C8	Simultaneous outage of PV and wind
C9	Islanding of both PV and wind

where two events occur simultaneously.

Classification task has been carried out using two different signal-processing techniques-Variational Mode Decomposition (VMD) and Detrended Fluctuation Analysis (DFA). The VMD followed by DFA makes the classification accuracy better with less computational time. VMD with optimal decomposition level, has been performed to filter out the noise and extract the mode function which has been fed to the DFA algorithm. This has been observed that these nine classes have been divided into three sub-sets as shown in Figure 1.31 where 2-D scatter plot between medium frequency range α_m and small frequency range α_s has been prepared.

An alternative representation of disturbance signals using a Hilbert Transform (HT)-based Mystery curve has been proposed in [18]. The signal decoupling into its time-varying amplitude and phase has been performed first as given by the flow chart in Figure 1.32. In this work, seven single and two dual disturbances have been created numerically and their Mystery curves (MC) have been shown, where each class of disturbances is clearly distinguished. For illustration, the interruption voltage signal and its respective 2D and 3D MCs are shown in Figure 1.33(a), (b) and (c), respectively.

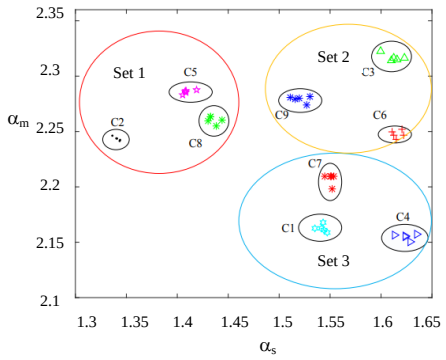

Figure 1.31: 2D scatter plot between α_m and α_s for nine disturbances

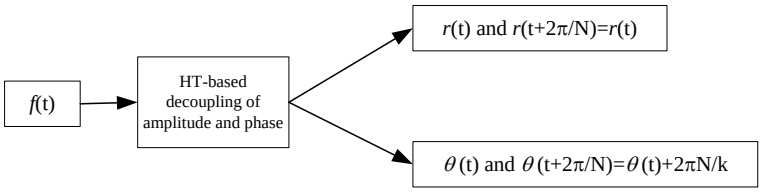

Figure 1.32: Signal decoupling into time-varying amplitude and time-varying phase

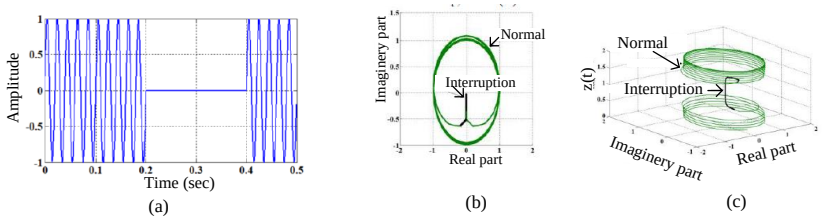

Figure 1.33: Mystery curves formation of voltage interruption signal. (a) simulated voltage signal (b) 2D MC (c) 3D MC

The authors in [19], emphasizes image processing rather than signal processing. Initially, eight common disturbance signals (i.e., sag, swell, interruption, flicker, transient, harmonics, notch and spike) were converted to the grey images followed by three image enhancement techniques-gamma correction, edge detection, and peak and valley detection. Using a Random Forest (RF) classifier the *Gini* indices have been determined and from then an optimal feature subset has been constructed using the Sequence Forward Search (SFS) algorithm. Ultimately, the RF classifier has been modelled with these feature subsets and the model was tested in a noisy environment.

In [20], authors studied the impact of five wavelet and disturbance-related factors on the disturbance detection accuracy. This study enabled the author to propose an effective model to detect the location of disturbance efficiently. Three wavelet-related factors (i.e, function, level and algorithm) and two disturbance-related factors (i.e, type and intensity, and start and end moment) were chosen as prime factors. The wavelet-based parameters were finally tuned to obtain maximum accuracy even in a noisy environment.

In the article [21], researchers have presented a different pattern of power system disturbances, where a sequence of events has been considered and a classifier has been proposed. The results were validated using real-time data obtained from a laboratory-based experimental setup. Initially, empirical mode decomposition (EMD) has been performed to obtain intrinsic mode functions (IMF) and residues. These IMFs are fed to the Gram-Schmidt orthogonal (GSO) algorithm to preserve significant energy levels and residues. After performing this process for all time series data, Hilbert transform (HT) has been applied to obtain statistical features of the resulting transform. Ultimately, least square support vector machines (LSSVM) machine learning algorithm has been applied to detect the sequence of events present in the acquired signal.

Authors in [22], addressed eight distinct disturbances and nine com-

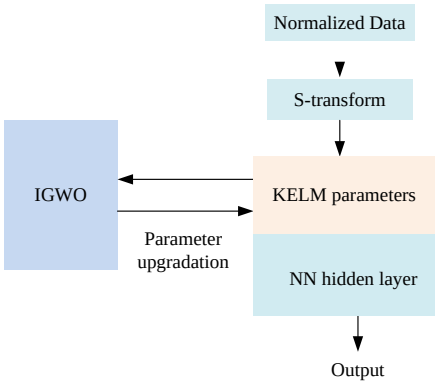

Figure 1.34: Flowchart describing the methodology

posite disturbances. A time-frequency scalogram has been created using the Stockwell transform (ST) to extract a few meaningful features. Kernel extreme learning machine (KELM) has been used to classify the disturbances. The parameters of KELM have been tuned using an improved grey wolf optimization (IGWO) technique. The flowchart of the algorithm is shown in Figure 1.34.

A total of 37 disturbances have been considered in [23]. Out of these, 8 very common single disturbances, 13 double, 12 triple and 4 quadruple type disturbances have been taken. The signals have been converted to RGB images using ST. The $227 \times 227 \times 3$input has been fed to a Deep Neural Network having five convolution layers, three pooling layers, two fully connected layers and one output layer. Besides, two activation layers have been used to filter out unwanted data mapping. These are the rectified linear unit (ReLU) and *Softmax* activation layer.

The researchers in [24], have thoroughly studied all kinds of feeder short circuit faults in the presence of high impedance. They simulated a six-feeder radial distribution system using MATLAB, and currents were collected from all three phases. The probabilistic distribution of energies

in all three phases determines the location and type of high-impedance faults. For this purpose, the wavelet transform has been carried out for all three-phase current signals, which provides approximate and detailed coefficients to construct a wavelet matrix (W) of size $(L+1) \times N$, where L and N are the levels of decomposition and data points, respectively. This W is formed by calculating the power spectral density (PSD_W), which has been obtained using Equations (1.16) and (1.17).

$$Var(\mathbf{X}_1) = \frac{1}{N}\sum_{i=1}^{N}(x_{1i} - \hat{x_1})^2 \tag{1.16}$$

$$Cov(\mathbf{X}_1, \mathbf{X}_2) = \frac{1}{N}\sum_{i=1}^{N}(x_{1i} - \hat{x_1})(x_{2i} - \hat{x_2}) \tag{1.17}$$

Here, $\mathbf{X}_1$ and $\mathbf{X}_2$ are first and second decomposed coefficient vectors and $\hat{x_1}$ and $\hat{x_2}$ are the means of the respective coefficients.

The diagonal elements of the covariance matrix (i.e, $diag(C^t = W^T W)$) gives the energy densities of all coefficients. The average energy densities and their distribution in all three phases identify the type and location of the fault.

A straightforward fuzzy-based classification of different short circuit faults was studied in [25]. A distribution system with a windfarm distributed generation has been simulated, and voltage and current signals were fed to the proposed algorithm, where each signal is decomposed using a wavelet to obtain approximate coefficients of voltage and current signals. The ratio of these two approximate coefficients provides impedance. These impedances have been fed to a fuzzy interface system (FIS) to classify the fault. In this article, all different kinds of short circuit faults for different loading conditions were extensively studied. Besides, the effect of CT saturation has also been dealt with.

Table 1.4: Camparative study of recently published articles on power system disturbance

Ref.	Number		Origin	Types	Feature extraction method	Classifier
	S	M				
[26]	10	-	PSCAD simulated	Faults	EEMD+CNN	LSTM
[15]	9	7	Nemerically simulated	Distorted waveform	Gabor filter guided	Softmax
[16]	9	7	Nemerically generated	Distorted waveform	Multi-resolution S-transform	DT
[17]	6	3	Matlab Simulink IEEE 13 bus	Event based	Variational Mode Decomposition (VMD)	DFA
[18]	7	2	Simulated Signals	Distorted waveform	Hilbert Transform (HT)	MC
[19]	8	-	Simulated Signals	Distorted waveform	Sequence Forward Search (SFS)	RF
[20]	3	-	Simulated Signals	Distorted waveform	Wavelet +disturbance impact factor	-
[21]	3	-	Simulated Signals	Sequence of events	HT	LSSVM
[22]	8	9	Nemerically simulated	Distorted waveform	ST	IGWO-KELM
[23]	8	28	Nemerically simulated	Programable ac generators	Stockwell Transform	NN
[24]	10	-	Matlab sumulated six feeder	Short circuit faults	WT	PSD
[25]	10	-	Matlab sumulated six feeder	Short circuit faults	WT	FIS
[27]	8	-	Practical	Event based	MTCDN	DNN
[28]	10	-	Practical + simulated	Event-based	MCEEMDAN +CGAN	CNN

1.7 Scopes of the Thesis

All these cited articles have been brought together as tabulated in Table 1.4 to compare one with the others and to search the scope and opportunities in this field.

N.B: S: Single event and M: Multi-events

After an extensive review, the following work opportunities have been identified.

- It has been noted that all feasible events have not been considered.

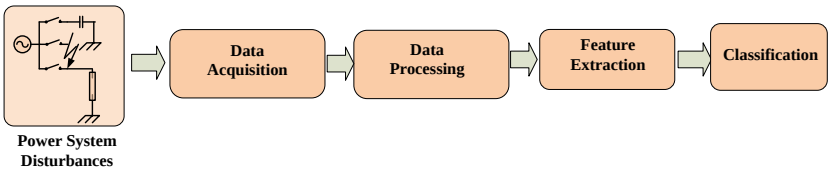

Figure 1.35: Four major sections for any disturbance classification [30]

- In most of the reviewed articles, it was observed that the authors created disturbances either numerically [14] -[16] or by introducing faults into simulated circuits [17], [19], [20], [22], [24] and [25]. Although simulation results were validated with real-time experimental results in [18], [21] and [23], none of the studies considered all feasible disturbances separately.
- Measurement errors have not been included in the study. These errors may appear from sensors or measuring devices.
- Most of the existing works primarily emphasise on the shape and characteristics of the distorted waveforms rather than identifying the root causes. However, pinpointing the root cause of the waveform distortion is essential, as it allows far quicker restoration of the system by addressing and eliminating the underlying disturbances.

After a few recent papers being reviewed, it has been seen that starting from sensing the power system quantities to the detection, the whole process comprises four major sections as shown in Figure 1.35. These are the Data Acquisition System (DAS), Data Processing (DP), Feature Extraction Process (EEP), and Classification Process (CP).

The distorted current and voltage signals have been sensed and tracked using the data acquisition arrangement (DAA). The raw signal contains noise in the form of high-frequency transients, errors caused by nonlinearity in the response of sensors, and unpredictable behaviour of the

power system. Hence, the detection of the actual shape of the disturbance waveform should be identified initially to detect every disturbance accurately.

The extensive use of power electronic controllers and devices by the generation, distribution, and load causes power quality issues to arise. The voltage and current waveforms at the point of common coupling (PCC) get distorted [29].

The contamination level on an outdoor insulator was recognised using a customized convolution neural network (CNN) model in [31]. Four different classes of contamination levels were chosen for classification.

Authors in [32] gave an idea of monitoring salt decomposition levels on an insulator surface, considering leakage current. They investigated time-frequency information obtained using wavelet transform for identifying surface conditions.

Pollution severity towards the occurrence of flash-overs was investigated using a CNN-BILSTM-based machine learning technique applied to infrared thermal (IRT) images of disc-type porcelain insulators [33].

Authors in [34] successfully proposed a KNN-based model using the EEG database of a hospital to predict the epilepsy of the patients. In this work, the statistical data of EEG waves have been taken as features.

In [35], the emotion of a person was recognized using a 3D-MLP-based neural network. The network was trained by EEG data of 23 people.

In [36] a novel method has been proposed for detecting Parkinson's Disease. The speech signals of patients were transformed into time-frequency information using wavelet synchro-squeezing transform to obtain the features. Finally, a Support Vector Machine (SVM) with a gradient boosting method-based model has been used for the classification.

The paper [37] proposed a multidimensional data space to quantify a particular disturbance by a deviation measure. A field programmable

gate array (FPGA) device was used to implement the proposed method. The deviation measure as an index quantifies the nature of the disturbance.

In [38], the authors generated the disturbance signals using formulae prescribed in IEEE std. 1159-2009 then applied the cross Stockwell transform on disturbance signals to obtain a time-frequency 2D image. In this process, the noises are reduced automatically. The deep features were taken from the outputs of four benchmark convolution Neural Networks, i.e. AlexNet, VggNet, ResNet and GoogleNet. Then Transfer Learning (TL) has been applied. Three advanced classifiers, i.e. Random Forest (RF), Support Vector Machine (SVM and k-nearest neighbours (KNN) were chosen and the performances were investigated.

The author in [11] predicted the future development in power distribution and proposed a decentralized power generation and management scheme. Accordingly, an overall concept of Distributed Generation (DG) technology has been delivered. Along with the advantages, a few problems have also been discussed.

A systematic review of a large number of articles was studied in [12] with the aim of establishing the research challenges in respect of the detection and classification of power quality disturbances in real-time microgrids.

In the article [13], the computational complexity associated with the conventional protection relay was mentioned and a novel algorithm known as mathematical morphology (MM) has been implemented to extract the shape-based characteristics of the signal for the detection of system abnormalities.

IEEE Recommended Practice for Monitoring Electric Power Quality, IEEE Standard 1159-2019, 2019.

In [39], more than 150 papers have been examined, and a few machine learning techniques have been suggested to automatically classify the power quality events. The presented methods have also been tested in

the noisy environment.

The usage of power electronic devices has expanded due to significant changes in the power system market, and this enhanced the amount of power used [40]. The need for green energy is felt globally, and the future of the smart grid. The inclusion of renewable energy sources into the distribution grid is the prime focus of today's utility companies. With the growing complexity of the power system, power utility companies are always expected to supply quality power. Any deviation of any of the power system quantities is called Power Quality Disturbance (PQD) [41]. These disturbances may result in failure of the system even total blackout. As a remedy, consumers are forced to install an Uninterrupted Power Supply (UPS), which is costly when the rating is too high.

The extensive use of power electronic devices, the integration of renewable energy sources, and their solid-state control devices produce harmonics in the system. It increases loss in the line, overheating of the connected equipment, and reduces equipment life span [42].

Besides, line faults, equipment faults and switching of compensating devices may also cause voltage sag, swell, flickering, impulse, unbalancing, etc.

In the last three decades, the remedies for these disturbances have been a growing concern for power researchers all over the world [43], [44].

Monitoring these aforesaid disturbances is a very tedious job. The measurement of all quantities and their analysis during any disturbance caused by sudden load change line or unit contingency makes the monitoring process complicated. With the advancement of high-end sensors, researchers are optimistic about measuring and recording the required quantities and are looking for smart tools and methodologies for a better understanding of system conditions that produce disturbances [45], [46], [47], [48], [49] and [50].

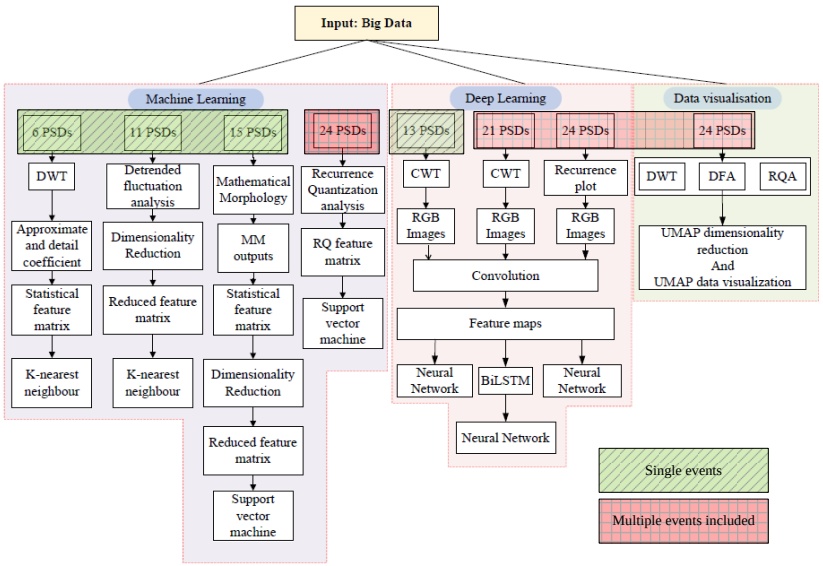

Figure 1.36: Overall work flow

1.7.1 Contributions of the present study in relation to the single power system events

After the scopes and opportunities had been sorted out, initially a laboratory-based experimental setup was prepared, where step by step a total of fifteen single events were conducted. The works with the single events have been depicted in Figure 1.36 by *green* hatched colour.

With the advancement of work, a few multi-event cases were considered and also a few more single-event cases, which are very common for the modern distribution system, have been included. These are depicted in the same figure using *red* hatched colour. Each column in Figure 1.36 signifies an independent research work. A total of eight outcome-based works have been carried out throughout the tenure. These have been

presented in subsequent chapters.

1.7.2 Contributions of the present study in relation to the multi-event cases

The presence of EV charging stations, sudden tripping of IM, abrupt load changes, scheduled and unscheduled islanding operations etc. increases the probability of multi-event occurrences. Therefore, in the latter stages of the work, a few multi-event phenomena have been added to the previously concluded single-event occurrences. With the increase in the number of categories, more advanced techniques were adopted for efficient classification. Even a few state-of-the-art techniques used in other fields have also been reviewed and applied to this field.

1.8 Organization of Thesis

This thesis has been organized in the following sequence:

Chapter 2 presents the experimental setup used to simulate and analyse power system disturbance events. It begins with an overview of the experimental arrangement, detailing the main power circuit, disturbance-creating mechanisms and the data acquisition unit. It further explains the generation of various disturbance events, including both single and dual disturbance types, which are critical for testing the reliability and response of power systems. These simulated scenarios help in understanding system weaknesses and improving monitoring strategies. The chapter concludes by summarising key observations from the generated disturbance events and their significance in power system research and development.

Chapter 3 focuses on the identification and classification of single power system disturbance (PSD) events using advanced signal pro-

cessing and machine learning techniques. It introduces three major approaches: DFA-based 1-NN robust classification, CWT-guided customized AlexNet CNN and mathematical morphology-based PCA-aided SVM. Each method includes detailed methodologies such as signal filtration, feature extraction, dimensionality reduction and classification. The chapter presents comparative results and discussions based on performance metrics and output data. Limitations of each method are also analysed. Overall, the chapter offers comprehensive insights into automated single PSD identification to enhance the accuracy and reliability of power system monitoring.

Chapter 4 explores the classification and identification of multiple power system disturbance (PSD) events using advanced deep learning and signal processing techniques. It begins with a CNN-aided tailored BiLSTM model that processes time-series data through feature extraction and classification stages. A second method employs recurrence plots with customised CNNs for visual and quantitative analysis of disturbances. The third approach integrates DWT, DFA and RQA features with UMAP for dimensionality reduction and visualisation. Each technique is thoroughly evaluated through performance metrics, comparisons with benchmark methods and robustness in noisy conditions. The chapter highlights the effectiveness of these models in multi-event PSD identification. In the concluding chapter, the overall work summary and its future scopes have been dealt with.

1.9 Originality of the Thesis

To the best of the author's knowledge, the following are the contributions that prove the originality of the work.

1. Design and development of a prototype experimental setup for generating both single and mixed power system disturbance events.

2. Designing robust machine learning and deep learning models for identifying commonly occurring distinct power system disturbances. As an outcome, four AI-based models — KNN, 1NN, CNN, and SVM — were developed.

3. Development of AI-based deep learning algorithms such as CNN-based BiLSTM and RP-based customised CNN for classification. These models are capable of classifying mixed disturbance categories with improved accuracy.

4. Development of a 2D data visualisation model for classifying mixed disturbance categories. A tuned UMAP model was employed to effectively cluster different classes in a 2D plot for better interpretation and understanding.

CHAPTER 2

Experimental Arrangement and Power System Disturbance Event Generation

2.1 Introduction

In the previous chapter, all commonly occurring power system events have been studied theoretically. Besides, a few articles have been reviewed thoroughly for finding out the recent trends in power systems, specially in the field of distribution protection. To proceed further with this knowledge, a laboratory-based experimental setup has been prepared to produce the disturbance-creating events as much as possible. This experimental setup has been modified over time by adding more disturbance-creating events, and the number of categories has been increased. In the following sections, this setup has been described, and the procedure of all event creation has been mentioned.

2.1.1 Experimental Arrangement for Generation of Power System Disturbance Events

The whole circuit has three major parts: the main power circuit (MPC), data acquisition system (DAS) and disturbance-creating arrangements (DCA).

2.1.1.1 Main power circuit

A 4-pole three-phase alternator has been used as a DG, and it has been operated by a separately excited DC motor of the same power rating. The ratings of all main circuit components are given in Table 2.1. Other than the prime-mover generator set, the power circuit comprises of resistive loads, inductive loads, capacitor banks, EV battery charging arrangements, a three-phase induction motor, a solid-state relay (SSR) and a grid-synchronisation arrangement. The complete circuit diagram has been shown in Figure 2.1. For stable operation of the DG, the rotational speed is kept constant at 1500 rpm by controlling the armature voltage of the DC motor, resulting in an output frequency of 50 Hz. A field exciter has been adjusted manually to maintain the terminal voltage of the DG by supplying the required VAR to the connected load. The main bus and DG bus have been synchronised using *two bright and one dark lamp* method. An extended common bus has been provided for connecting different types of loads, switching capacitor banks, charging batteries, and creating faults with the help of semi-automated solid-state relays (SSR). Initially starting from very few common switching and faults and then gradually increasing their variations, 25 different classes of events have been produced.

Table 2.1: Components Used in Hardware Setup

Components	**Range / Ratings**
Alternator	3 Ph, 50 Hz, 1500 rpm, 415 V, 1 kW
Exciter	I/P : 230 V, 50 Hz O/P : 220V dc
DC Motor	3 Ph, 220 V, 1500 rpm, 3 hp
DC Power Supply	I/P: 230 V, 1 ph, 50 Hz O/P: i) 220 V dc Excitation to the motor field ii) 220 V dc armature supply
Main Bus	50 Hz, 3 ph, Line Voltage = 415 V, Phase Voltage = 240 V
Grid	415 V, 50 Hz
Induction Motor (Local load)	3 Ph, 50 Hz, 1425 rpm, 415 V, 3 hp

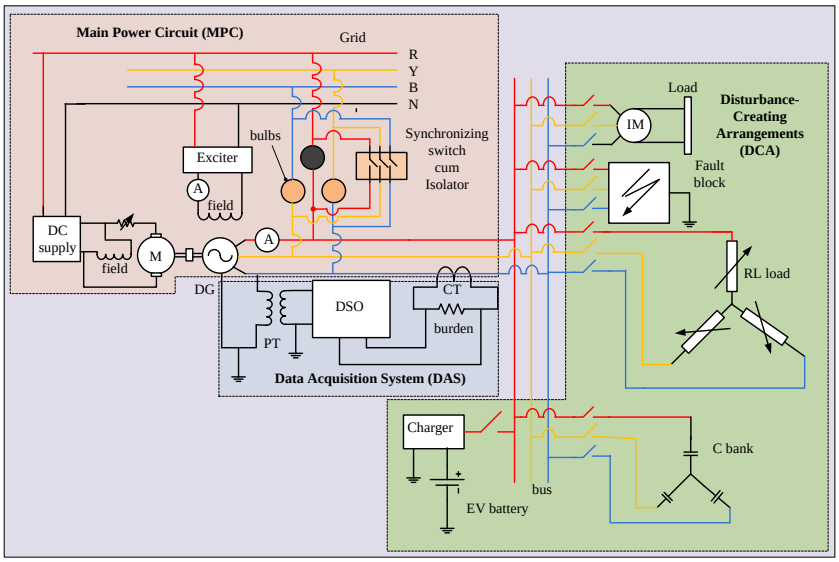

Figure 2.1: The composite circuit diagram

2.1.1.2 Disturbance-creating arrangements

Based on the considered category of PSD, the components, along with the semi-automated solid-state switching circuit, have been assembled and connected to the point of common coupling (PCC). The switching circuit comprises

- 25 A, Input: 4-32 VDC (4-16mA), PIV 800V, SSR
- Time delay circuit with push-to-on switch, and
- 9 V DC source.

2.1.1.3 Data Acquisition Unit

An electrically isolated Data Acquisition System (DAS) with ratings provided in Table 2.2 has been developed to acquire the phase voltage and line current sensed through the Potential Transformer (PT) and

Table 2.2: DAS Ratings

SL No.	Items	Range/Rating
1	PT	231/55 V, 1 kVA
2	CT	10/5 A, 5 VA
3	DSO	GDS-1022, 25 MHz, 250 M Sa/s
4	Burden	5 A, 10 Ohms

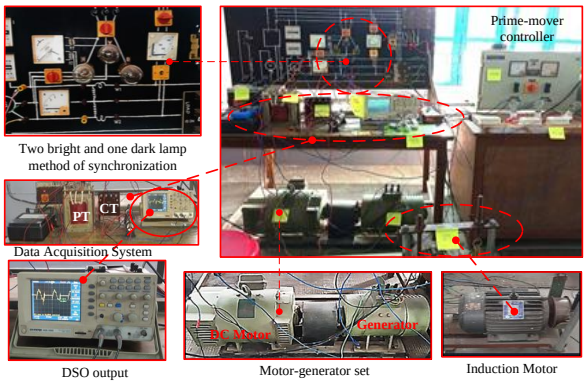

Figure 2.2: A complete hardware setup for PSD creation

Current Transformer (CT), respectively. The PT secondary has been directly fed to one channel of the digital storage oscilloscope (DSO), and the CT secondary has been shorted by a burden across which the other channel of the DSO has been connected. In this way, the acquired signals have been visually displayed on the DSO for their acceptability and recorded simultaneously in the hardware memory for further use. A complete hardware setup has been shown in Figure 2.2, where the enlarged views of all the major parts are adjacent to the main hardware circuit.

2.1.2 Generation of Different Power System Disturbance Events

At the initial stage of the work, only very few commonly occurring disturbances, as given in Table 2.3 have been created. As the research progresses, more feasible power system disturbances have been taken into account. This study has been conducted considering two different broad categorical classes–single power system disturbance events and mixed (single and dual) power system disturbance events.

2.1.2.1 Single Power System Disturbance Events

At the first stage, only six disturbance events comprising basic switching operations and faults have been considered as given in Table 2.3. The procedures are described below.

- **PSD 1: Capacitance Switching**

A three-phase star-connected capacitor bank has been formed using six identical 36 μF, 415 V, 1.95 VAR capacitors. Series and parallel combinations of two capacitors in each phase have been considered for the variation of VAR rating. Several case studies for this category have been executed under different loading conditions with variable RL load and induction motor. As mentioned in Table 2.3, the number of events could not be possible to take beyond 52 due to voltage instability issues at the PCC.

- **PSD 2: Line to Line Fault**

Before the switching operation is performed, a 100-ohm rheostat is brought in series with the SSR switch to ensure that the short circuit current does not cross double the DG current rating and also does not flow for more than 0.5 sec. In this way, the fault has been created for no load, static load, and induction motor loading conditions. Keeping the short circuit

current within the limit, 59 events have been possible to perform.

- **PSD 3: Line-Line to Ground Fault**

The connection has been kept as before with a series path comprising the combination of SSR and a rheostat that has been solidly fixed with common ground. A total of 100 cases were considered.

- **PSD 4: Three-Phase Fault at no load**

More than 100 cases were performed, keeping the voltage around 50% of the rated value. As the system is in a balanced condition, winding currents are easily anticipated. Three SSRs were connected in three conductors with a fault point resistance.

- **PSD 5: Reactor Switching**

Owing to the limited availability of the reactor coils, only 51 cases were generated.

- **PSD 6: Sudden Load Change**

The DG has been operated in isolated mode, and a three-phase induction motor has been connected to the PCC. The mechanical load on the induction motor (IM) has been varied. Not more than 47 events have been performed due to the motor halt at high load.

In the latter stages, more categories were included, keeping in view that in a practical grid-connected distribution system, the possibility of other classes occurring is very frequent, which cannot be ignored. Table 2.4, includes other considered categories, among which three categories have been further subdivided depending on the circuit conditions. A brief procedural step is described below.

- **PSD 7: Single Line to Ground Fault**

During a single-line to ground fault, a medium resistance is always kept

Table 2.3: Six commonly occurring power system disturbance events

Serial ID	PSD classes	No. of Events	Limitations
PSD1	Capacitance Switching	52	Voltage instability restricts large number of capacitors
PSD2	Line to Line Fault	59	The fault current has been kept within the rating of DG winding
PSD3	Line-Line to Ground Fault	100	Enough readings have been taken due to presence of neutral path
PSD4	Three-Phase Fault at no load	103	Readings were taken satisfactorily. keeping the terminal voltage 50% of rated
PSD5	Reactor Switching	51	Less number of readings due to unavailability of enough reactor
PSD6	Sudden Load Change	47	Induction motor loading could not be possible beyond the limit to avoid halt

in the fault path to limit the fault current. Due to thermal stress on the measuring and DG winding, a large number of events could not be taken.

- **PSD 8: Single-Phasing**

This is a very common open-type fault with only one phase getting disconnected. In the case of single-phasing, one SSR has been connected to one of the phase conductors and operated in reverse mode (i.e., push to make switching off). More than 100 case studies have easily been taken.

- **PSD 9: Mechanical input power interruption**

Mechanical input power to the shaft may be interrupted when the steam valve malfunctions, fuel input gets interrupted, or turbine blades break. This input interruption has been carried out by controlling the armature voltage of the DC motor using a regulator.

- **PSD 10: High Impedance Fault**

One of the most challenging tasks was conducting high impedance faults (HIF). As discussed in Chapter1, Section 1.4.1.5.2, HIF occurs when any of the line conductors touches the ground in different circumstances. This may happen when any object other than pure wet soil comes in between the ground and a live conductor of an overhead line. In the case of cable, due to partial damage to insulation, a small leakage current enters into the ground through the fault point. Depending on the object present at the fault point and its hygroscopic condition, the fault current is of very low magnitude. It is also associated with frequent weak arcs, resulting in nonlinearity in the current wave. Due to its diverse characteristics, detection is a challenging task. Still, its early detection is highly recommended for power system protection.
The DG terminal voltage is stepped up to the range of tens of kilovolts, and the live conductor of any phase has been made to touch a few objects on the earth's surface as shown in the circuit diagram in Figure 2.3. As

Table 2.4: Other possible power system disturbance events

Serial ID	**Categories**	**Sub-categories**	**No. of events**
PSD 7	Single line to ground (SLG) fault	• With isolated neutral	53
		• With neutral grounded	43
PSD 8	Single phasing	-	102
PSD 9	Input mechanical power interruption	-	100
PSD 10	High impedance fault (IIIF)	-	200
PSD 11	EV battery charging	-	101
PSD 12	Induction motor starting	-	102
PSD 13	Non-linear load	-	102
PSD 14	Islanding Operation	• With Generation greater than load	54
		• With Generation less than load	60
		• With Generation equal to load	101
PSD 15	Three phase fault	• At no load	103
		• With resistive load	103
		• With RL load	103

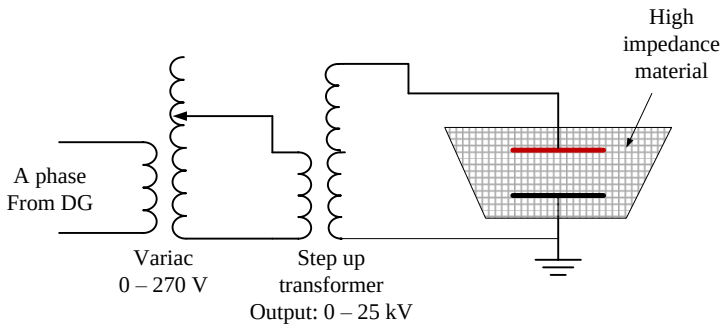

Figure 2.3: Circuit arrangement for HIF

specimens, the most commonly known objects, as shown in Figure 2.4 like wet leaf, dry leaf, sand, stone, soil, twig, etc., have been taken as the medium at the fault point for the HIF test in the laboratory.

- **PSD 11:EV battery charging**

Another important event that is very much concerned about the sustainability of the green transportation system. The provision for charging EV batteries at different nodes in a distribution system is highly recommended. Keeping these issues to be brought into the system, a battery with a charge controller has been connected through an SSR with a phase of the DG.

- **PSD 12: Induction motor starting**

An induction motor has been connected to the three phases of DG with three SSRs. With the help of a semi-automated switch, the motor has been started at different loads. This enables to take 102 readings.

- **PSD 13: Non-linear load**

A three-phase AC voltage regulator with a TRAIC switch has been connected to the power line to control a dimmer circuit. At different firing

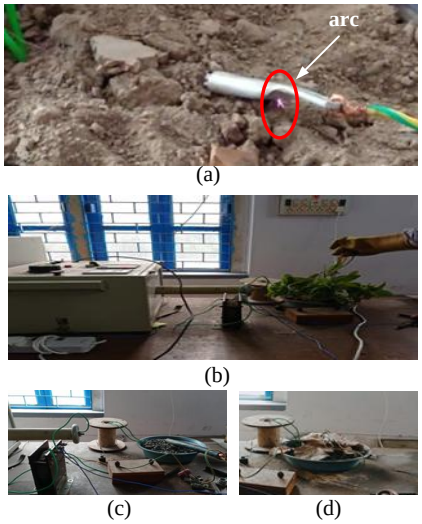

Figure 2.4: Experiment on HIF performed in the laboratory for different objects (a) Live broken conductor falling on soil producing arc (b) Full setup with green twig (c) HIF for Stones (d) HIF for dry leaves

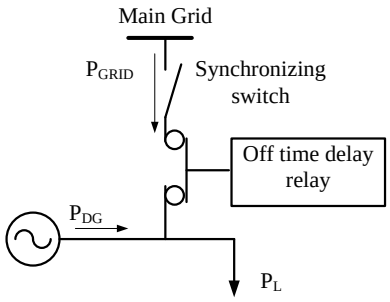

Figure 2.5: Power flow before islanding operation

angles and different load conditions, 103 events were successfully taken.

- **PSD 14: Islanding operation**

Before the islanding operation was performed, the DG was synchronized with the main grid using the conventional *two bright and one dark lamp* method. The following three conditions were set before the islanding operation with the power flows shown in Figure 2.5.

Condition 1: Generation (P_{DG})= connected load (P_L); hence, P_{grid}=0
Condition 2: Generation > load connected; hence, P_{GRID}=P_{DG}-P_L
Condition 3: Generation < load connected; hence, P_{GRID}=P_L-P_{DG}
Maintaining these three conditions, islanding operations were performed for different loading conditions. In all cases, power was noted using the $two-wattmeter$ method to ensure the above conditions. A total of 300 sets of voltage and current signals were recorded.

- **PSD 15: Three-phase fault for different power factors**

At the initial stage of the study, a three-phase fault was conducted at no load only. However, two more categories were added later, taking two more load conditions—resistive load and inductive load.

Table 2.5: Considered dual power system disturbance event cases in the study

Serial ID	Categories	No. of events
PSD 16	Islanding and EV charging	100
PSD 17	Islanding and load-shedding	102
PSD 18	Islanding and motor starting	103
PSD 19	Islanding and open circuit	102
PSD 20	Islanding and single phasing	102

2.1.2.2 Dual Power System Disturbance Events

As the research work progressed, the concept of dual events was brought into the study. This necessitated the data generation by creating two events simultaneously or one after another.

In all the dual events that have been considered here, the islanding operation has been taken as the common event, and five different events, which are not so dangerous unlike faults, have been associated with islanding to avoid any thermal breakdown and overcurrent for a longer period. These five dual events and their number of cases are given in Table 2.5.

- **PSD 16: Islanding and EV charging**

Initially the DG has been synchronised with the common grid and a normal operation was carried out. Suddenly, the islanding has been created using SSR, and the EV battery has been connected using another SSR to the PCC. These two events have been created randomly at the same instant or one after another, with microseconds time lag.

- **PSD 17: Islanding and Load Shedding**

As load shedding is a very usual power system practice when generation is less than the load demand, this event has been merged with the is-

landing operations.

- **PSD 18: Islanding and Motor Starting**

During large motor starting, a high load current flows through the line. This requires intentional or non-intentional grid synchronisation and/or islanding operations. These operations have been created randomly, and 103 readings were taken.

- **PSD 19: Islanding and Open Circuit**

The most common occurrences in power systems are the opening of phase conductors with a bus, which results from tripping a faulty line or intentional opening because of routine maintenance.

- **PSD 20: Islanding and Single Phasing**

The single phasing is very common when any of the phase conductors gets disconnected, keeping the other phases in a healthy condition. In this study, this event has been merged with the islanding operation.

2.2 Conclusions

The experimental setup simulates and records power system disturbances using a combined motor-generator system with a Data Acquisition System (DAS). It allows controlled creation of faults and transients, which are useful for training and testing algorithms that classify disturbances. The collected data helps in identifying and categorizing different types of power disturbances. This setup connects theoretical concepts with practical testing. The data obtained here is also used in the following chapters, which focus on the classification of power disturbances.

CHAPTER 3

Identification of Single Power System Disturbances

3.1 Introduction

In the initial stage of the work, the most commonly occurring Power System Disturbances (PSD) have been considered for their detection and classification with the help of the K Nearest Neighbour (KNN)-based Machine Learning (ML) technique. Experimentally created disturbance signals have been processed using Discrete Wavelet Transform (DWT) to obtain time and frequency domain information before they have been fed to KNN-based classifiers. The switching, line faults and load change have been chosen as root causes of disturbances. Later, another five single-type power system disturbances were included. Initially, valuable big data was filtered from the acquired signals using an unsupervised k-means clustering technique, followed by feature extraction through detrended fluctuation analysis (DFA). The feature matrix was then reduced by retaining only the most important principal components (PC) before applying the 1-Nearest Neighbour (1-NN) supervised ML algorithm. As the research progressed, more disturbances were taken into account, and

the classification algorithm was modified. The proposed algorithms with the increase of the single event disturbances have been presented in this chapter. In all cases, the performances of the used algorithms were evaluated and compared to other benchmark ML algorithms. In addition, the performance has also been examined in noisy environments.

3.2 Classification of Single PSD using DFA-based 1-NN Robust method

Previously few papers on the detection methods of various types of disturbances were published. In [51], the probabilistic approach in identifying the power system states was reported. George A *et al* [52] in their paper, presented harmonic power flow in traction-fed data using Fast Fourier Transform (FFT). In [53]-[54], power quality disturbances were investigated using wavelet transform. In [55], fuzzy-based technique to identify the types of disturbances has been applied. In [56], voltage disturbances were detected using S-transform on the data obtained from a Matlab-simulated transmission line model. In [57] authored by Gabor *et al*, a modified wavelet transform was introduced to identify voltage sags and swells. In [58], Hilbert Huang Transform (HHT) was used to investigate voltage behaviour due to different types of faults. Kaewarsa S *et al* in [59], successfully identified different faults in the simulated circuit using an artificial neural network (ANN) after the feature extraction from signals applying S-transform. In the above mentioned papers, the signals were taken from a simulation circuit. Though these signals are completely validated by theoretical concepts, but are less challenging. Whereas, signals recorded in our work were acquired from a real experimental test setup via a data acquisition system (DAS). These signals contain more noise. As a result, detection becomes more challenging.

The importance of distributed generator (DG)–based isolated power

systems has significantly grown due to the advancement of the power sector worldwide over the past few decades [60]. In this process of advancement, sensor technology, semiconductor switching technology, a lot of infrastructural developments, etc. have come into regular operation in power system network, which results in system operational complexity in terms of protection and reliability [11] and [61]. As a result, several unwanted disturbances (i.e., power system disturbance (PSD)) may occur in the power system, which usually may create different power quality issues that may hamper the safe operation of the power system network. Hence, the greater the system complexity, the more will be challenges for power engineers and researchers to keep the power system safe, well protected, and reliable [62] and [63]. In this context, several research articles have reported different power quality issues related to power system disturbances, such as islanding operations, switching, faults, etc. [64]. In this situation, it is yet to be mentioned here that to ensure the smooth and reliable operation of the power system and to deliver uninterrupted high-quality power, it is essential to smartly analyze all major disturbances that occur within such networks. For effective coordination and to prevent the malfunction of protective devices, the detection and classification of PSDs must be both rapid and precise. The progress in adaptive protection systems heavily relies on signal processing, where the key measurable parameters include the magnitude and phase angle of voltage and current signals, as well as the system frequency during disturbances, etc. Accurate extraction of these attributes is crucial for identifying PSDs correctly. In recent years, several algorithms have been developed for this purpose, including multi-cycle waveform analysis, deep convolutional methods with classifiers, and multiresolution decision tree-based approaches [65]. The use of modern algorithms such as S-transform, wavelet transform, SVM, ANN, CNN, fuzzy logic and their various hybrids, as well as complex combinations, has become increasingly prevalent, particularly in tasks related to signal processing

and classification for the detection and classification of several power system related problems [65]. Besides, mechanical and electrical faults of electric machines, like ball bearing faults and inter-turn faults, have been studied, and their severity has been judged using health indices and suitable machine learning algorithms [66]-[68]. In the field of power systems, different advanced signal processing techniques have been used to detect switching faults and power quality disturbances [69] and [70]. The initial step in any ML technique involves feature extraction from the data. Various publications have employed wave-shape analysis, signal processing, and Continuous Wavelet Transform (CWT)-based methods for feature extraction [14],[71]. However, those techniques have some potential limitations. The performance of the wavelet transform degrades with the noise. The S-transform has issues related to optimal window size selection, and also its performance is inefficient in cases of highly non-stationary signals. SVM may suffer due to overfitting tendency, and others have computational time burden issues as well as limited interpretability. However, Detrended Fluctuation Analysis (DFA) has become widely accepted for identifying long-range correlations in noisy and non-stationary time series [72]-[75]. It is particularly useful for analysing non-stationary signals due to its ability to remove trend-related fluctuations. In the case of different PSDs, which can introduce disturbances that are somewhat non-stationary in nature. In this work, the DFA technique has been used as an analytical tool for the identification of different features from the experimentally emulated different PSD events. It should be mentioned here that DFA has proven effective across various fields, including DNA sequence analysis, heart rate analysis, geological studies, ethnology, economic time-series investigation, solid-state physics, etc. [73]. This work specifically focuses on the fast and robust detection of common normal and abnormal operations in grid-connected microgrid (MG) systems, adhering to IEC Standard 60909-0:2016 during both the fabrication of the MG and the creation of relevant events [76].

For this purpose, a series of experiments were conducted to emulate different PSD events, and accordingly, the corresponding signals have been recorded for subsequent validation of the proposed method. It's important to note that PSDs can vary in nature, being either instantaneous, momentary, or continuous, and may also differ in severity. The main aim of this research section is to establish DFA as a robust tool for detecting different PSDs. Hence, in this work, DFA has been used for feature extraction from the recorded signals. Using DFA, subclasses are easily identified before the ML algorithm has been trained, unlike wavelet packet decomposition (WPD) or empirical mode decomposition (EMD). As all the disturbance signals of the MG network are non-stationary in nature, that is why those signals can be analysed using DFA effectively. Additionally, Principal Component Analysis (PCA) which is a popular technique for the identification of useful features based on principal components (PC), has been utilized to optimize memory usage and computational time by reducing the feature matrix [77]-[80]. For classification, a simple yet robust 1-nearest neighbour (1-NN) supervised method has been applied [81]. In this context, it should be mentioned here that efforts have been made in this work to include the commonly prevalent types of PSDs encountered in grid-connected MG systems. While the method may appear straightforward, its effectiveness in identifying PSD events has proven to be promising and comparable to the widely used methods currently applied for similar purposes.

3.2.1 Methodology of Single Power System Disturbance Events Identification

A laboratory-based micro-grid system has been prepared with a Distributed Generator (DG) supplying all possible kinds of load and compensating devices. The complete three-phase circuit diagram has been shown in Figure 2.1 of Chapter 2, Section 2.1.1.1 and also the pictorial

view of the whole experimental setup has been shown in Figure 2.2 of Chapter 2, Section 2.1.1.1.

A total of 11 individual PSDs were generated by varying the circuit conditions and the corresponding data has been stored at the PCC. Here, the most commonly occurring normal (N) and faulty (F) events have been considered. These power system disturbances (PSDs, from PSD1 to PSD11) are mentioned in Table 3.1. Among these, PSD4 and PSD11, i.e., input mechanical power interruption and islanding operations occur in the case of normal operation and during faults associated with the prime-mover and main grid.

The number of events in each PSD category could not be made the same. The number of switching (PSD1 and PSD6) and unbalanced fault events could not be increased due to the restrictions on loading and thermal stresses of the measuring instruments. All the acquired signals have been normalised to bring all the acquired data within unity resulting in uniformity among the data sets.

Each step has been depicted on the flow chart given in Figure 3.1. The normalised signal data contains informative and non-informative data. To filter out all non-informative data, each signal, known as the mother signal (MS), is segmented into sixteen child signals (CS), shape factors of each CS are calculated, and the k-mean clustering technique has been applied. The informative child signals (info-CS) are stored and added up to produce big data, which enables the classifier to be trained accurately.

3.2.1.1 Informative child signal filtration

Here, the k-mean unsupervised binary clustering technique has been used to filter out unwanted data points, and informative child signals (CS) are accumulated to form big data (BD)[71] for DFA feature matrix formation and classification. Big data generation serves two purposes in

Table 3.1: Single power system disturbances

Category code	**Name**	**Operational Mode**
PSD1	Capacitance switching	N
PSD2	Line to line fault	F
PSD3	Three phase fault with RL load	F
PSD4	Input mechanical power interruption	N/F
PSD5	Non-linear load	N
PSD6	Reactor switching	N
PSD7	Single line to ground fault with isolated neutral	F
PSD8	Single line to ground fault with neutral solidly grounded	F
PSD9	Sudden load variation	N
PSD10	EV battery charging	N
PSD11	Islanding operation	N/F

** N: Normal, F: Fault

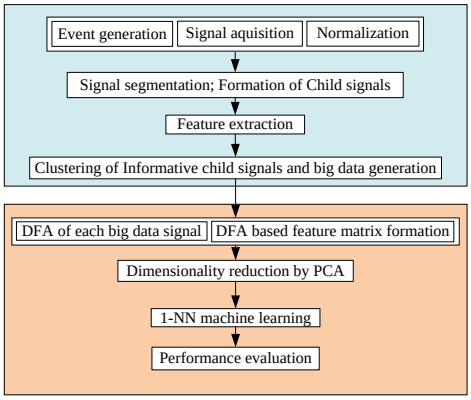

Figure 3.1: Step-by-step procedure of the whole process

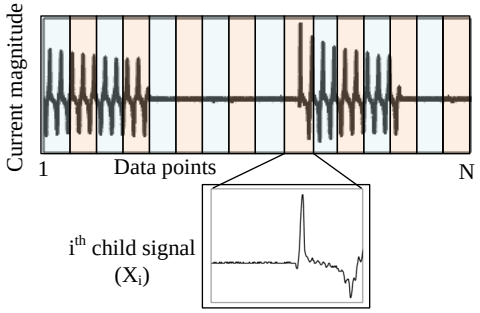

Figure 3.2: Child signal generation and their feature extraction

this study: to strengthen the input database and to provide a uniform number of data for each class of disturbance. This clustering technique has been applied to process the normalised raw signals and does not affect the main classification algorithm.

Each mother signal (MS) is divided into n child signals (CS) of w window-size as given in Equations (3.1) and (3.2) as presented in Figure 3.2 [71].

$$X_{MS} \in [X_{CS,1}, X_{CS,2}, ..., X_{CS,n}] \tag{3.1}$$

$$X_{MS} \in [X_{CS,informative}, X_{CS,non-informative}] \tag{3.2}$$

For the i^{th} child signal (CS_i), its data $X_{CS,i}$=$[x_1\ x_2\ \cdots\ x_w]^T$ are used to obtain statistical characteristics–rms value, peak value and shape factor (SF)–as given in Equations (3.3), (3.4) and (3.5). The feature matrix comprising these factors is used for the clustering process. The algorithm has been given in Table 3.2.

$$X_{rms,i} = \sqrt{\frac{1}{w}\sum_{k=1}^{w} x_k^2} \tag{3.3}$$

Table 3.2: Algorithm for informative child signals accumulation

Input: All mother signals
Output: Informative child signals
1. ***for loop*** j=1:1100
2. ***for loop*** i=1:n
Get features $[X_{rms,i}\ X_{avg,i}\ X_{SF,i}]$ using Equations (3.3), (3.4) and (3.5)
end loop 2.
Unsupervised binary k-mean clustering
end loop 1.
Accumulate all informative child signals

$$X_{avg,i} = \frac{1}{w}\sum_{k=1}^{w} x_k \tag{3.4}$$

$$X_{SF,i} = \frac{X_{rms,i}}{X_{avg,i}} \tag{3.5}$$

All informative child signals from all the recorded signals are accumulated to form Big Data (BD).

3.2.1.2 Detrended Fluctuation Analysis-based Feature Extraction

Detrended fluctuation analysis (DFA) has been carried out for each accumulated informative child signal to characterise the pattern of the signals in different categories. The fluctuation pattern across the window has been represented by three different frequency zone components as given in Table 3.3.

For a signal with data points, $\mathbf{X}$, the trending profile at any point k is given by Equation (3.6) [72] [73]. The actual signal x(k) and its trending profile y(k) have been clearly shown in Figure 3.3.

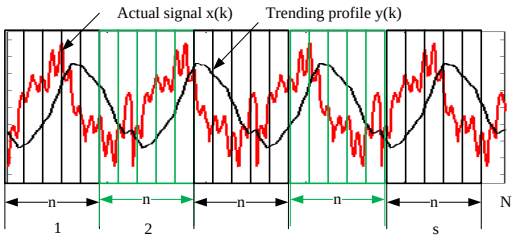

Figure 3.3: Processing of actual signal using DFA

$$y(k) = \sum_{i=1}^{k} [x(i) - \hat{x}] \tag{3.6}$$

As shown in Figure 3.3, the profile $y(k)$ has been divided into s number of non-overlapping windows of size n, so that the nearest integer of (N/n) is s and $(n \times s) \leq N$. The mean square fluctuation for m^{th} window $z(n, m)$ is given by Equation (3.7)

$$z(n, m) = \frac{1}{n} \sum_{m=1}^{s} \sum_{i=1}^{n} y_{i,m} \tag{3.7}$$

The RMS for a particular window size, n is calculated using Equation (3.8).

$$F(n) = \sqrt{\sum_{m=1}^{s} z(n, m)} \tag{3.8}$$

In DFA, the RMS value of the trending function $F(n)$ is expressed in terms of the power of window size n. Then taking log_e on both sides, the equation can be made linear as given in Equation (3.10) [72] [73].

$$F(n) \propto n^{\alpha} \tag{3.9}$$

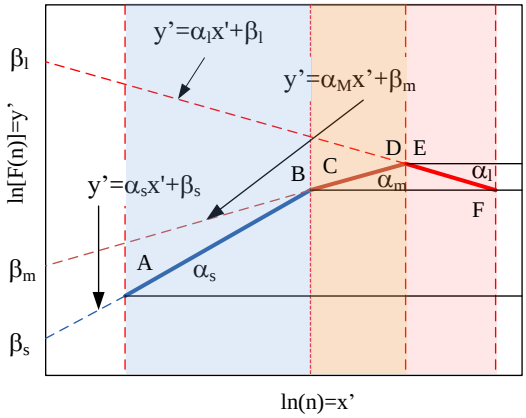

Figure 3.4: $ln[F(n)]$ versus $ln(n)$ linear curve for three different window size regions

Considering the proportionality constant, c, one gets $F(n) = cn^{\alpha}$ and hence Equation (3.11) is obtained, where $\beta = ln(c)$

$$ln[F(n)] = \alpha ln(n) + \beta \tag{3.10}$$

$$y' = \alpha x' + \beta \tag{3.11}$$

These linear equations have been obtained for three different window size zones corresponding to three different frequency zones for each signal, as shown in Figure 3.4. These linear equations of AB, CD and EF are characterised by their slopes (α_s, α_m and α_l), intersection with $ln[F(n)]$ (β_s, β_m and β_l) and the dimension of the time series (D). These characteristic features have been calculated using the formulae mentioned in Table 3.3. The algorithm used to extract the DFA feature matrix from all the acquired signals is presented in Table 3.4.

Table 3.3: Seven Characteristics Features of DFA

Characteristics features	Nomenclature	*Used Formulae*	*Window size*
Dimension of the time series	D	$3-\alpha_s$	–
Slope	α_s	$\frac{ln[F(n_{s,max})]-ln[F(n_{s,min})]}{ln(n_{s,max})-ln(n_{s,min})}$	$n_{s,min}<n<n_{s,max}$
	α_m	$\frac{ln[F(n_{m,max})]-ln[F(n_{m,min})]}{ln(n_{m,max})-ln(n_{m,min})}$	$n_{m,min}<n<n_{m,max}$
	α_l	$\frac{ln[F(n_{l,max})]-ln[F(n_{l,min})]}{ln(n_{l,max})-ln(n_{l,min})}$	$n_{l,min}<n<n_{l,max}$
Point of intersection with ln[F(n)]	β_s	$ln[F_s(1)]$	$n_{s,min}<n<n_{s,max}$
	β_m	$ln[F_m(1)]$	$n_{m,min}<n<n_{m,max}$
	β_l	$ln[F_l(1)]$	$n_{l,min}<n<n_{l,max}$

Table 3.4: Algorithm to extract DFA features of the signals

Input : $\mathbf{X} = [x_1\ x_2\ x_i\ \cdots\ x_N]^T$
Output : $X_{DFA} = [D\ \alpha_s\ \alpha_m\ \alpha_l\ \beta_s\ \beta_m\ \beta_l]$
To determine the trended profile y(k) using Equation (3.6)
1. for k=1 to N
2. for i=1 to k
sum=sum+x(i)-$\bar{x}$
end for loop 2
y(k)=sum
end for loop 1
To determine the mean square fluctuation z(n,m) of the profile y(k) using Equation (3.7)
3. for m=1 to s
4. for i=1 to n
sum1=sum1+y(i,m)*y(i,m)
end for loop 4
z(n,m)=$\frac{sum1}{n}$
end for loop 3
z(n,1), z(n,2) $\cdots$ z(n,s)
To find RMS for all sub-series of length n, F(n) using Equation (3.8)
5. for n=n_{min} to n_{max}
6. for m=1 to s
sum2=sum2+$[z(n,m)]^{0.5}$
end for loop 6
F(n)=sum2
end for loop 5
To construct a linear equation using Equations (3.9),(3.10) and (3.11) and to find the features of ln(F(n))=α ln(n)+β
Linear equation: ln(F(n))=α ln(n)+β
Window sizes: $n_{s,min} < n_s < n_{s,max}$, $n_{m,min} < n_m < n_{m,max}$ and $n_{l,min} < n_l < n_{l,max}$
$\alpha_s = \frac{ln[F(n_{s,max})] - ln[F(n_{s,min})]}{ln(n_{s,max}) - ln(n_{s,min})}$ and $\beta_s = \ln[F_s(1)]$ for $n_{s,min} < n_s < n_{s,max}$
$\alpha_m = \frac{ln[F(n_{m,max})] - ln[F(n_{m,min})]}{ln(n_{m,max}) - ln(n_{m,min})}$ and $\beta_m = \ln[F_m(1)]$ for $n_{m,min} < n_m < n_{m,max}$
$\alpha_l = \frac{ln[F(n_{l,max})] - ln[F(n_{l,min})]}{ln(n_{l,max}) - ln(n_{l,min})}$ and $\beta_l = \ln[F_l(1)]$ for $n_{l,min} < n_l < n_{l,max}$ and
D=3-α_s

3.2.1.3 Dimensionality Reduction using PCA

These DFA features are highly correlated, which needs unnecessary memory consumption and acts as a burden in the classification process. This issue has been handled using the straightforward PCA technique. Since a huge number of case studies have been performed on experimental setups, the data sets have become deterministic. The authors in [82], used probabilistic PCA, where it is required to interpret the probable data. In PCA, an equal number of uncorrelated PCs are formed using a linear combination of all seven DFA features [77] [83]. Arranging those PCs in descending order, the first four significant PCs are considered. This reduces the dimension of the feature matrix, and machine learning-based classifiers can effectively be trained with this reduced matrix to obtain a higher accuracy level.

As discussed in [84] the i^{th} PC is given by Equation (3.12).

$$\begin{aligned} PC_i = \mathbf{a_i^{'}} \mathbf{X}_{DFA} = & a_{i1}D + a_{i2}\alpha_s + a_{i3}\alpha_m + a_{i4}\alpha_l + a_{i5}\beta_s + \\ & a_{i6}\beta_m + a_{i7}\beta_l \end{aligned} \tag{3.12}$$

For the PC_i to have maximum variance, $\mathbf{a_i^{'}} \mathbf{\Sigma}\ \mathbf{a}_i$ must be maximum, subject to $\mathbf{a_i^{'}} \mathbf{a_i}$=1, where Σ is the covariance of the original variables $\mathbf{X}_{DFA}$ and has given in as

$$\Sigma = \begin{bmatrix} \text{var}\,(D) & \text{cov}\,(D, \alpha_s) & \cdots & \text{cov}\,(D, \alpha_l) \\ \vdots & \text{var}\,(\alpha_s) & & \vdots \\ \text{cov}\,(\alpha_l, D) & \cdots & & \text{var}\,(\alpha_l) \end{bmatrix} \tag{3.13}$$

$$\text{var}\,(x_i) = \frac{\sum_{k=1}^{n} (x_{i,k} - \overline{x_i})^2}{n-1} \tag{3.14}$$

$$\text{cov}\,(x_i, x_j) = \frac{\sum_{k=1}^{n} (x_{i,k} - \overline{x_i})(x_{j,k} - \overline{x_j})}{n-1} \tag{3.15}$$

for i and $j = 1, 2 \ldots\ldots\ldots 7$ but $i \neq j$. Here, $x_i \in \mathbf{X}_{DFA}$

The *Lagrange* function has been formed as

$$L = \mathbf{a}_i^{'}\boldsymbol{\Sigma} \;\; \mathbf{a}_i - \lambda(\mathbf{a}_\mathbf{i}^{'}\mathbf{a}_\mathbf{i} - 1) \tag{3.16}$$

After differentiation with respect to $a_\mathbf{i}$ one gets

$$(\boldsymbol{\Sigma} - \lambda\mathbf{I}_\mathbf{p})\,\mathbf{a}_\mathbf{i} = 0 \tag{3.17}$$

Where λ is eigenvalue of Σ, $\mathbf{a_i}$ is the corresponding eigenvector and $\mathbf{I_p}$ is identity matrix. The variances of PCs are investigated with the help of PC loading and *scree* plot which have been shown in the result section.

3.2.1.4 Classification using 1-nearest neighbour (1-NN) machine learning technique

In this study, the K-nearest neighbour-based machine learning has been adopted for its simple detection technique without any pre-trained classifier model and has been presented in Table 3.5. It only requires the recognisable training dataset memory [81]. The Euclidean distance of the test data from all the training datasets as shown in Figure 3.5 is calculated using Equation (3.18) and a single nearest data point from the test data is considered the best nearest neighbour and the test data point is assigned to be a member of the same category.

$$ED_{j,test} = \sqrt{\sum_{i=1}^{4}(PC_{i,j} - PC_{i,test})^2} \tag{3.18}$$

Table 3.5: Algorithm for test signal prediction

Memory: Training datasets **Input:** Test data
Output: 1-NN and its category
1. for loop j=1:1100 Calculate $ED_{j,test}$ using Equation (3.18) End loop 1.
To determine 1-NN and its category
1-NN=Minimum [$ED_{j,test}$; j $\forall$ 1 to 1100]

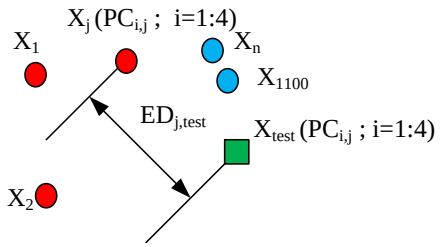

Figure 3.5: Euclidean distance between test and training data

3.2.2 Results and Discussions

As already mentioned, the commonly occurring power system phenomena have been considered here for producing categorically 11 different disturbance signals. Due to restrictions on equipment and instruments' current and thermal ratings, the conducted experiments were not the same for all 11 disturbances. Switching and single-line-to-ground fault events have not been conducted more than 50 times due to the aforementioned restrictions. The results have been shown in subsequent sections.

3.2.2.1 Big data generation as an output of k-mean clustering

The number of mother signals (MSs) produced by the experiments for different categories is presented in Figure 3.6. Three types of disturbances, like a three-phase fault with RL load (PSD3), non-linear load (PSD5) and EV battery charging (PSD10) were possible to conduct 106,102 and 104 times, respectively. Whereas, the number of experiments performed for other PSDs ranges from 43 to 74, as shown in Figure 3.6. A total of 735 events have been created. As mentioned in the theory section, all 4000 data points of a particular MS, have been divided into 16 equal-sized CSs before k-mean unsupervised clustering was performed. Table 3.6 presents the shape factor matrix for 735 mother signals; however, it is displayed in truncated form here due to its large actual size.

Here, in Figure 3.7 (a), a normalized current signal of 4000 data points during a capacitance switching event (PSD1) has been divided into 16 CSs. It is easily observed that the first 45% contains information about the disturbance, and it is also obvious from Figure 3.7(b) that seven child signals in the first seven sub-windows have a shape factor (SF) greater than 1.0.

After filtering out unwanted CS from all 735 mother signals. 1540

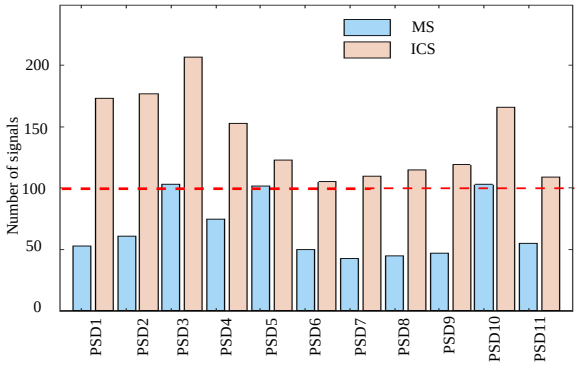

Figure 3.6: Number of big and informative data in comparison with mother signals

informative CS data signals were obtained. Data generation from MS ranges from 107 to 201. To maintain uniformity in the training data, a rounding down value of 100 for each category has been considered as shown by the red dotted lines in Figure 3.6.

3.2.2.2 DFA feature matrix

The accumulated data for each category has been used to represent the trending profile of the signal in terms of DFA attributes. Here, in Figure 3.8, one signal from each category and its respective DFA plot have been clearly depicted to visualize their DFA plot variations in three different window-size ranges as mentioned in Table 3.7.

Besides, all these DFA plots for different disturbance categories have been shown using *log-log* graph in Figure 3.9. It is obvious from this graph that these 11 categories fall under 5 major sub-bands in terms of their low-frequency and medium-frequency contents, i.e., PSD(2,6,9), PSD(5,3), PSD(1,4), PSD(7,8) and PSD(10,11) but they differ when their high-frequency contents are chosen. These high-frequency con-

Table 3.6: Shape factors of sixteen child signals for all 1100 events

	E1	E2			E735
SF1	1.8117	2.6603	--------	-------	1.6687
SF2	2.1052	2.244	--------	-------	1.0515
SF3	1.7173	1.3941	------	-------	1.0619
⋮	⋮	⋮	⋱		⋮
SF13	1.9415	1.5757	-------	-------	1.0451
SF14	1.2241	1.3555	-------	-------	1.0419
SF15	1.3154	1.4332	-------	-------	1.0427
SF16	2.2101	2.4722	-------	-------	1.0593
					(16×735)

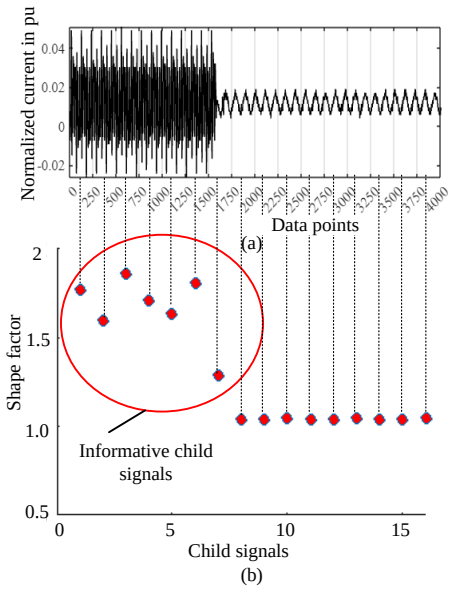

Figure 3.7: (a) Normalized current signal for the capacitance switching event (PSD1) and sub-window partitions (b) informative child signals filtration after k-mean clustering

Table 3.7: Three window ranges and corresponding frequency components

Frequency components	window range
High	4 to 108
Medium	108 to 316
Low	316 to 500

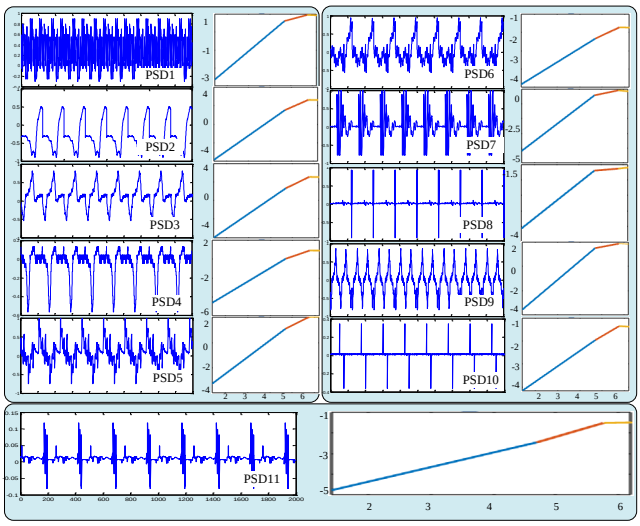

Figure 3.8: One signal from each power system disturbance and their DFA plots

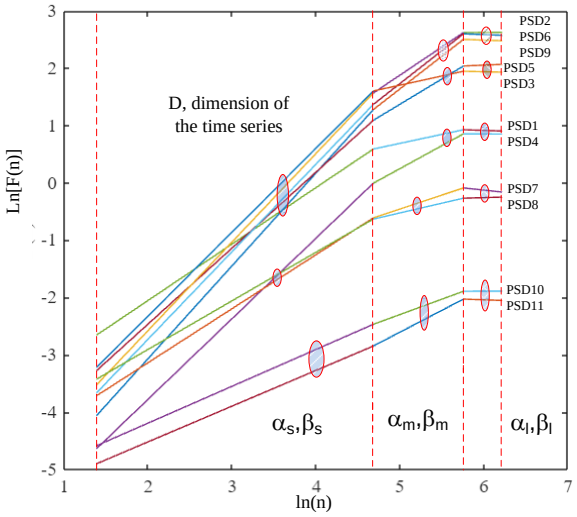

Figure 3.9: DFA plots of eleven different PSDs.

tain three different sub-bands, i.e. PSD (2,6,9,5, 3,1), PSD(4,7,8) and PSD(10,11)

The linear characteristics of all 1100 DFA plots have been specified by 1100× 7 feature matrix as shown in Table 3.8 in reduced form due to its large actual size. The corresponding *box* plots for all seven features have also been shown in Figure 3.10 to investigate the distribution of feature variables and their pattern.

3.2.2.3 Reduced Feature Matrix

To obtain the principal components (PCs), a covariance matrix has been formed and this is given in Table 3.9. Using this covariance matrix, all PCs were calculated as shown in Figure 3.11 (b) and eigenvalues along the principal major axes were also been obtained to observe the PC loading as given in Figure 3.11(a). The first 4 PCs contribute 100%

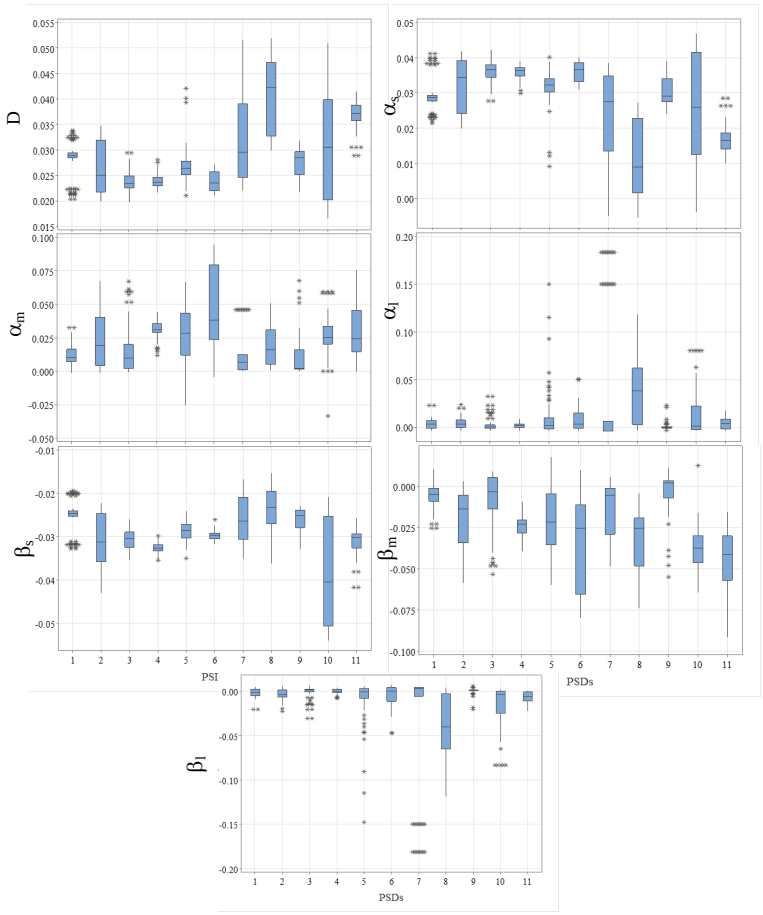

Figure 3.10: Box-plot of all seven DFA features showing their variances.

Table 3.8: 1100×7 feature matrix

	D	α1	α2	α3	β1	β2	β3
E1	1.98	1.02	0.0618	-0.1456	-4.112	0.3742	1.4852
E2	1.9982	1.0018	0.0835	0.2247	-4.0221	0.2778	-0.4789
	⋮	⋮	⋮	⋮	⋮	⋮	⋮
E501	1.4057	1.5943	0.917	2.3903	-6.0602	-2.8887	-10.7808
E502	1.6529	1.3471	2.7409	-0.1639	-5.7649	-12.2908	3.2692
	⋮	⋮	⋮	⋮	⋮	⋮	⋮
E1099	1.7939	1.2061	1.0571	0.6335	-8.2948	-7.5974	-5.328
E1100	2.4951	0.5049	0.0683	-0.108	-6.0218	-3.9774	-3.0333

Table 3.9: 7×7 Covariance matrix

$$\boldsymbol{\Sigma} = \begin{bmatrix} -0.117 & 0.015 & 0.473 & 0.023 & 0.132 & 0.797 & -0.329 \\ 0.172 & -0.022 & -0.697 & -0.034 & 0.621 & 0.296 & -0.101 \\ 0.051 & 0.692 & -0.272 & 0.507 & -0.365 & 0.225 & 0.058 \\ -0.681 & -0.037 & -0.227 & 0.126 & -0.06 & -0.223 & -0.643 \\ -0.046 & -0.063 & 0.308 & 0.734 & 0.534 & -0.247 & 0.123 \\ 0.111 & -0.717 & -0.241 & 0.424 & -0.415 & 0.248 & 0.045 \\ 0.69 & 0.032 & 0.108 & 0.08 & -0.062 & -0.232 & -0.669 \end{bmatrix}$$

of loading without potential information loss and the *scree* plot also suggests that the dimension can be brought down to 4 as indicated by the coloured 1100×4 matrix.

3.2.2.4 Prediction using 1-NN

Using 10-fold cross-validation, 97.18% accuracy level has been achieved as presented in Table 3.10. 1-NN accuracy level and miss-classified events are clearly depicted by *circos* plot in Figure 3.12. The evaluation matrix in terms of specificity, precision, recall. f1-score, sensitivity and accuracy has been computed and displayed in Figure 3.13.

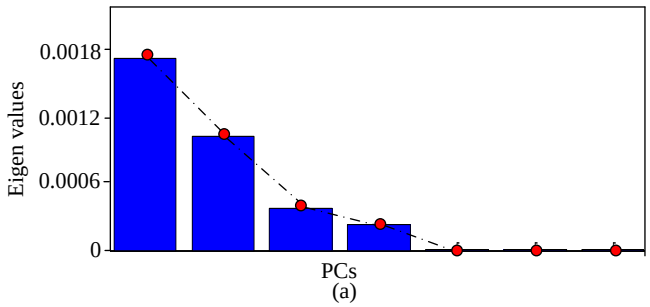

	PC1	PC2	PC3	PC4	PC5	PC6	PC7
E1	0.0039	0.0011	-0.0088	-0.0132	0.0064	0.0385	-0.0159
E2	0.0000	0.0019	-0.0092	-0.0127	0.0063	0.0385	-0.0159
E501	-0.0617	-0.0122	-0.0393	-0.0176	0.0063	0.0385	-0.0159
E502	-0.0175	0.0345	-0.0347	-0.0143	0.0063	0.0385	-0.0159
E1099	-0.0083	0.0606	-0.0191	-0.0333	0.0064	0.0385	-0.0159
E1100	-0.0062	0.0217	0.0064	-0.0317	0.0064	0.0385	-0.0159
				1100*4			1100*7

(b)

Figure 3.11: (a) Scree plot and corresponding principal component loading (b) principal components

Table 3.10: Overall accuracy and relative computational time (RCT) comparison with other benchmark methods

Method	Without PCA		With PCA	
	accuracy in %	RCT in pu	accuracy in %	RCT in pu
Gaussian SVM	89.03	1.23	90.20	1.14
Decision tree	86.00	1.66	86.00	1.43
Ensemble bagged tree	89.00	1.35	90.03	1.23
Random forest	92.10	1.97	92.54	1.77
CNN	92.40	2.07	93.45	1.92
1-NN	96.34	1.01	97.18	1

This DFA-PCA-based 1-NN method has been compared with other modern machine learning and deep learning methods like SVM, decision tree (DT), ensemble bagged tree (EBT), random forest (RF), and CNN. Their class-wise accuracy has been shown in Figure 3.14.

The overall accuracy and respective relative computational time (RCT) have also been presented in Table 3.10. Here the processing time of this proposed method has been taken as unity and all others' computational times have been expressed in pu value with respect to this 1-NN method. It is observed from Figure 3.14 and Table 3.10, that 1-NN can classify the disturbances with the highest accuracy in lower detection time. Since the DFA-based feature extraction method already, segregates the disturbances before training the classifier, this high level of accuracy can be achieved. PCA also contributes to obtaining such higher accuracy, as per Table 3.10, where the results without using PCA have been portrayed.

In Table 3.12, the proposed method has been compared with some state-of-the-art methods used in [26], [15] and [23]. The novelty in this work is that all the disturbances have been created from a hardware

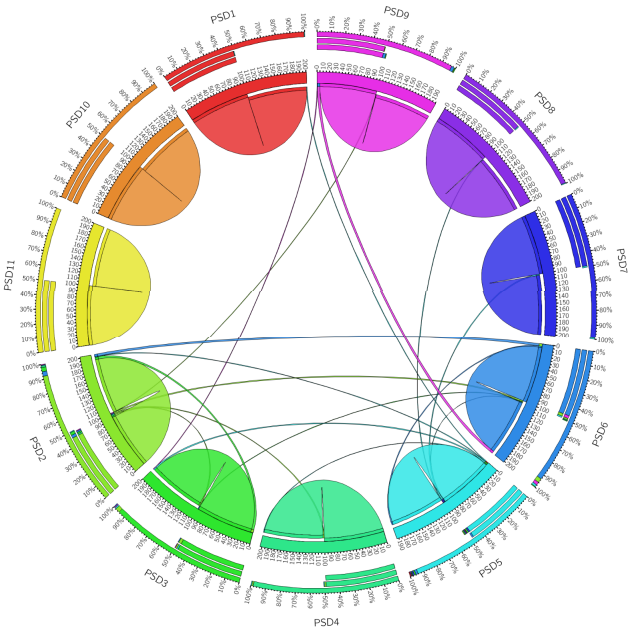

Figure 3.12: Circos plot showing all miss-classifications

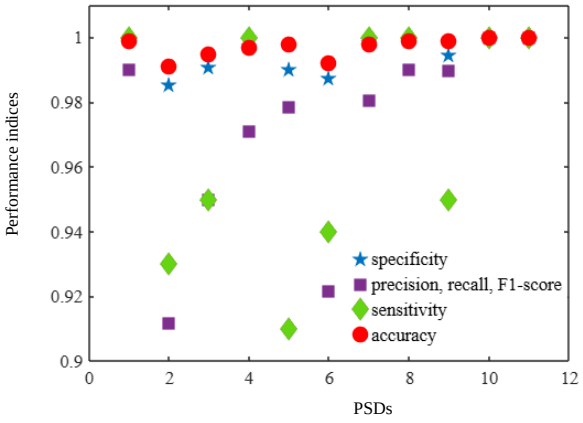

Figure 3.13: Class-wise performance indices.

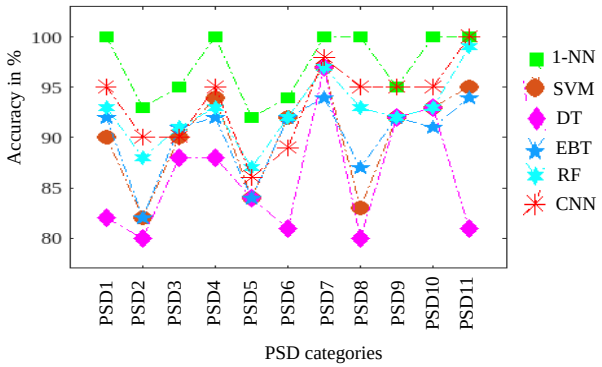

Figure 3.14: Class-wise accuracy comparison with other benchmark machine learning

Table 3.11: Accuaracy level under noisy environment

Noise level (in dB)	Accuracy (in %)			
	Gaussian SVM	Decision tree	Ensemble bagged tree	1-NN
20	88.00	80.80	86	90.10
30	88.90	81.03	87.10	92.20
40	89.01	83.40	87.20	94.34
50	89.30	85.62	89.03	96.50
60	90.20	86.00	89.70	97.01
Raw signals	90.20	86.00	90.03	97.18

experimental setup, and different types of power system operations like, switching, islanding and faults have been considered.

As the disturbances have been created using a laboratory-based practical grid-connected DG system, some random and undefined noises are present in the acquired signals. Though, the study has been performed using those practical noisy signals, still its performance has been assessed by adding different accountable noise level up to 20 dB. The performances at different SNR (signal-to-noise ratio) have been presented in Table 3.11. This proposed method provides a satisfactory performance of 90% accuracy even in highly noisy environments.

3.3 Classification of Single PSD using CWT Guided Customized AlexNet CNN

This work aims at designing a Convolution Neural Network (CNN) based classifier that detects and classifies thirteen different types of power system disturbances. The whole process comprises of a couple of steps. Initially, the disturbance current signals were sensed from the experimental setup. The filtration by unsupervised k-mean Machine Learning (ML) has been performed to remove noisy data and to obtain big data. The architecture of AlexNet CNN has been modified, and the time-frequency informative images have been created using Continuous Wavelet Transform (CWT). The convolution has been performed using kernels to obtain feature maps. The forward-backward propagation algorithm has been used to optimise the hyperparameters. Finally, the *softmax* activation function categorises the classes. The proposed customized CNN has been compared with other benchmark CNN architectures. The method has shown 98.46% accuracy with minimum computational time.

The classification study of almost all possible power system distur-

Table 3.12: Comparison with few state-of-the-art methods

Ref.	**Number /Origin / Type**	**Feature extraction method**	**Classifier**	**Accuracy in %**	**Novelty**
[26]	10/ PSCAD simulated / Faults	Ensemble empirical mode decomposition (EEMD) + CNN	LSTM	96.89	State-of-the-art techniques
[15]	15 Simulated signals	Gabor filter guided	Softmax	97.00	State-of-the-art techniques
[23]	8 events and their combinations / Programmable / ac generator	Stockwell Tranform guided	Neural Network	98.25	State-of-the-art techniques
Proposed work	11 exclusively different / Practical Laboratory setup / Switching Islanding Faults	DFA	1-NN	97.18	Simple and Robust Less computational time

bances is challenging in a decentralised modern power distribution network. Due to the diversity in generation technology and bidirectional flow of current, the conventional method of fault analysis fails [85], [86] and [87]. The classification study of other disturbances, unlike fault, i.e., capacitor, or inductor switching, nonlinear load switching, mechanical power interruption, islanding from utility, etc., which are equally significant to supply reliable and quality power to the consumer [88] and [89]. Power quality disturbance classification using Convolution auto-encoder network and Stockwell Transform (ST) guided deep learning techniques was addressed in [15] and [23], respectively. In some previous literature, from [62] to [90], the study of islanding detection, fault classification, high impedance fault detection etc. have been addressed. In [91] and [92], the combination of two, three or four different types of disturbances have been reported.

The synthetic signals have been used in most of the articles for classification studies [93] and [64].

In [64] the CNN method has been proposed using the Hilbert Huang transform for fault classification in the power distribution network.

In this study, the AlexNet has been considered as the basic network for its straightforward architecture, faster convergence capability with proper learning rate and batch size and parallelization ability with Graphics Processing Unit (GPU) [94, 95]. This CNN has been customized by manual tuning of a few deciding parameters and by varying the architecture of the input layer and last three layers as described in the classification section. The performance of the classifier has been evaluated both in the absence of noise and under various noisy conditions.

Thirteen different classes of disturbances (CD) from CD1 to CD13 as mentioned in Table. 3.13 have been created. To create a high impedance fault (CD2), naturally available materials like soil, sand, stone, twigs, dry leaves etc. have been used as the contact surface of a broken conductor [96].

Table 3.13: Classes of Disturbances

Code	**Class**	**Code**	**Class**
CD1	VAR compensating device switching	CD8	Non-linear load
CD2	High Impedance Fault	CD9	Reactor coil switching
CD3	Sudden disconnection from grid	CD10	Single line to ground fault
CD4	Line to line fault	CD11	Single line to ground fault with grounded neutral
CD5	Line line to ground fault	CD12	Induction motor single phasing
CD6	Three phase fault	CD13	Load demand fluctuation
CD7	Prime mover decoupling		

3.3.1 Methodology of Single Power System Disturbance Events Identification

The recorded data are processed through the following steps.

• Filtration and big data generation using unsupervised k-mean clustering.

• 2-D Scalogram for time-frequency information using continuous wavelet transform

• Feature extraction and classification using customized proposed CNN.

3.3.1.1 Filtration using Data Clustering

In this step, the entire set of data points from each signal, referred to as the mother signal (MS), is divided into n child signals (CS).

$$X_{MS} \in [X_{CS,1}, X_{CS,2}, ..., X_{CS,n}] \tag{3.19}$$

$$X_{MS} \in [X_{CS,informative}, X_{CS,non-informative}] \tag{3.20}$$

Unsupervised k-mean clustering techniques has been used to segregate informative and non-informative child signals for each mother signal. All informative child signals extracted from the recorded signals are aggregated to form big data (BD).

Here, the statistical features – shape factor, rms value and peak value have been taken as variables for each child signal.

3.3.1.2 Time-Frequency Schelogram Conversion

In this part, the time and frequency domain information in the form of a scalogram have been obtained using (CWT) as given in Equation (3.21). Each child signal, $x(t)$ is transformed into a wavelet function, W_x using a mother wavelet function $\psi(t)$. Here, a is the scale factor and b is the shifting operator. The schalograms so obtained have been converted to images in a MATLAB environment.

$$W_x(a,b) = \frac{1}{\sqrt{a}} \int_{-\infty}^{\infty} x(t)\hat{\psi}\left(\frac{t-b}{a}\right) dt \tag{3.21}$$

Here, $\hat{\psi}(t)$ is dual function of $\psi(t)$.

3.3.1.3 Classification by Convolution Neural Network

The total images have been divided into 80% training set and 20% validation set. Initially, to make the network architecture compatible,

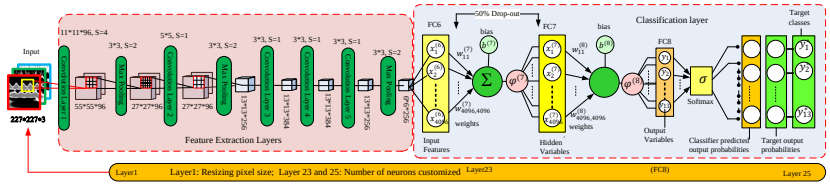

Figure 3.15: Proposed customized CNN

Table 3.14: Tuned Hyper-parameters

Hyper-parameters	Values	Hyper-parameters	Values
Batch size	30	Number of epochs	6
Learning rate	0.0003	Validation frequency	43
Optimizer	sgdm		

the five important parameters i.e. learning rate (LR), batch size, number of epochs and optimiser have been tuned as shown in Table 3.14. The convergence, computational time, memory requirement and accuracy depend on those parameters. The complete process comprises the following steps, as depicted in Figure 3.15.

3.3.1.4 Customization of AlexNet

The images are fed to the input layer of the Neural Network (NN) in a number of batches. The images have been resized to 227×227 and divided into three channels– *Red*, *Green* and *Blue* to comply with the requirement of the input layer. As a base network, AlexNet has been considered and its architecture has been customized as per the requirements. The hyper-parameters have been tuned manually at a value given in Table. 3.14 to obtain the maximum accuracy.

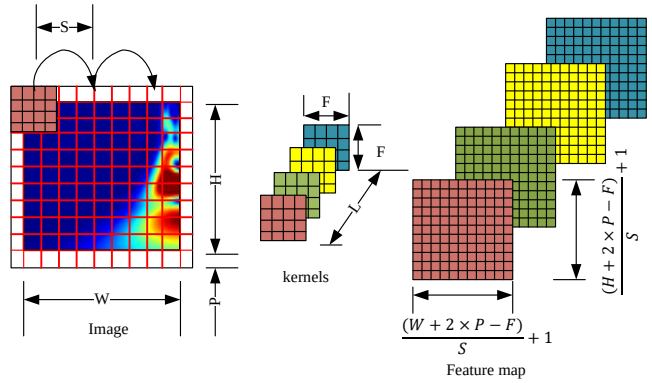

Figure 3.16: Feature extraction by convolution in hidden layers

3.3.1.5 Feature Extraction by Convolution

The complete architecture of this customized CNN with five convolution layers, three pooling layers, three fully connected layers (FC6, FC7 and FC8) and *softmax* activation layer has been clearly shown in Figure 3.15. Sizes of all layers are also mentioned in this figure. The convolution layer is always followed by pooling layer. Here, 3×3 max-pooling with stride of 2 has been used to extract features. As depicted in Figure 3.16, an image matrix, $\mathbf{X} \in \mathbb{R}^{W\times H\times 3}$ has been padded with P number of dummy pixels around its boundary. It results in $\mathbf{X}_p \in \mathbb{R}^{(W+2P)\times(H+2P)\times 3}$. When the filter $f \in \mathbb{R}^{F\times F}$ comprising of different feature detecting *kernels* is convolved with this resulting image, the output neurons of this layer contain feature maps and given by Equation (3.22).

$$(\mathbf{X}_P * f)(m,n) = \sum_{c=1}^{3}\sum_{i=1}^{F}\sum_{j=1}^{F}\mathbf{X}(m+i,n+j,c)f(i,j) \tag{3.22}$$

where m =1,2,3 ... $(\frac{W+2P-F}{S})+1$ and n =1,2,3 ... $(\frac{H+2P-F}{S})+1$. Here, S is the stride by which the filter has been shifted across the image.

Besides, two different types of activation functions Linear Unit (ReLU) and Dropout Unit (DU), have been used in extraction layers and output layer repeatedly.

3.3.1.6 Classification

The classification layers of the proposed CNN are shown in the second part of Figure 3.15. Here, the operations are:
- Feed forward propagation
- Softmax activation
- Optimization using Back propagation

3.3.1.6.1 Feed Forward Propagation: The input feature vector has been added with bias after being multiplied with the random weights and the activation function has been applied on the resulting matrix two times in FC 7 and FC 8 layers.

$$\mathbf{Y} = \varphi^{(8)}\left(\mathbf{W}^{(8)}\varphi^{(7)}\left(\mathbf{W}^{(7)}\mathbf{X}^{(6)} + \mathbf{b}^{(7)}\right) + \mathbf{b}^{(8)}\right) \tag{3.23}$$

Here, $\mathbf{Y} = [y_1\ y_2 \ldots\ y_j \ldots y_{13}]^T$ is classifier output vector. The bracketed index given at the top of the quantity indicates the layer number, where the quantities are:
φ : activation function; $\mathbf{W}$: weight matrix; $\mathbf{b}$: bias vector; $\mathbf{X}$: input feature vector.

3.3.1.6.2 Softmax function activation: The softmax function as shown in Equation (3.24) has been applied on thirteen output numeric values to obtain normalized probability distribution where larger value

becomes more larger and smaller becomes more smaller.

$$p_i = \sigma(y_i) = \frac{e^{y_i}}{\sum_{j=1}^{13} e^{y_j}} \tag{3.24}$$

$\forall \quad i$ from 1 to 13 and obviously $\sum p_i = 1$.

3.3.1.6.3 Optimization using Back Propagation: The cross entropy has been considered as loss function given in Equation (3.25). Back propagation technique has been used to get optimal values weights ($\mathbf{W}$) and bias ($\mathbf{b}$) by reducing the loss function in an iterative process.

$$\mathcal{L}(\mathbf{W}, \mathbf{b}) = \sum_{j=1}^{13} p_j^* \log\left(\frac{1}{p_j}\right) \tag{3.25}$$

where $\mathcal{L}$ is loss function. The classifier output probability vector and probability distribution of label vector are $p = [p_1\ p_2 \dots p_j \dots p_{13}]^T$ and $p^* = [p_1^*\ p_2^* \dots p_j^* \dots p_{13}^*]^T$ respectively. $\mathbf{W}$ and $\mathbf{b}$ are weight and bias tensors respectively. The stochastic gradient descent method (SGDM) and chain rule of derivatives have been used to update the weights and bias at the end of each iteration.

3.3.2 Results and Discussions

This article aims at categorizing different types of power system disturbances. This necessitates PSD creation, big data generation and training a classifier. The results at every step are given in a sequential manner in the following sections.

From 1210 mother signals of all classes, 3510 informative child signals (ICS) were stored after the data clustering of 16 child signals for each event. In the Figure 3.17, seven informative child signals with higher

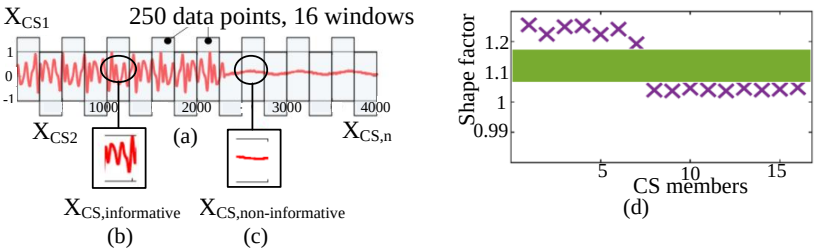

Figure 3.17: Unsupervised k-mean binary clustering of CD1 event (a) 16-child signals (b) informative child signals (c) non-informative child signals (d) clustered seven informative child signals

shape factors have been segregated using k-mean clustering method for capacitance switching event.

Figure 3.18 shows the population of mother signals and filtered informative child signals for all disturbance classes. The number of MS for CD1, CD10, CD11 and CD12 have not been more than 50 because of thermal and electrical rating constraints of the generator winding. For CD2 the population of ICS is just 8 more than MS. Here 200 has been taken as 1 per unit. After rounding up, 200 ICS from each class as shown by a black horizontal line, have been chosen for further processing. 41 mother signals of capacitance switching (CD1) have generated 340 child signals as shown in Figure 3.19 and corresponding RGB images are also shown.

2600 scalogram images have been obtained from 2600 ICS. All CWT image outputs of 2600×1 and their *Red* (R), *Green* (G) and *Blue* (B) component images of 2600×3 have been stored in the form of tensor. Figure 3.20 shows CWT image outputs of 13 ICS, one from each class. Data sizes at different stages of operations are summarised in Table 3.15.

During mini-batch training, it has been observed that the loss function has decreased as the epoch goes on increasing. Simultaneously, the

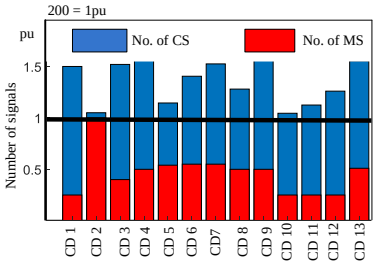

Figure 3.18: Population comparison among mother and child signals

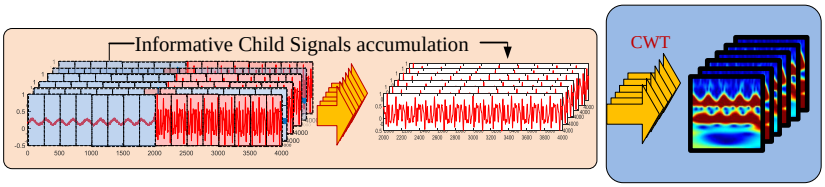

Figure 3.19: Big data generation and image creation

Table 3.15: Parameter value at different stages

Parameters	Values	Parameters	Values
Input class	13	Input of FC6	4096
Current signals	13 × 200=2600	Dropout	50%
Training set	80%	Classification layer FC8	13
CWT image	227× 227× 3	Output classifier	softmax

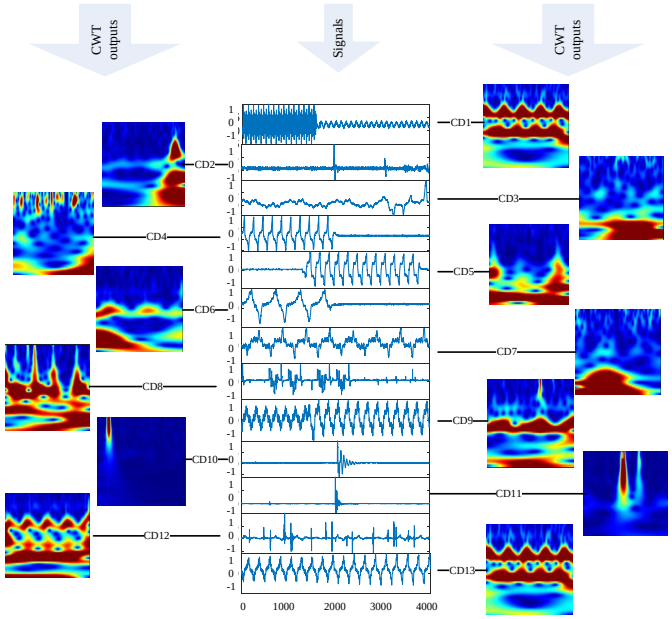

Figure 3.20: 13 CWT image outputs for 13 different classes

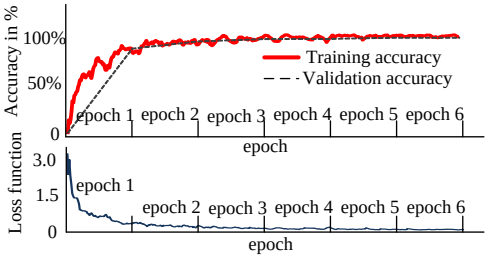

Figure 3.21: Accuracy and loss function variation with epoch

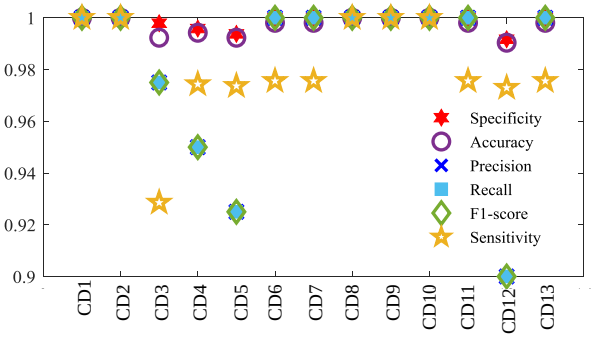

Figure 3.22: Class-wise variation of performance indices

validation accuracy level has been increased with epoch as shown in Figure 3.21 by *black* line and 98.46% accuracy has been achieved at the end of the final epoch.

The class-wise performance indices like accuracy, precision, recall, F1-score, sensitivity and specificity are represented in Figure 3.22. It is clear that out of 13 classes, 9 classes have been predicted with 100% accuracy though, in the case of CD3, CD4, CD6 and CD12, very few events have been misclassified.

In Table 3.16 this proposed customized CNN has been compared with other power system disturbance classification methods used in [15] and

Table 3.16: Comparison with other methods used in different works

Reference work	Used methods	Disturbance signal creation	Accuracy in %
[15]	Gabor filter guided softmax	Simulated	97.00
[23]	ST guided CNN	Programmable ac source	98.25
Proposed method	**CWT guided customized CNN**	**Practical low voltage power system**	**98.46**

[23].

The performance of the classifier under different noisy conditions has also been observed in Table 3.17. Signals with different noise contamination levels specified by signal-to-noise ratio (SNR) have been compared. The accuracy level is acceptable even at higher noise contamination of 20 dB.

Table 3.17: Performance of Classifier under Noisy Environment

SNR	Accuracy(%)	RCT(pu)
20 dB	97.5	1.02
30 dB	98.46	1.02
40 dB	97.94	1.05
50 dB	98.45	1.05
60 dB	98.46	1.05
without noise	98.46	1.00

3.3.3 Limitation of this Method

Though the proposed method performed the classification task satisfactorily, there are some limitations with respect of the types of events.

Firstly, the synchronisation of DG with the power grid and its islanding are very common phenomena which have not been addressed in this section. Besides, in this section, three-phase faults have been considered only for the no-load conditions. But, in actual practice, this fault may occur at any circuit conditions. These two facts have been considered in the preceding section.

3.4 Classification of Single PSD using Mathematical Morphology Based PCA Aided SVM

In this part, the methodology of Mathematical Morphology (MM) based Power System Disturbances (PSD) sensing using Principal Component Analysis aided Support Vector Machine (SVM) has been introduced. The statistical features are extracted from the acquired data using Mathematical Morphology (MM). The high dimensional correlated feature variables are transformed into a smaller set of uncorrelated variables called principal components using Principal Component Analysis (PCA). Finally, a Support Vector Machine (SVM) based Machine Learning (ML) algorithm has been proposed using a quadratic polynomial kernel function to classify the disturbances and the performance of the algorithm has also been assessed. The results show that the performance of the proposed method is acceptable for sensing PSD. The present method is generic in nature and can be implemented for similar problems.

In the recent past, various algorithms like multiple cycle wave shape-based analysis[14], deep convolution method with classifier[15], multi-resolution decision tree-based approach [16] etc. have been reported. In [14] authors proposed a detection method based on wave shapes during

the disturbance. In [15], Poras *et al* numerically simulated fifteen different disturbances, used the Gabor filter to reduce noise and achieved 97% accuracy. Nine different types of disturbances along with distributed sources have been simulated in [17] and variational mode decomposition (VMD) based classification has been made. Ramesh *et al* in [18], used Hilbert transform (HT) before the classifier has been modelled. In [19], a random forest (RF) based classifier has been used after the power signal has been converted to a grey image. In [20] authors focused on determining the location of different disturbances using wavelet transform of the sensed signals. Nand *et al* in [21] worked on a real-time grid-connected network and proposed an empirical mode decomposition technique for detection and classification. In [22] and [23], authors proposed a hybrid model for feature extraction and classification and 98.86% accuracy has been achieved. In [24] authors simulated high impedance fault (HIF) using MATLAB and developed a power spectral analysis-based algorithm for the detection of faulty feeders. In [25], wavelet transforms (WT) have been applied to the signals after the inception of fault to extract coefficients before the fuzzy-based classifier has been modelled.

In this study, the high impedance faults (HIF) have also been taken into consideration as these are likely to occur in DG-based systems. The conventional protection scheme may fail to detect due to the similarity of the HIF current with the normal current magnitude. The classification is also challenging due to the similar nature of HIF current with that of SLG fault.

In this work, fifteen completely different events comprising all possible short circuit faults, switching, load change, islanding as well as prime mover faults have been considered.

The distorted signals of current and voltage have been sensed and tracked using the data acquisition arrangement (DAA). The raw signal contains noise in the form of high-frequency transients, errors caused by non-linearity in the response of sensors, and unpredictable behaviour of

the power system. Hence the detection of the actual shape of the disturbance waveform should be identified initially to detect every disturbance accurately. This task has been performed by mathematical morphology (MM) based filtering technique. The sensed noisy signals are processed by the structuring element function which creeps as a moving window but not interact with the signals [13]. The wanted and unwanted features can be preserved or suppressed respectively by the fundamental morphological operator. The MM-based technique has been used successfully to eliminate the dc offset of a current transformer to improve the performance of protective devices in [97]. Besides, the researchers in [98], [99] and [100] have applied this technique successfully in their own fields. The literature cited in [101] signifies the efficacy of MM-based feature extraction in the field of power system fault analysis. In this study, MM performs dual operation – filtration and feature extraction. Since the significant features can also be extracted during MM operation, no further or extra transformation tool is required to implement this work. It also saves the detection time. The ten morphological operations of dilation and erosion followed by their combination have been performed on each DAA sensed signal to obtain the accurate shape attributes and significant statistical features are extracted from these attributes.

For classification purposes support vector machine (SVM) based machine learning algorithm has been proposed in this research. The input feature vector plays an important role to train this classifier with accuracy and fastness. To improve the performances, principal component analysis (PCA) based dimensionality reduction technique has been adopted. Principal components (PCs) are so arranged that most of the variations present in all the original variables remain in the first few PCs [84], [102] and [78]. PCA-based techniques have also been proposed for data mining [80],[79] and [103].

Here, different classes and patterns have been sensed during fifteen different disturbances using DAA. To recognize and classify a large num-

ber of datasets obtained from DAA, an SVM-based algorithm has been designed to find the best boundaries. It models nonlinear decision boundaries by nonlinear kernel function [104]. SVM-based algorithm for classification has been proposed in [105] and [106].

Therefore, an efficient methodology has been developed for sensing PSD with reasonable accuracy. These disturbances are generated with the help of real DG-based power system networks. First, MM-based filtering has been applied to the sensor output signal for the extraction of shape attributes because of its suitability with the noisy real dataset. Then, PCA based SVM classifier has been designed. The detailed steps of the proposed algorithm for feature extraction, selection and classification will be discussed in the following stages.

3.4.1 Methodology of Single Power System Disturbances Events Identification

3.4.1.1 Disturbance Creation

Fifteen different types of disturbances as listed in Table 3.19 have been generated in accordance with the following IEC 60909-0:2016 standards [76], using the experimental setup shown in Figure 2.1 of Chapter 2, Section 2.1.1.1. The different loading conditions in both the isolated and grid-connected operating modes have been performed using the switching operation and load variation arrangement. The switching has been done using a 12 V battery-operated 25 A solid state relay (SSR) (UNI 901 ZDA). The three-phase switches S1 and S2 are used for motor starting and to connect or disconnect the resistive and inductive type load. The mechanical load of the induction motor has been varied by using the belt pulley arrangement. A series combination of a 100 Ω rheostat and an coil has been used as RL load. The load impedance and the power factor have been varied with the help of the rheostat. The

Table 3.18: Components Used in Hardware Setup

Components	**Range / Ratings**
Alternator	3 Ph, 50 Hz, 1500 rpm, 230 V, 1 kW
Exciter	I/P : 230 V, 50 Hz O/P : 220V dc
DC Motor	3 Ph, 220 V, 1500 rpm, 3 hp
DC Power Supply	I/P: 230 V, 1 ph, 50 Hz O/P: i) 220 V dc Excitation to the motor field ii) 220 V dc armature supply
Main Bus	50 Hz, 3 ph, Line Voltage = 415 V, Phase Voltage = 230 V
Grid	415 V, 50 Hz
Induction Motor (Local load)	3 Ph, 50 Hz, 1425 rpm, 415 V, 3 hp

switching of a capacitor bank has been done by S3.

Among these PSDs from C1 to C15, High Impedance Fault (HIF) (C2) is the most difficult to generate. It required an additional setup as shown in Figure 2.3 of Section 2.1.2 of Chapter 2. Figure 2.4 of Section 2.1.2 of Chapter 2 shows a few materials like soil, stones, sand, twig, and dry and wet leaves, commonly associated with this type of fault. In our study, two critical cases have been considered. In class C3, the sudden disconnection of DG from the grid affects the power quality of the system. This islanding is mandatory when grid instability occurs. In C9, mechanical energy input to the generator shaft gets interrupted due to sudden malfunctioning of steam or fuel valves, breaking of shaft or bearing, rotor eccentricity etc. resulting in oscillation of machine angle about post operating point.

Table 3.19: Classes of Power System Disturbances (PSD)

Class	PSD
C1	Capacitance Switching
C2	High Impedance Fault
C3	Islanding
C4	Line to Line Fault
C5	Line-Line to Ground Fault
C6	Three Phase Fault at no load
C7	Three Phase Fault with R load
C8	Three Phase Fault with RL load
C9	Mechanical Power Interruption
C10	Nonlinear Load Injection
C11	Reactor Switching
C12	Single Line to Ground (SLG) Fault with Isolated Neutral
C13	SLG Fault with Neutral Grounded
C14	Single Phasing
C15	Sudden Load Change

3.4.1.2 Feature Extraction Technique Based on Mathematical Morphology

The current signals of few events are so similar in nature that their statistical features are not sufficient to classify them. Besides, the signals contain noise and some undefined random error signals. For the purpose of filtration and to obtain large number of features, Mathematical Morphology (MM) has been applied on each signal of raw data set ($\mathbf{X}$). Some operations of Mathematical Morphology with "*line*" structuring element ($\mathbf{B}$) have been performed to extract its shape and size attributes in terms of its statistical indices. Two basic operations – *dilation* and *erosion* – one followed by the other and depending on the operation sequence, they are termed *opening* and *closing* operations. The basic theory of MM is detailed in [13]. Here, a few basic morphological operations and their combinations are given in the equations from Equations (3.26) to (3.31).

Dilation (D) and Erosion (E):

$$M_1 = D = X \oplus B \quad ; \qquad M_2 = E = X \ominus B \tag{3.26}$$

Opening (O) and Closing (C):

$$M_3 = O = E \oplus B \quad ; \qquad M_4 = C = D \ominus B \tag{3.27}$$

Dilation erosion difference filter (DEDF) and Opening closing difference filter (OCDF):

$$M_5 = DEDF = D - E \quad ; \qquad M_6 = OCDF = O - C \tag{3.28}$$

Morphological median filter (MMF) and Open close median (OCM):

$$M_7 = MMF1 = \frac{D+E}{2} \; ; \qquad M_8 = OCM1 = \frac{O+C}{2} \tag{3.29}$$

Similarly,

$$M_9 = MMF2 = \frac{(MMF1 \oplus B) + (MMF1 \ominus B)}{2} \tag{3.30}$$

$$M_{10} = OCM2 = \frac{(OCM1 \oplus B) + (OCM1 \ominus B)}{2} \tag{3.31}$$

For each of the 1200 datasets, the above ten operations ($\boldsymbol{M_1, M_2, M_3, \ldots\ldots\ldots\ldots M_{10}}$) are performed. Four statistical features– *Maximum Value, Variance, Skewness and Kurtosis* are extracted from each MM output. The variance of i^{th} data set ($\boldsymbol{M_i}$) is represented as $\mathrm{Var}(M_i) = \sigma_i^2$ where σ_i is the *standard deviation* and

$$\sigma_i = \sqrt{\frac{1}{m}\sum_{j=1}^{n}\left(M_{i,j} - \overline{M_i}\right)} \tag{3.32}$$

Here, m is the number of data points in each vector $\boldsymbol{M}_i$, $M_{i,j}$ is j$^{\text{th}}$ element of $\boldsymbol{M_i}$ and $\overline{M_\mathbf{i}}$ is the mean value. The *skewness*

$$S_i\left(M_i\right) = \frac{\sqrt{m(m-1)}}{m-2} \times \frac{\frac{1}{m}\sum_{j=1}^{m}\left(M_{i,j} - \overline{M_i}\right)^3}{\sigma^2} \tag{3.33}$$

And the *kurtosis*,

$$K_i\left(M_i\right) = \frac{\frac{1}{m}\sum_{j=1}^{m}\left(M_{i,j} - \overline{M_i}\right)^4}{\sigma^4} \tag{3.34}$$

The extracted distinct features are processed further using the PCA technique, and a new set of features having significant variances are considered in designing the classifier. The dimension of data stored after MM operation is 1200×40.

3.4.1.3 Dimensionality Reduction using Principal Component Analysis (PCA)

For the problem considered here, MM features are highly correlated causing difficulties in classification. This issue is handled effectively by PCA technique. It helps to transfer those correlated features into equal number of uncorrelated PCs. As lower number of PCs retains all variability of the original features, the dimensionality of the problem reduces. Besides, the transformation technique is very simple as the PCs are the linear combination of all features. It also allows us to visualize and interpret the problem in 2D or 3D. PCA has been used to reduce the dimensionality of the data set having many interrelated variables [84],[102]. The scattered normalized data of p variables are transformed into a new set of uncorrelated and linear combinations of original variables. The first few variables retain most of the variation present in all of the original variables. The feature vector $\mathbf{X}$ obtained from MM is fed to the PCA algorithm to select the most significant

principal components before SVM-based machine learning is performed. The detailed theory has been given in [78]. First step is to investigate a linear function (PC_1) of the elements of $\mathbf{X}$ having maximum variance i.e. $PC_1 = \mathbf{a_1}^{'}\mathbf{X} = a_{11}x_1 + \ldots + a_{1i}x_i + \ldots\ldots\ldots\ldots + a_{1p}x_p = \sum_{j=1}^{p} a_{\mathrm{ij}}x_j$ To maximize PC_1, it requires to maximize $\mathbf{a_1}^{'}\mathbf{\Sigma}\ \mathbf{a}_1$ subject to $\mathbf{a_1}^{'}\mathbf{a_1}$=1. Where Σ is the covariance of the original variables *(x_1, x_2, ... x_i ..... x_p)* and it is given as

$$\Sigma = \begin{bmatrix} \mathrm{var}\,(x_1) & \mathrm{cov}\,(x_1, x_2) & \cdots & \mathrm{cov}\,(x_1, x_p) \\ \vdots & \mathrm{var}\,(x_2) & & \vdots \\ \mathrm{cov}\,(x_p, x_1) & \cdots & & \mathrm{var}\,(x_p) \end{bmatrix} \tag{3.35}$$

$$\mathrm{var}\,(x_i) = \frac{\sum_{k=1}^{n}(x_{i,k} - \overline{x_i})^2}{n-1} \tag{3.36}$$

$$\mathrm{cov}\,(x_i, x_j) = \frac{\sum_{k=1}^{n}(x_{i,k} - \overline{x_i})(x_{j,k} - \overline{x_j})}{n-1} \tag{3.37}$$

for i and $j = 1, 2 \ldots\ldots\ldots p$ but $i \neq j$ Introducing *Lagrange multiplier* to include the equality constraint, *Lagrange* function has been formed as

$$L = \mathbf{a_1}^{'}\mathbf{\Sigma}\ \mathbf{a}_1 - \lambda(\mathbf{a_1}^{'}\mathbf{a_1} - 1) \tag{3.38}$$

Now, differentiating with respect to a_1 one gets

$$(\mathbf{\Sigma} - \lambda\mathbf{I_p})\,\mathbf{a_1} = 0 \tag{3.39}$$

$\mathbf{I_p}$ is *($p \times p$)* identity matrix and λ is eigenvalue of Σ and $\mathbf{a_1}$ is the corresponding eigenvector. The principal components (PC) are arranged according to their variances. Only PCs with significant variances are considered for classification.

3.4.1.4 Classifier Design using SVM-based Machine Learning

As a supervised learning algorithm, SVM has been used with the goal of segregating 14-dimensional space into said classes. SVM algorithm helps to create the best decision boundary known as *hyperplane*, with sufficient margin among the support vectors belonging to different classes. As fifteen different types of disturbances are taken here, a multiclass classification technique has been adopted. It is an extended application of *one versus one* (OVO) binary classification technique as shown in Figure 3.23. Each class is segregated from all other classes separately, generating ${}^{15}C_2$ number of classifiers. The detailed theory and derivations are given in [107] and [108] where the classifier $(\mathbf{W_{ij}}, \mathbf{b_{ij}})$ of linearly separable vectors of two classes is obtained by maximizing the derived *Lagrangian function*, $L(\alpha)$ given in Equation (3.40) and solving *Lagrange* Multipliers, α.

$$L(\alpha) = \sum_{i=1}^{N} \alpha_i - \frac{1}{2} \sum_{i=1}^{N} \sum_{j=1}^{N} \alpha_i \alpha_j \; y_i y_j \; \mathbf{X}_i \mathbf{X}_j \tag{3.40}$$

here, $y_i = \pm 1$ and $\boldsymbol{X}_i$ is i^{th} vector.

For a non-separable problem, to make it separable, *Lagrange function* is modified as Equation (3.41) introducing non-linear kernel functions $k\left(\boldsymbol{X}_i, \boldsymbol{X}_j\right)$, which replaces the inner products $(\boldsymbol{X}_i \boldsymbol{X}_j)$

$$L(\alpha) = \sum_{i=1}^{N} \alpha_i - \frac{1}{2} \sum_{i=1}^{N} \sum_{j=1}^{N} \alpha_i \alpha_j \; y_i y_j \mathrm{k} \; (\mathbf{X}_i \mathbf{X}_j) \tag{3.41}$$

Subject to $\alpha_i \geq 0$ and $\sum_{i=1}^{N} \alpha_i y_i = 0$. The ten-fold cross-validation technique has been used to modify the classifier and to reduce misclassification errors as obtained by using Equation (3.42). In this mode of operation, 10% events have been used for validation and the rest 90%

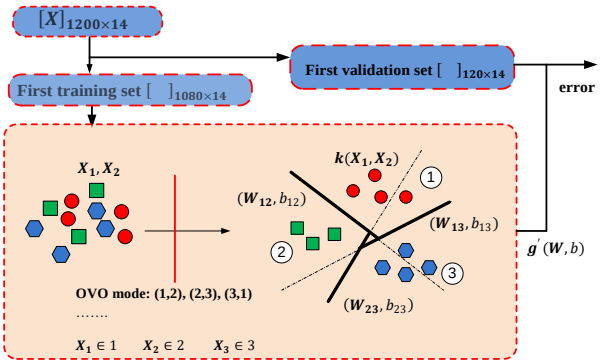

Figure 3.23: Flowchart of OVO based cross-validation

events have been used to train the classifier as shown in Figure 3.23.

$$E_{val(avg)} = \frac{1}{10}\sum_{i=1}^{10} E_{val}(g^{'}(i)) \tag{3.42}$$

where, $E_{val}(g^{'}(i))$ and $E_{val(avg)}$ are the error in i^{th} cross-validation and the average error at the end of the validation process, respectively. The algorithm of the whole process is given in Table 3.20.

3.4.2 Results and discussion

A total of 1200 data files, 80 data files for each class have been used to train the classifier. The results are produced below in a sequential manner.

Step 1: The current waveforms for the different PSD events were recorded using data acquisition system. The Figure 3.24 represents the recorded current and voltage signal of a PSD event (i.e. C7).

Among all 1200 raw signals acquired from 1200 events, only one signal from each class has been shown in Figure 3.25. The following character-

Table 3.20: Algorithm for Complete Workflow

Input: PSD data
Output: Type of disturbance
Feature extraction from raw data
1. Load n current signals of (1×4000) data set each.
2. **for *i=1 to n***
3. Carry on MM operations: D, E, O,C, DEDF, OCDF, MMF1, MMF2, OCM1 and OCM2.
4. ***End for loop***
5. Compute statistical features of MM output data sets: $Maximum\ value$, $Variance$, $Skewness$ and $Kurtosis$.
Principal Components selection using PCA
6. All features stored in n *by* p matrix.
7. Compute covariance matrix
8. Get eigenvalues and eigenvectors.
9. Compute all PCs.
10. Construct a *scree plot*.
11. Select a suitable number of PCs.
Training of SVM based Classifier.
12. Construct Training database.
13. Divide data into q subsets for cross-validation.
14. ***For i=1:q*** For all test subsets and training sets.
15. Use polynomial kernel functions. Obtain optimal $Hyperplane$.
16. ***End for loop.***
17. Get SVM classifier.
18. Evaluate performance.

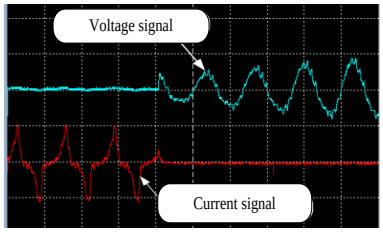

Figure 3.24: Recorded line voltage and line current for the event C7

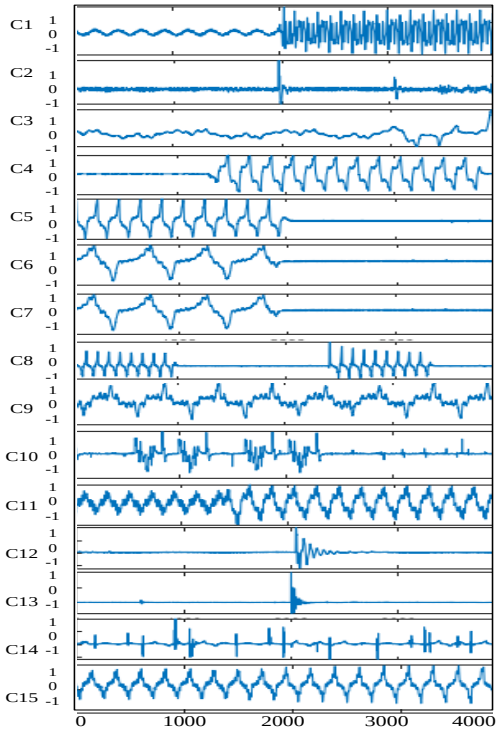

Figure 3.25: Recorded current signals of different Power System Disturbance events

istics are noticed from visual observation of the signals.

- Each current waveform clearly indicates the point where the disturbance occurs.
- The waveforms belonging to C2, C5 and C13 classes of disturbance, primarily associated with ground contain high-frequency transients. The number of transients and their durations differ from each other.
- The signals from C4, C5, C13 and C14 are of the same nature and the current flows in two phase-conductors.
- C1 and C11 are switching events, the raw signals are symmetrical with high frequency transient at the time of inception of the switching.
- C6, C7 and C8 are of same nature. The waveforms are symmetrical with some DC offsets at the instant when the fault occurs.
- C3, C9 and C15 are similar in nature and occur when there is any power mismatch between the input and output of the DG. Frequency and amplitude variation with time are observed.
- The waveform in C10 is due to non-linear load switching. It may be symmetrical or unsymmetrical depending on the mode of operation of the semiconductor switching devices. It appears to be non-sinusoidal with lots of harmonics.

Step 2: The ten said morphological operations have been applied on all 1200 datasets, followed by four statistical operations and as an output 1200×40 extracted feature matrix is formed. This matrix is shown in its truncated form in Table 3.21 due to its large actual size.

Step 3: The extracted 1200 data sets are fed to the PCA algorithm to reduce the dimensionality of the feature vector. As an output of PCA, 40 eigenvalues, corresponding 40 eigenvectors are obtained. The resulting PCA loading matrix in its truncated form is shown in Table 3.22, where it is evident that PC28 has maximum variance and contains larger proportions of all 40 input features. PC28 is followed by PC29, PC30, PC32 then PC24 and so on. The *scree* plot is obtained to select the number of PCs to take part in the machine learning algorithm. Here, the variance

Table 3.21: 1200×40 Mathematical morphology Feature Matrix

	m1	m2	....	m25	m26	....	m40
e1	0.36	1.00	....	4.74	7.37	....	-1.095
e2	0.21	0.94	....	6.05	7.25	....	-1.109
....	....	....	....	....	....	....	....
e400	0.29	0.95	....	7.52	7.66	....	-1.074
e401	0.42	0.93	....	7.17	6.88	....	-1.083
.....	.....	.....	.....	.....	.....	.....	.....
e1000	0.29	0.95	....	7.52	7.66	....	-1.074
....	....	....	....	....	....	....	....
e1199	0.93	1.00	....	5.34	4.51	....	-1.064
e1200	0.03	1.00	....	5.23	4.58	....	-1.060

1200×40

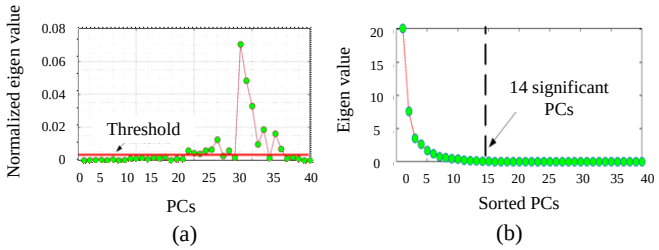

Figure 3.26: Scree plot.(a) Normalized variances of PCs (b) value wise sorted variances of PCs

of all 40 PCs have been represented in two different ways. In Figure 3.26 (a), normalized values of eigen for all PCs are plotted serially and in Figure 3.26 (b) the PCs are sorted according to their eigen values, known as *scree* plot. It is evident from the *scree* plot that the first 14 PCs contain 99.07 % of total variance and the fourteenth onwards PCs are of negligible variances and it has also been validated by the bar chart attached with the Table 3.22.

Step 4: With the 14 PCs as shown in Table 3.22, one-versus-one (OVO) mode of operation and ten-fold validation scheme, a quadratic kernel function-based SVM has been trained. To get the optimal value of the regularization parameter ($\hat{C}$) on which the performance depends, the grid search algorithm has been used as an optimizer and after 100 iterations with 1.76 pu evaluation time, the value of $\hat{C}$ appears to be 2.1544. The performance is shown by the confusion matrix given in Fig-

Table 3.22: PCA Loading Matrix

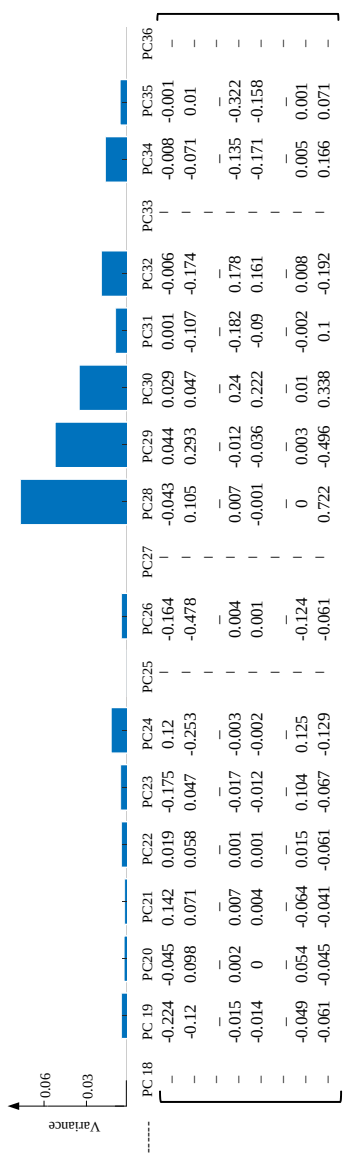

ure 3.27, where it is clear that only 0.67% events have been misclassified. It has also been observed that without PCA, taking all 40 extracted features, 96% accuracy has been obtained with the training time of 1.06 pu whereas using the first 14 PCs with the same machine learning algorithm, 99.3% accuracy has been obtained in just 1 pu time. For 15 PCs, the accuracy remains same whereas computational time increases to 1.20 pu. If all 40 PCs are taken into consideration, accuracy decreases to 98.7% with much more computation time. The Optimum number of PCs is 14. For comparison, accuracy for lower (5 and 10 PCs) and upper (15, 16, 35 and 40 PCs) than the optimum number of PCs are shown in Table 3.24.

Step 5: The event-wise receiver operating characteristics (ROC) with the Area Under Curve (AUC) have been obtained. The ROCs of the events C2 and C3 have been shown in Figure 3.28(a) and Figure 3.28(b), respectively. These curves clearly indicates the detection ability of the classifier to identify C2 and C3 types of disturbances with AUCs of 0.9952 and 0.9965, respectively.
Step 6: Finally, the proposed method has been compared with other two efficient classifiers – Medium Gaussian SVM and Naive Bayes classifier and the comparative results have been shown in the Table 3.23. The accuracies for the first two classifiers are 98% and 94.7% and corresponding Relative Computational Times (RCTs) are 1.03 and 1.24 respectively. RCT is the ratio between the computation time for a particular technique and the minimum computation time considering all techniques [17]. In Table 3.25, the proposed method has also been compared with recently published works on PSD in respect of the number and types of events, feature extraction processes, classification methods and accuracy levels. It is observed that our proposed method is superior than others in the view point of accuracy level except [17]. In [17], the accuracy is slightly higher but only nine events have been considered and also the data have

Table 3.23: Comparison of the Proposed Classifier with the Other Classifiers

Method	Accuracy (%)	RCT
Medium Gaussian SVM	98	1.03
Naive Bayes	94.7	1.24
Proposed Quadratic SVM	99.3	1.00

Table 3.24: Performance Variation with Different Feature Selection

Feature	Accuracy (%)	RCT
40 MM without PCA	96.0	1.06
First 5 PCs	86.0	0.98
First 10 PCs	96.3	0.90
First 14 PCs*	**99.3**	**1.00**
First 15 PCs	99.3	1.20
First 16 PCs	97.3	1.04
First 35 PCs	99.3	2.01
All 40 PCs	98.7	2.15

*The proposed method is taken as a reference

been generated from computer simulation.

3.4.3 Conclusions

In this chapter, the most commonly occurring power system disturbances due to individual root causes have been identified. Starting with only six root causes and increasing the number by adding more single disturbances in succession, a few simple and robust machine learning and deep learning algorithms were proposed for disturbance detection. A summary of all classifiers considered in this chapter has been provided below.

- Six disturbances: After the feature extraction using DWT, KNN-based Machine Learning have been applied and an optimistic result with 97.1% accuracy was achieved.

Table 3.25: Comparison with Other Methods

Reference Papers	**Number of Events**	**Feature Extraction method**	**Classifier**	**Data Generation from**	**Classification Accuracy (%)**
[15]	15	Gabor Filter	Softmax	Simulation	97.00
[16]	16	Multiresolution Stockwell Transform	Decision Tree	Numerical	99.08
[17]	9	Variational mode decomposition	Statistical base	Simulation	99.38
[23]	8 events and their combinations	Stockwell Transform	Convolutional Neural Network	Programmable ac power supply	98.25
Proposed method	15 exclusively different events	MM	PCA based SVM	Practical Experimental setup	99.30

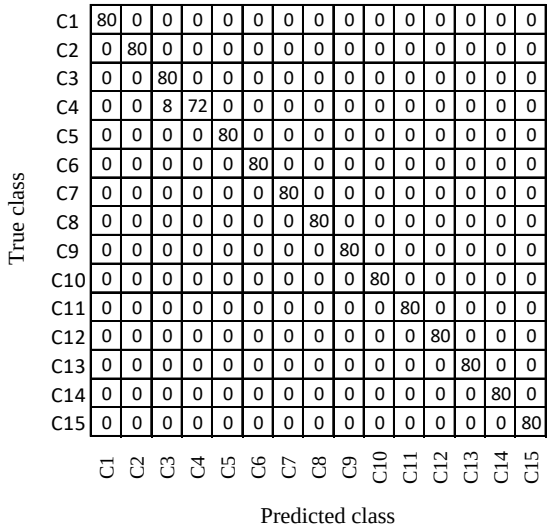

Figure 3.27: Confusion matrix of proposed classifier on all events

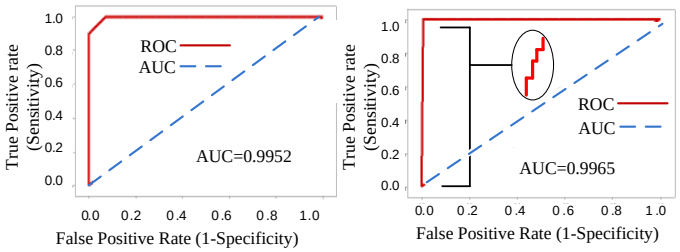

Figure 3.28: ROC and AUC for power system disturbance event (a) C2 and (b) C3

- Eleven disturbances: DFA characteristics were considered as features followed by dimensionality reduction using PCA. A very robust ML, 1-NN gave 97.18% accuracy.
- Thirteen distinct disturbances: CNN-based classifier with tuned hyperparameters provides 98.46% accuracy.
- Fifteen distinct disturbances: For feature extraction and dimensionality reduction, mathematical morphology (MM) and PCA have been used. Finally, quadratic kernel function-based SVM were modelled with 99.3% accuracy.

CHAPTER 4

Classification/Identification of Multiple Power System Disturbances

4.1 Introduction

Fast and accurate detection of power system disturbance-creating events is very much essential for the safe and reliable operation of today's power distribution network. This task becomes more challenging when two events occur simultaneously. Here, a few normal events like switching, load changing, all feasible faults, and five dual events have been considered. In this chapter, three deep learning network-based classifiers have been proposed to classify the events. The methodologies and their implementations have been presented in three sections according to the increasing number of considered events.

4.2 Classification of Multiple PSD Events using CNN-Aided Tailored BiLSTM Model

All acquired disturbance signals are allowed to go through three major stages. At the initial stage, signal-to-image conversion takes place

using continuous wavelet transform (CWT) followed by a couple of convolution operations for feature extraction, and then, the extracted time series data have been fed to the input of Bidirectional Long Short Term Memory (BiLSTM) module. Finally, the softmax output classifier has been applied. Few other popular classifiers have also been studied for comparison. Using this proposed method, 98.57% accuracy has been achieved considering twenty-one feasible events.

The microgrid-based distribution network is one of the major solution to power shortage and uncertainty in the modern power industry due to the numerous advantages of having distributed generators (DGs) as the main source of energy, in terms of environmental issues, reliability, loss reduction factor and node voltage profile [62]. The inclusion of microgrids in power distribution networks offers sustainable development by utilizing renewable energy [109], [12]. In such a DG-based distribution network, due to some normal power system operations along with some conventional faults, sudden changes in node voltages and line currents are likely to occur and create power system disturbances (PSD). This PSD causes the malfunction of electrical appliances and equipment resulting in the interruption of quality power supply to the consumers. To mitigate these problems, power system protection requires fast detection of the causes and their accurate classification for suitable measures. These tasks become challenging because of the diversity in generation technology and the increased complexity of power electronics device interfaced generation unit [109], [27]. In this context, several researches are going on to identify the different types of power system disturbances [110]-[112]. In [110], authors have reported the deep learning method for the identification of islanding, fault, and other power quality disturbances. The authors in [111] have proposed the deep convolutional neural network to classify the power quality disturbances. The articles [64] and [28] ensure the effectiveness of deep learning techniques to address fault detection and fault type classification. In addition to the afore-

mentioned disturbance types, the high impedance fault (HIF) has been considered an important disturbance event and given priority in [112]. The switching transient detection (i.e. capacitor and reactor switching, linear and nonlinear load switching) has been addressed in [109], [113]. It is to be mentioned here that, the PSD classification is an important task for reliable and continuous power supply. In this scenario, several researches are going on multiple PSD classifications where the methodology has been developed based on software-generated synthetic signals [111]-[113]. However, the entire methodology (i.e. training, testing) of the PSD classification based on practical signals is a challenging task for the researchers. In this context, an attempt has been made to develop a suitable methodology for sensing the different PSD events based on real-life test signals.

In the process of classification, a few significant features are required to develop the classifier model. There are several methods for extracting useful features, convolution neural network (CNN) is one of the popular ones because of its auto-feature extraction capability [114]-[116]. It is to be mentioned here that, CNN works on images that are generated by converting the recorded signal using continuous wavelet transform (CWT) [114]. In addition, CNN is considered a powerful tool for feature extraction because of the facility of batch normalization in each convolution layer as in [115]. In [116], authors have reported CNN based technique for the classification of different faults. Besides that, CNN-based deep learning methods have been utilized in the field of biomedical signal processing, hand sign recognition and human movement classification etc. [117]-[119]. In [23], the CNN-based deep learning method has been reported in the area of power quality study. In the same area, the researchers reported the CNN method integrated with the BiLSTM network. In addition, it shows that the CNN can provide automated features and can generate the time series data which provides the advantageous result with BiLSTM network [115], [120]-[122]. Apart from

that, a feed-forward neural network is useful for pattern recognition as stated in [123]. All the feed-forward neural networks, i.e. CNN, RNN, and PNN have been studied and analyzed in [120].

In this work, a CNN-BiLSTM network has been proposed to identify different PSD events. For this purpose, 21 different PSD events have been created separately and disturbance signals have been sensed using a data acquisition system (DAS). It is to be mentioned here that, five dual events are included in those 21 PSD events, which have not been studied before. At first, the convolution neural network (CNN) algorithm has been applied to the real-life signals of the PSD events for significant feature extraction. Thereafter, a new BiLSTM-based RNN has been proposed to identify and classify all possible PSD events that happen in microgrids including dual events. The computational complexity due to the combined effect of convolution, sequencing modelling and neural network (NN) hidden layers, necessitates huge memory, long training time and minute hyperparameter tuning. Finally, the performance of the proposed scheme has been validated class-wise by computing the confusion matrix.

4.2.1 Methodology of Multiple Power System Disturbance Events Identification

The operations at different stages are given in the preceding sections.

4.2.1.1 Data Acquisition

For the generation, sensing and recording of signals, a test setup comprising of a generator-prime mover set, signal sensing & data acquisition system, and disturbance-producing arrangement, have been prepared as shown in Figure 2.1 of Chapter 2, Section 2.1.1.1.

Using this experimental setup, twenty-one different classes of disturbances under three major categories have been created using Solid State

Table 4.1: Category-wise twenty one events

Classes	Major categories		
	Switching and load changing events	Dual Events	Faults
C1: Capacitance switching	√		
C2: On load islanding with generation equal to load	√		
C3: On load islanding with generation greater than load	√		
C4: High impedance fault			√
C5: Induction motor (IM) starting	√		
C6: Islanding followed by EV charging		√	
C7: Islanding followed by load shading		√	
C8: Islanding followed by IM starting		√	
C9: Islanding followed by open circuit		√	
C10: Islanding followed by single phasing		√	
C11: Islanding at off load	√		
C12: Double line fault			√
C13: Double line to ground			√
C14: Three phase fault			√
C15: Mechanical power interruption			√
C16: Non- linear load switching	√		
C17: Reactance switching	√		
C18: Single line to ground fault with isolated neutral			√
C19: Single line to ground fault with grounded neutral			√
C20: Single phasing			√
C21: Sudden load change	√		

Relay (SSR) and grid synchronizing Switches (GSS).
Category 1: Eight switching and load changing events
Category 2: Five dual events
Category 3: Eight line faults

All classes are mentioned in Table 4.1 clearly. 200 cases for each class have been considered and a total of 4200 signals have been processed further.

4.2.1.2 Pre-processing of Recorded Signal Data

The Normalization and the filtration operations were performed on each signal before they were converted to CNN-compatible three-channel images using continuous wavelet transform (CWT).

Initially, the frequency content across the whole time span of each signal $x(t)$ has been represented by a wavelet function $W_x(\alpha, \beta)$ in the form of the scalogram using Equation (4.1), where $\hat{\psi}(t)$ is the dual function of $\psi(t)$. α and β are scale and shifting factors respectively.

$$W_x(\alpha, \beta) = \frac{1}{\sqrt{\alpha}} \int_{-\infty}^{\infty} x(t) \hat{\psi} \left(\frac{t - \beta}{\alpha} \right) dt \tag{4.1}$$

The admissible constant C_ψ as given by Equation (4.2) lies between zero and infinity.

$$C_\psi = \int_{-\infty}^{\infty} \frac{\bar{\hat{\psi}}(\tau) \hat{\hat{\psi}}(\tau)}{|\tau|} d\tau \tag{4.2}$$

4.2.1.3 CNN based Feature Extraction

For multi-class classification, distinct features of individual categories are highly recommended for better performance of the classifier. Red-green-blue (RGB) three-channel image provides the frequency information of a signal for the full range of time. Convolution Neural Network (CNN) has been used to extract deep and distinct features from the images as much as possible. After convolution with a suitable number of kernel filters, resulting neurons carry all possible distinct features. Each neuron helps in detecting a particular characteristic for a particular class of events.

All 227× 227 pixels three-channel images have been fed to the input layer of CNN for feature extraction after all the pixel values are normalized. Here, CNN has been made of three sets of four layers – convolution,

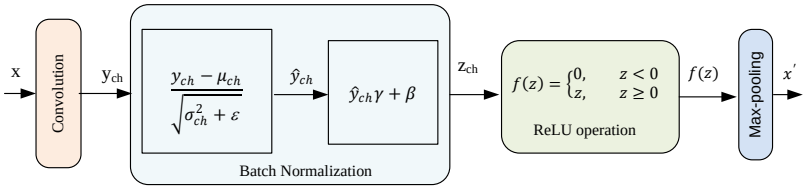

Figure 4.1: One set of feature extraction layers

batch normalization, ReLU operation, and max pooling as shown Figure 4.1.

4.2.1.4 Convolution using Kernel Filter

Each channel image was convoluted with a kernel filter. When the B-channel image matrix, $\mathbf{X_B}$ of $W \times H$ is convoluted with kernel $\mathbf{k}$ of $L \times M$ with horizontal stride and vertical stride of S_1 and S_2 respectively, it gives an output of size $W_{out} \times H_{out}$.
Where,

$$W_{out} = \frac{W - L}{S_1} + 1 \tag{4.3}$$

$$H_{out} = \frac{H - M}{S_2} + 1 \tag{4.4}$$

The numerical values of the output matrix are obtained from Equation (4.5) for all the horizontal positions, from one to W_{out}, and vertical positions, from one to H_{out}. The graphical representation of this convolution operation is shown in Figure 4.2.

$$\mathbf{X_B} * \mathbf{k} = \sum_{l=1,m=1}^{L,M} \sum_{i=S_1,j=S_2}^{S_1+L,S_2+M} X_B(i,j).k(l,m) \tag{4.5}$$

$\forall \in 1, 2, ... W_{out}$ and $\forall \in 1, 2, ...H_{out}$.
Here, $X_B(i,j)$ is the pixel value of B-channel image at i^{th} row and j^{th}

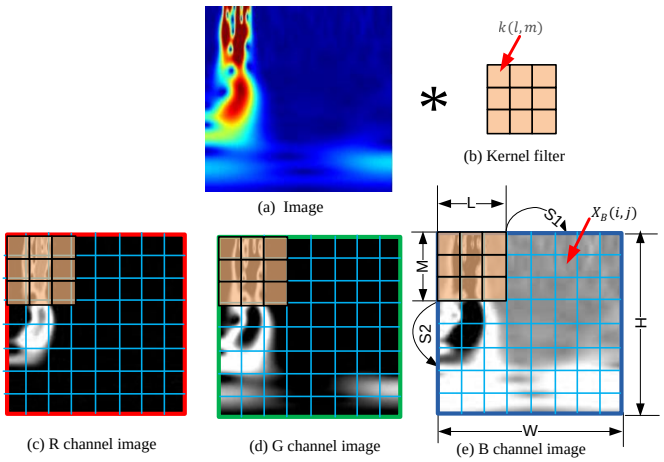

Figure 4.2: Three channel convolution operation with kernel filter column; and $k(l,m)$ is the kernel value at l^{th} row and m^{th} column. Likewise, other channels are convoluted with the same kernels.

4.2.1.5 Batch Normalization

After the completion of the convolution for all training examples in a batch of size N_B, the feature maps of all neurons belonging to the same channel have been normalized to minimize the co-variate shift making the mean value zero and standard deviation to be one. A particular channel contains similar feature neurons belonging to the training examples in a batch as shown in Figure 4.3.

It results in causing the distribution of the features belonging to the same class to be more or less the same. In the first step of batch normalization, the element values of the feature vector are scaled to the values ranging from zero to one using Equation (4.6).

$$\hat{y}_{ch} = \frac{y_{ch} - \mu_{ch}}{\sqrt{\sigma_{ch}^2 + \epsilon}} \tag{4.6}$$

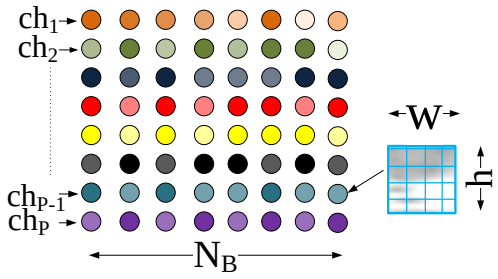

Figure 4.3: Schematic diagram of channel-wise neurons for any layer of all training samples in a batch

where, μ_{ch} stands for mean value, σ^2_{ch} is the variance of the neurons of any channel and ϵ of very insignificant value has been added to avoid any undefined term in case of any zero variance. The mean and the variance are given by the following equations

$$\mu_{ch} = \frac{1}{N_B \times w \times h} \sum_{n=1}^{N_B} \sum_{i=1}^{w} \sum_{j=1}^{h} (x_{ch})_{n,i,j} \tag{4.7}$$

and

$$\sigma^2_{ch} = \frac{1}{N_B \times w \times h} \sum_{n=1}^{N_B} \sum_{i=1}^{w} \sum_{j=1}^{h} \Big((x_{ch})_{n,i,j} - \mu_{ch} \Big) \tag{4.8}$$

$\forall\ ch \in ch_1, ch_2, ...ch_P$

Here, the size of each neuron is $w \times h$, and the total number of channels or the total number of neurons per example is P. n is sample index in a batch, i and j are width and height indices of neuron, respectively.

Finally, the weights γ and the bias β are introduced as per Equation (4.9) to get normalized output, z_{ch}.

$$z_{ch} = \hat{y}_{ch}\gamma + \beta \tag{4.9}$$

4.2.1.6 Rectified Linear Unit operation

Rectified linear unit (ReLU) is a very commonly used activation function for any deep learning network to avoid any vanishing gradient problem and to optimize hyper-parameters at a faster rate. The resulting neurons of ReLU are obtained as per the definition given in Equation (4.10)

$$f(x) = \begin{cases} 0 & \text{if } x \leq 0 \\ x & \text{if } x > 0 \end{cases} \tag{4.10}$$

4.2.1.7 Maximum Pooling Operation

The pooling operation is performed after every convolution to reduce the dimension of the feature map without losing feature characteristics. The dimension of resulting feature map when $f \times f$ kernel moves across the feature map $(H_c \times W_c)$ with s stride as shown in Figure 4.4 is $\frac{(H_c - f + 1)}{s} \times \frac{(W_c - f + 1)}{s} \times 3$

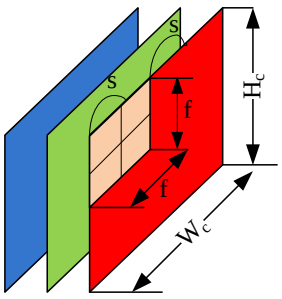

Figure 4.4: Max pooling operation on RGB image

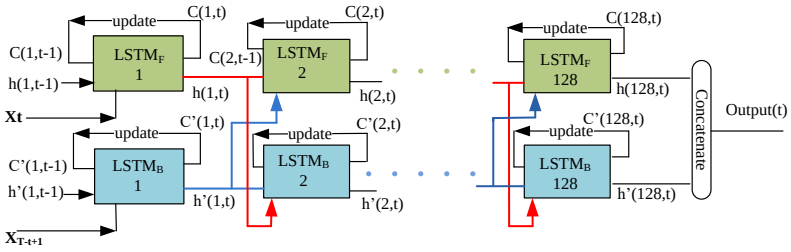

Figure 4.5: Time series data processing in BiLSTM

4.2.1.8 Time-Series Data Preparation

It is necessary to prepare the data that are compatible with the input layer of the classifier. Here, all feature maps are transformed into a single 1D vector to make this suitable for the input layer of Bidirectional Long Short Term Memory (BiLSTM) which requires time-series data (TSD).

4.2.1.9 Classification by BiLSTM

Unlike conventional classifiers, feature maps are not directly fed to the Recurrent Neural Network (RNN). The feature maps are flattened to produce a single-column vector or sequence. As a result, N_B training samples from different classes provide N_B number of sequential data, which have been fed sequentially to our proposed BiLSTM-based RNN. Unlike simple LSTM-based RNN, in BiLSTM, N_B sequential data are also fed in a reverse way to a different set of LSTM. The number of time series data, T is exactly equal to the number of samples per batch, N_B. Here, a total of 128 layers of forward and backward LSTM ($LSTM_F$ and $LSTM_B$) sets have been considered. As shown in Figure 4.5, at any instant of time (t) of training process, two inputs– one X_t being fed to forward LSTM and other X_{T-t+1} fed to backward LSTM– have been processed to obtain short term (ST) information (h and h') and long term memories (LTM) or cell state (C and C') which have resulted in modifying learnable parameters and thus reaching convergence at faster

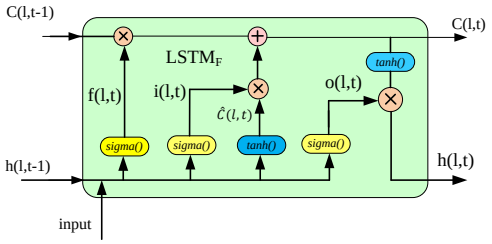

Figure 4.6: An LSTM architecture in l^{th} layer at t^{th} time

rate.

Here, in Figure 4.6, a single LSTM module comprising of all input and output cell states $(C(l,t), C'(l,t))$ and hidden state$(h(l,t), h'(l,t))$ along with the intermediate quantities in l^{th} layer at t^{th} time has been shown. In this module, ST and LTM are formed using the outputs of three gates- forget, input, and output gates. The output of output gate $f(l,t)$ has been obtained taking sigmoid (σ) of weighted $W_f(l,t)$ sequence resulting from recent memory $(h(l,t-1))$ and current input $(input(l,t))$ with bias terms $(b_f(l,t))$ as given in Equation (4.11). Cell state $C(l,t)$ is influenced by input gate and forget gate output as given in Equation (4.12). Hidden state $h(l,t)$ is influenced by input, output, and updated cell state as given in Equations (4.13), (4.14), (4.15) and (4.16). The expression for cell state and hidden state for backward LSTM in l^{th} layer and at t^{th} time are given in the similar manner. All quantities would be replaced by the same nomenclature with a "$'$" symbol. i.e f by f', C by C' and so on.

The full BiLSTM architecture is given in Figure 4.7. For the first layer, at time t, the variable, $input_1$ to the forward LSTM is X_t and that $(input_2)$ for backward LSTM is X_{T-t+1}. In all the layers, other than the first layer, forward LSTM input $(input_1)$ is the hidden state $h'(l-1,t)$ of backward LSTM in the previous layer and input to the $LSTM_B$ $(input_2)$ is the hidden state $h(l-1,t)$ of the $LSTM_B$ in the

previous layer.

$$f(l,t) = \sigma\left(W_f(l,t).[h(l,t-1), input(l,t)] + b_f(l,t)\right) \tag{4.11}$$

$$C(l,t) = f(l,t) * C(l,t-1) + i(l,t) * \tilde{C}(l,t) \tag{4.12}$$

$$i(l,t) = \sigma\left(W_i(l,t).[h(l,t-1), input(l,t)] + b_i(l,t)\right) \tag{4.13}$$

$$\tilde{C}(l,t) = \tanh\left(W_c(l,t)[h(l,t-1), input(l,t)] + b_c(l,t)\right) \tag{4.14}$$

$$o(l,t) = \sigma\left(W_o(l,t)[h(l,t-1), input(l,t)] + b_o(l,t)\right) \tag{4.15}$$

$$h(l,t) = o(l,t) * \tanh(C(l,t)) \tag{4.16}$$

The algorithm of the proposed BiLSTM applied to T number of time series sequential data is given in Table 4.2. T sequential outputs are fed to the fully connected (FC) layer of 21 neurons. $Softmax$ activation applied on FC gives probabilities of output classes.

4.2.2 Results and Discussion

As mentioned in Chapter 2, Section 2.1.1.1, 21 different types of disturbances, 200 events of each type, have been generated. A total of 4200 currents have been sensed and recorded for the detection of the type of disturbances. Every component and their sizes and numbers at every stage starting from data acquisition to the final prediction are indicated in Table 4.3. The results in all stages have been presented sequentially.

Table 4.2: BiLSTM Algorithm

Input: T or N_B number of time series data $(X(1), X(2), ...X(T))$
Output: $output(t) \quad \forall \quad t$
$Initialize : C(l,0), h(l,0).C^{'}(l,0), h^{'}(l,0)$ for all $layers$
Do for $t = 1 : T$
$input_1$=$X(t)$; $input_2$=$X(T-t+1)$
Do for $l = 1 : 128$
Determine $C(l,t)$, $h(l,t)$, $C'(l,t)$ and $h'(l,t)$
$[C(l,t) \quad h(l,t)]$ =function$(C(l,t-1), h(l,t-1), input_1)$
$[C'(l,t) \quad h'(l,t)]$ =function$(C'(l,t-1), h'(l,t-1), input_2)$
(using Equations from (4.11) to (4.16))
$input_1$=$h'(l,t)$
$input_2$=$h(l,t)$
end
$output(t)$=$concatenate(input_1, input_2)$
end

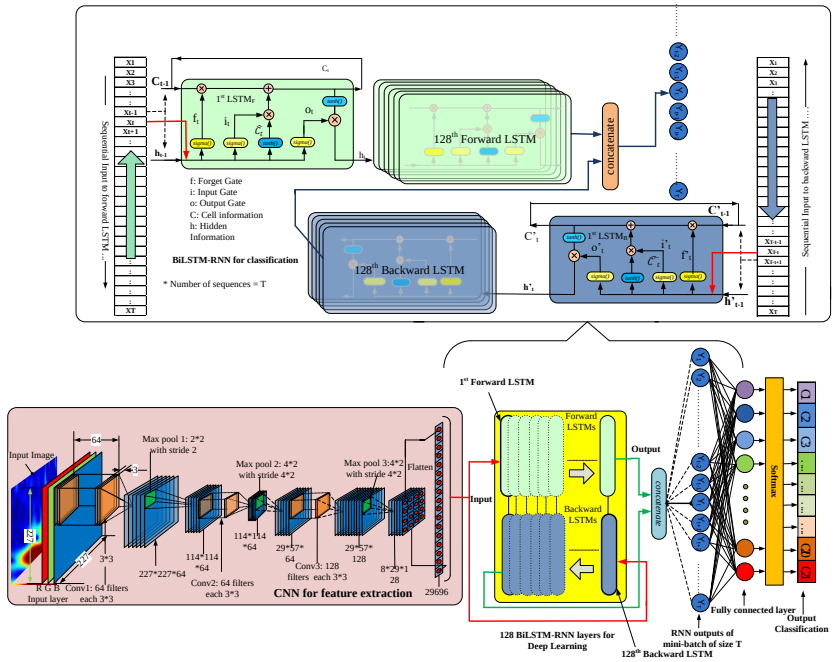

Figure 4.7: Proposed customized Convolution-BiLSTM based Deep Neural Network architecture

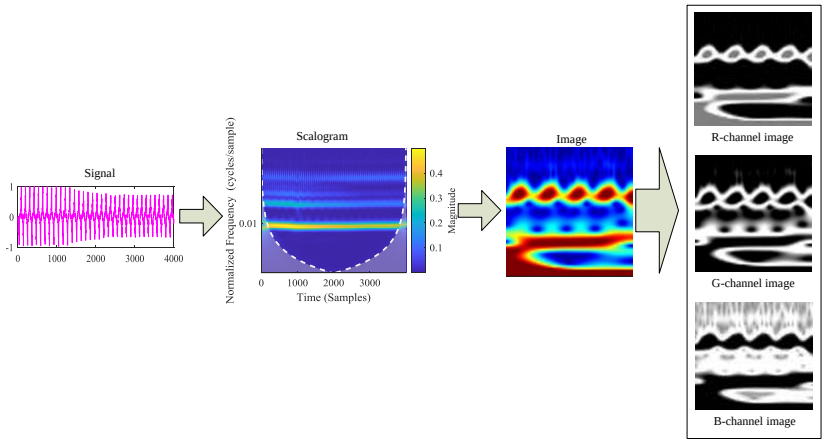

Figure 4.8: Signal to RGB three channel image formation

4.2.2.1 Data Acquisition and Processing Stage

At the initial stage, 4200 three-channel images of size 4200 three-channel images of 227×227 pixels were generated using CWT, as presented in Table 4.3.

Here, in Figure 4.8, the step-by-step signal to RGB image formation has been shown for a single case of sudden load change category (i.e. C21). The current signal clearly indicates the sample points after 1000 decreased due to the decrease in load demand. The frequency contents throughout the sample window have been shown in the Scalogram. Its image, and respective red, green and blue components have also been shown in Figure 4.8.

Additionally, one image from each of the switching, dual event, fault, and load change groups is shown in Figure 4.9.

4.2.2.2 Feature Extraction Stage

In this stage, all 227× 227 pixels three-channel images have been fed to the input layer of CNN for feature extraction after all the pixel values

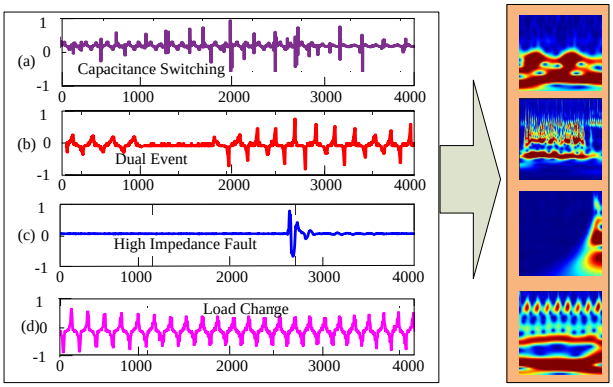

Figure 4.9: CWT Image output of four signals for (a) capacitance switching (b) islanding followed by EV charging (c) high impedance fault (d) sudden load change

are normalized. The convolution operation with 3×3 kernel on three images obtained from an event of islanding with generation equal to load is shown in Figure 4.2. In the first stage of convolution, a total of 64 *kernel* filters at 2×2 pixel stride rate produce 113×113 feature maps using Equations (4.3), (4.4) and (4.5).

After three convolution operations followed by the last max pooling operation, 128 feature neurons of 8×29 have been generated. Sequential data of 29696 size for feeding to the BiLSTM classification layer has been prepared using $faltten$ operation.

4.2.2.3 Classification Stage

A total of 33 neurons from 33 examples of each batch have been generated after BiLSTM operation. These 33 outputs converge to 21 neurons at the fully connected layer after they are multiplied by weights and added with bias. The $softmax$ activation applied on these neurons gives the probability value. The class having a higher probability value will be the predicted class. The variation of the accuracy and loss func-

Table 4.3: Stage-wise parameters and their values

Stages	Paprameters	Value/Size
Data Acquisition and Processing	Classes	21
	Current Signals	21×200=4200
	CWT output Images	227×227×3
Feature Extraction	Input Image Layer	227×227×3
	1st Convolution Layer	Filter Size 3×3 , Number=64, Stride 2×2
	1st Max Pooling Layer	kernel size 2×2 , Stride 2×2, Output : 114×114×64
	2nd Convolution Layer	Filter Size 3×3 , Number=64, Stride 1×1
	2nd Max Pooling Layer	kernel size 4×2 , Stride 4×2, Output: 29×57×64
	3rd Convolution Layer	Filter Size 3×3 , Number=128, Stride 1×1
	3rd Max Pooling Layer	kernel size 4×2 , Stride 4×2, Output: 8×29×128
	Flatten Layer	Sequential Output size: 29696
Classification	BiLSTM	Hidden Layers: 128 , Output Mode :Last, State Activation Function: tanh, Gate Activation Function: sigmoid
	Fully Connected Layer	21
	Output Classifier	softmax
	Loss Function	Cross Entropy
Training Parameter	Optimizer	sdgm
	Batch Size	33
	Epoch	6
	Learning Rate	0.008

tion with iteration count has been shown in Figure 4.10. At the end of all 6 epochs and 600 iterations, an overall accuracy of 98.57% has been achieved and the objective loss function is seen to be approaching zero.

4.2.2.4 Performance Evaluation

Here, a few popular performance indices have been calculated from the class-wise true positive (TP), true negative (TN), false positive (FP), and false negative (FN) values. Initially, these values are obtained using equations Equations (4.17) to (4.20) from the confusion matrices presented in Figure 4.11. In these matrices, j indicates the prediction class index, i stands for the actual class index, and $C_{i,j}$ is the value at i^{th} row and j^{th} column. The calculated values of TP, TN, FP and FN have been given in Table 4.4. Besides a few indices like *accuracy, precision, F1-score, sensitivity and specificity* derived from TP, TN, FP and FN, using formulae given from (4.21) to (4.25) have also been calculated. Figure 4.12 depicts each Machine Learning performance indices for all 21 classes. The accuracy and specificity are nearly 100%. The precision level of class $C3$ is 90%, the lowest among all.

4.2.2.5 Comparison with Benchmark Methods

This proposed CNN-based feature extraction and BiLSTM-based prediction method has been compared with other popular deep learning methods as shown in Table4.5. The feature has been extracted in two different ways i.e. CNN and Alexnet. The proposed BiLSTM prediction model has been compared with benchmark machine learning (ML) and deep learning (DL) techniques. The accuracy level of the proposed method is 1% to 1.5% higher as compared with the CNN-based LSTM, CNN-based quadratic SVM, AlexNet and AlexNet-based narrow neural network (NNN).

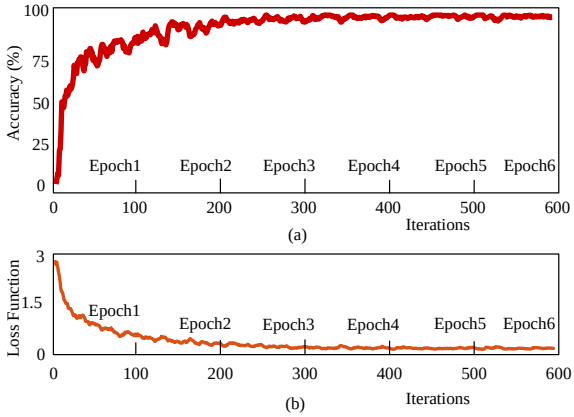

Figure 4.10: (a) Accuracy and (b) loss curve of proposed method

$$TP_k = C_{k,k} \tag{4.17}$$

$$FN_k = \sum_{i=1(i\neq k)}^{N} \sum_{j=1(i\neq k)}^{N} C_{i,j} \tag{4.18}$$

$$TN_k = \sum_{i=1,i\neq k}^{N} C_{i,k} \tag{4.19}$$

$$FP_k = \sum_{j=1,j\neq k}^{N} C_{k,j} \tag{4.20}$$

$$Accuracy_k = \frac{TP_k + TN_k}{TP_k + TN_k + FP_k + FN_k} \tag{4.21}$$

$$Precision_k = \frac{TP_k}{TP_k + FP_k} \tag{4.22}$$

$$F1 - Score_k = 2 \times \frac{Precision_k \times Recall_k}{Precision_k + Recall_k} \tag{4.23}$$

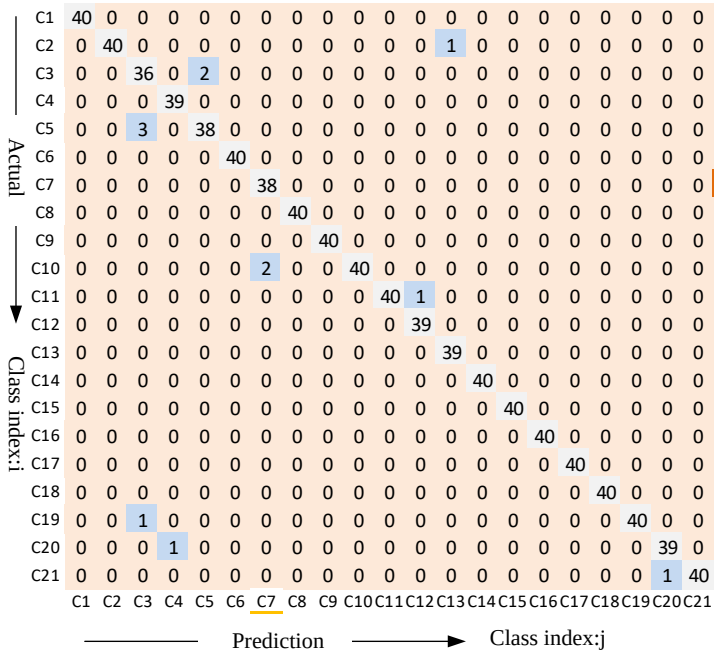

Figure 4.11: Confusion matrix for evaluation of class-wise performance

Table 4.4: Class wise performance indices

Class	TP	TN	FP	FN
C1	40	800	0	0
C2	40	799	0	1
C3	36	798	4	2
C4	39	800	1	0
C5	38	797	2	3
C6	40	800	0	0
C7	38	800	2	0
C8	40	800	0	0
C9	40	800	0	0
C10	40	798	0	2

Class	TP	TN	FP	FN
C11	40	799	0	1
C12	39	800	1	0
C13	39	800	1	0
C14	40	800	0	0
C15	40	800	0	0
C16	40	800	0	0
C17	40	800	0	0
C18	40	800	0	0
C19	40	799	0	1
C20	39	799	1	1
C21	40	799	0	1

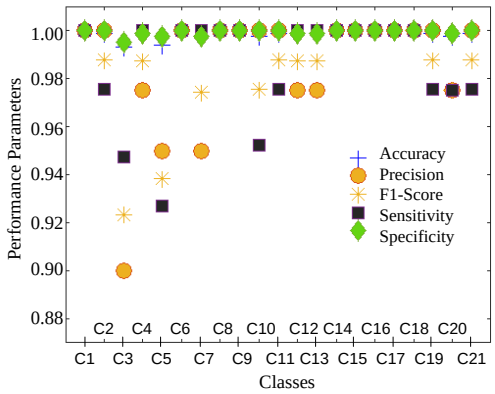

Figure 4.12: Class wise performance indices

$$Sensitivity_k = \frac{TP_k}{TP_k + FN_k} \tag{4.24}$$

$$Specificity_k = \frac{TN_k}{TN_k + FP_k} \tag{4.25}$$

4.2.2.6 Performance in Noisy Environment

The performance of the proposed method has also been evaluated in a noisy environment. The noise level has been varied from 60 dB signal-to-noise ratio (SNR) to 20 dB SNR, and the corresponding accuracy level and their relative computational time (RCT) have been observed and presented in Table4.6. It has been observed that each 10dB SNR decrement causes around 1% accuracy fall without any significant change in RCT. Here, RCT value in the case of no noise is taken as unity i.e. 1 pu. At the highest noise level of 20 dB SNR, the accuracy still appears to be more than 90%.

The accuracy under different training to test ratios and noise levels up to 40 dB has also been determined to obtain the overall accuracy to

Table 4.5: Comparison with other methods

Extraction Method	Prediction Model	Acc. (%)	Extraction Method	Prediction Model	Acc. (%)
CNN	LSTM	97.14	Alexnet 6th FC output	Naïve Bayes	79.8
CNN	KNN	96.3	Alexnet 6th FC output	Subspace KNN Ensemble	96.9
CNN	SVM (Linear)	95.5	Alexnet 6th FC output	Fine Tree	87.8
CNN	SVM (Quadratic)	97.6	Alexnet 6th FC output	Narrow Neural Network	97.6
Alexnet	Alexnet	97.14	**Proposed CNN**	**BiLSTM**	**98.57**

* FC : Fully Connected Layer

consider the presence of noise in the system. The accuracy at different combinations of training to test ratios and noise levels has been shown in Table 4.7. The average values and respective standard deviations have also been calculated. With 80% training set, the overall accuracy of 97.266% has been achieved with a standard deviation of ± 1.65.

Here, a few other state-of-the-art methods presented in the recent articles in the same field have been investigated and compared with this work as given in Table 4.8. There are very few works where such diverse types of experimentally generated disturbance signals have been considered.

Table 4.6: Performance of the proposed method at different noise levels

SNR	Accuracy (%)	RCT (pu)
without noise	98.57	1.000
60 dB	97.50	1.025
50 dB	95.24	1.175
40 dB	94.64	1.125
30 dB	93.57	1.100
20 dB	92.74	1.075

Table 4.7: Accuracy variation with training to test ratio and noise level variation

Training/ test	Practical signal	Noise level						Avg.	Std. dev.
		90dB	80dB	70dB	60dB	50dB	40dB		
80/20	**98.57**	98.57	98.52	97.82	97.5	95.24	94.64	**97.266**	±1.65
70/30	**98.57**	98.57	97.64	97.23	97.64	95.00	94.31	96.994	±1.68
60/40	97.11	97.02	97.02	97.08	95.18	94.81	92.41	95.804	±1.79
50/50	97.03	97.02	97.01	97.01	95.1	93.00	91.14	95.330	±2.40
–	97.82	97.795	97.548	97.285	96.355	94.51	93.13	**96.349**	±1.84

Table 4.8: Comparison with recent state-of-the-art methods

Ref.	Method used		No. of classes and type	Accuracy (in %)
	Feature extraction	Classification		
[27]	MTCDN	DNN	8, Practical	98.3
[28]	MCEE-MDAN+ CGAN	CNN	10, Practical+ Generated	75 to 99.50
[23]	ST	CNN	37, Synthetic	98.25
[71]	CWT	Customized AlexNet CNN	13, Practical	98.46
This paper	CNN	BiLSTM+NN	21, Practical	**98.57**

4.3 Classification of Multiple PSD Events using Recurrence Plots Based Customised CNN Model

This work proposes a Recurrence Plot (RP) based customized convolution neural network (CNN) method for the power system disturbance classification of (Distributed Generation) DG-based networks. All feasible disturbance-creating events including faults, different switching events and dual disturbances have been considered here. The proposed method has been applied to the disturbance signals generated from a laboratory-based experimental setup of DG. Those signals were converted to RP images to train the CNN algorithm. In addition, recurrence quantification analysis (RQA) was performed to train the Support Vector Machine (SVM) simultaneously for comparison. Performance indices have been estimated to validate the proposed method. This algorithm has also been tested under highly noisy conditions and performs satisfactorily.

The Indian power system paradigm has already been shifted from centralized generation technology to distributed generation (DG) due to several apparent issues stated by the International Energy Agency (IEA) [124]. It is also important to explore renewable energy generation technology to address environmental issues in the modern era. Those renewable energy units can be used as DGs in power distribution networks [125]. However, several new complications arise in a DG-based network in terms of a changed voltage profile, increased short circuit level, power losses, voltage transient, etc., which affect the protection and stability of the power system [11] and [126]. System stability hampers due to the failure of reactive power management, which may occur in the case of DG-based systems since DGs consist of induction generators, which usually can't provide reactive power. Therefore, DG units require a

power electronics interface to compensate for the reactive power, and consequently, power quality degrades [11]. The advancement is also necessary for designing the protection scheme of this type of network to cope with the increased short circuit level and bidirectional current flowing [11],[125]. Frequently, DG operates in islanding mode, which also creates power quality issues. Due to those mentioned issues, the power system disturbance study must be revised so that a DG-based network can send uninterrupted and high-quality electrical power. The very fast detection and classification of all feasible power system disturbances that create such complicated situations, mentioned above, are mandatory for stable DG-based power system operation. This classification study is very difficult when a huge variety of disturbances are considered, including situations of multi-disturbance, i.e., different categories of disturbance happen at the same time [71]. This study is significant to avoid unnecessary interruptions due to the maloperation of protective devices and to make the protection system of the DG network more sensitive to the causes of the disturbances but not the effects of the disturbances. It is possible when the source or cause of disturbances is classified. Classification of different types of faults, islanding and non-islanding transients, switching transient disturbances, and different power quality issues have been studied in several research articles [127]–[133]. However, none of the feasible disturbances were considered in those studies. Most articles consider a lower number of single events for real-time signal classification, and when higher events or multiple events are considered, the signals are generated synthetically. A few authors studied a higher number of real-time signals. However, all the dual disturbances have not been considered in that article either. This classification study considered 24 disturbance events, including 19 single and 5 dual events. The feature extraction process is based on the recurrence plot (RP) method in the proposed method, as in [132]. The RP carries much significant information about the nonstationary signals, and this RP method uses the proper-

ties of a deterministic dynamical system [133] and [134]. All the dynamic characteristics of the system can be determined using this RP-based feature extraction method [134]. Hence, this visualization tool is used for feature extraction in different areas of application, i.e., [133]–[136]. The benefits of using RP-based methods in power quality disturbance analysis studies have been described in [137]. The theory of RP, stated in [138], to visualize the time series data of a complex dynamical system has been applied in this study. A convolutional neural network (CNN)-based classifier has been trained using the RP of different disturbance signals in this study. Recurrence quantification analysis (RQA) has been applied initially to train SVM classifiers. But the results are not satisfactory. A very good result has been obtained when the features are used in image form. Better classification accuracy can be achieved by using this RP to train the CNN compared to the use of continuous wavelet transform-based image formation to train the CNN [71]. The authors in [139] have also shown the efficacy of the combination of the RP-CNN method to identify faults in rolling bearings. This proposed RP-based CNN algorithm for the classification of all feasible power system disturbances in a DG-based network has been validated using real disturbance signals recorded from an experimental setup in a power system laboratory, maintaining all standard specifications. A very satisfactory result has been achieved with 98.91% accuracy. All the results are furnished and analyzed in Section 4.3.2.

4.3.1 Methodology of Multiple Power System Disturbance Events Identification

The methodologies and their implementations are presented in the following sections.

4.3.1.1 Real Time Signal Generation

A test bench has been prepared to create disturbance signals for all 24 events, as shown in Figure 2.1 and Figure 2.2 of Chapter 2, Section 2.1.1.1.

For each event, 200 disturbance signals were created. All 24 events considered here fall into three major groups as categorised in Table 4.9. Here, nine normally occurring power system operations have been considered (**E1** to **E9**). These all create transients in voltage and current waves for three to five cycles. Besides, islanding operations at three different loading conditions (**E7, E8** and **E9**) have also been included in this work, which are common occurrences in the DG-based power system.

Under the second broad category, all usual power faults (**E10** to **E17**). In addition to those faults, the input machine shaft power interruption (**E18**) due to the valve failure, breaking of shaft and shaft eccentricity has been considered here. The high-impedance fault (HIF, **E19**), the detection of which is challenging for power engineers, has also been given priority in this work. All events from **E20** to **E24** in the third category have been created operating two events simultaneously which is another challenging task in this work.

4.3.1.2 Proposed Methodology

After acquiring all the disturbance signals in discrete form, data normalization has been carried out. The composite work plan has been depicted in Figure 4.13. As mentioned in the plan, all normalized data sets have been used to calculate the recurrence plot (RP) matrices. From their three-dimensional RGB images, feature maps were generated using convolution, and finally, the deep neural network-based classifier was trained. In addition, a recurrence quantification-based feature matrix has also been developed to design a machine-learning-based classifier for

Table 4.9: All considered power system events

Broad Categories	Events
E1–E9: Normal events	**E1:** Capacitance switching, **E2:** Reactor switching, **E3:** Non-linear load, **E4:** Sudden load change, **E5:** Electric vehicle (EV) charging, **E6:** Induction motor starting, **E7:** Islanding at no load, **E8:** Islanding with generation equal to local load, **E9:** Islanding with generation greater than local load
E10 – E19: Faults	**E10:** Single line to ground (SLG) fault, **E11:** SLG with neutral grounded, **E12:** Line to line fault (LL), **E13:** LL with ground fault, **E14:** No load three phase (LLL) fault, **E15:** LLL with resistive load, **E16:** LLL with inductive load, **E17:** Single phase loading, **E18:** Input mechanical power failure and **E19:** High impedance fault (HIF)
E20–E24: Dual events	**E20:** Islanding and EV charging, **E21:** Islading and load shedding, **E22:** Islanding and motor starting, **E23:** Islanding and open circuit, and **E24:** Islanding and single phasing

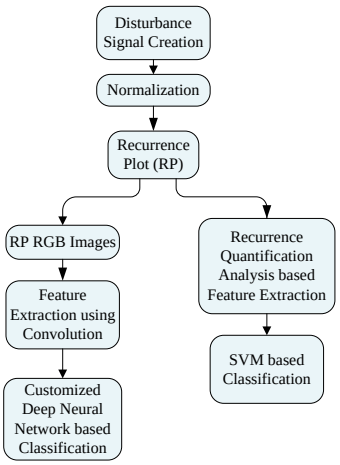

Figure 4.13: The composite block diagram for RP-based classification using CNN

comparison with the proposed CNN model. The major stages, i.e., RP generation, the development of feature maps, and the training of classifiers, have been dealt with in the subsequent sections.

4.3.1.3 Recurrence Plot Generation

Feature extraction is the initial part of any classification problem. Here, a novel technique has been adopted for the better realization of the data sets to ease the extraction process.

The time series data has been visualised in the form of a recurrence plot (RP). For normalized signal data, $X = [X_0\, X_1 \ldots X_i \ldots X_j \ldots X_{N-1}]$, the recurrence behaviour of a state X_i in phase space has been denoted by the element of RP matrix. X_i and X_j are two different states of the time series data X as shown in Figure 4.14. Two arbitrary data points X_i

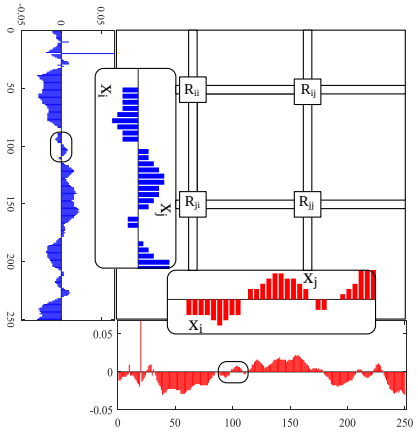

Figure 4.14: Recurrence plot formation

and X_j have been shown in the enlarged views of a very small region of the data set along row and column. The distances between any two data points are calculated using Equation (4.45) to form a recurrence plot.

The easiest way of theoretical understanding is to place the same data set along the row and column and to find all self and mutual distances. Using Equation (4.45), the entries of N×N RP matrix are obtained by applying the Heaviside function on those distances with a constant cut-off (ϵ) known as threshold distance. The element of RP, R_{ij} at i^{th} row and j^{th} column is given by the following equation.

$$R_{ij} = \mathcal{H}\left(\epsilon - ||X_i - X_j||\right) \tag{4.26}$$

where, i and j both are from 0 to $N-1$, ϵ is threshold distance, $||.||$ is Euclidean norm, and $\mathcal{H}$ is Heaviside function.

4.3.1.4 Recurrence Quantification Analysis (RQA)

The RP is characterized by a few indices that clearly indicates the recurrence behavior of a signal. These are as follows.

4.3.1.4.1 Recurrence rate:

$$RR = \frac{1}{N^2}\sum_{i,j=1}^{N} R_{i,j} \tag{4.27}$$

4.3.1.4.2 Determinism:

$$DET = \frac{\sum_{l=l_{min}}^{l_{max}} lp(l)}{\sum_{l=l_0}^{l_{max}} lp(l)} \tag{4.28}$$

Where, $p(l)$: histogram of the length (l) of diagonal lines.

4.3.1.4.3 Ratio:

$$RATIO = \frac{DET}{RR} \tag{4.29}$$

4.3.1.4.4 Average length of the diagonal lines:

$$L = \frac{\sum_{l=l_{min}}^{l_{max}} lp(l)}{\sum_{l=l_{min}}^{l_{max}} p(l)} \tag{4.30}$$

4.3.1.4.5 Entropy:

$$ENTR = -\sum_{l=lmin}^{l_{max}} p(l) \ln p(l) \tag{4.31}$$

4.3.1.4.6 Largest Diagonal Line:

$$l_{max} = max\,(l_i \;\; ; \quad i = 1, 2, \;\; \ldots \;\; N) \tag{4.32}$$

4.3.1.5 Convolution-based Feature Extraction

The pixel values of all 227×227 Red-green-blue (RGB) three-channel recurrence plots are normalized before they are fed to a convolution neural network (CNN) to construct distinct feature maps. Each channel image has been convoluted with suitable kernel filters [124]. When a $W \times H$ image is convolved with $w \times h$ *kernel* filter, the resulting feature map gets the dimensions given by Equations (4.3) and (4.4) of Section 4.2.1.4.

4.3.1.6 Customized Deep Neural Network-based Classification

The extracted feature maps are allowed to pass through the deep neural network as modelled in [124]. This NN model comprises one flattened and two dense layers followed by a softmax output classifier. The layer-wise operation and resulting output shapes have been given in the result section.

4.3.2 Results and Discussion

As described in Section 4.3.1.2, from data generation to their final classification, the outputs in each stage have been discussed sequentially in this section.

4.3.2.1 Disturbance signals

After the normalisation, one disturbance signal from each of the 24 events has been depicted in Figure 4.15. In this figure, signals for three broad categories have been shown separately. It is clear from the signals that a few signals such as E2, E10, and E19 are very close to each other. Besides, E22, E24, E11 and E5 have very slight differences and E3, E4, E14, E15, E17 and E18 are similar with very insignificant differences.

4.3.2.2 Recurrence Plots

Though a set of signals is similar as mentioned in the earlier section, their recurrence plots are a little bit different. The recurrence plots (RPs) of all the previously mentioned signals have been presented in Figure 4.16.

4.3.2.3 Recurrence Quantification Analysis

The histogram of the RP diagonal lines has been used to obtain the quantification indices. In Figure 4.17, the histogram of RP for a disturbance due to sudden load change is shown. A truncated version of the recurrence quantification feature matrix has been shown in Table 4.10. This feature matrix has been considered for the classification using the Support Vector Machine for comparison.

To distinguish the 24 typical events based on RP indices, all six RP indices are shown in Figure 4.18. It is observed from the figure that the dual events have the longest diagonal line compared to other events.

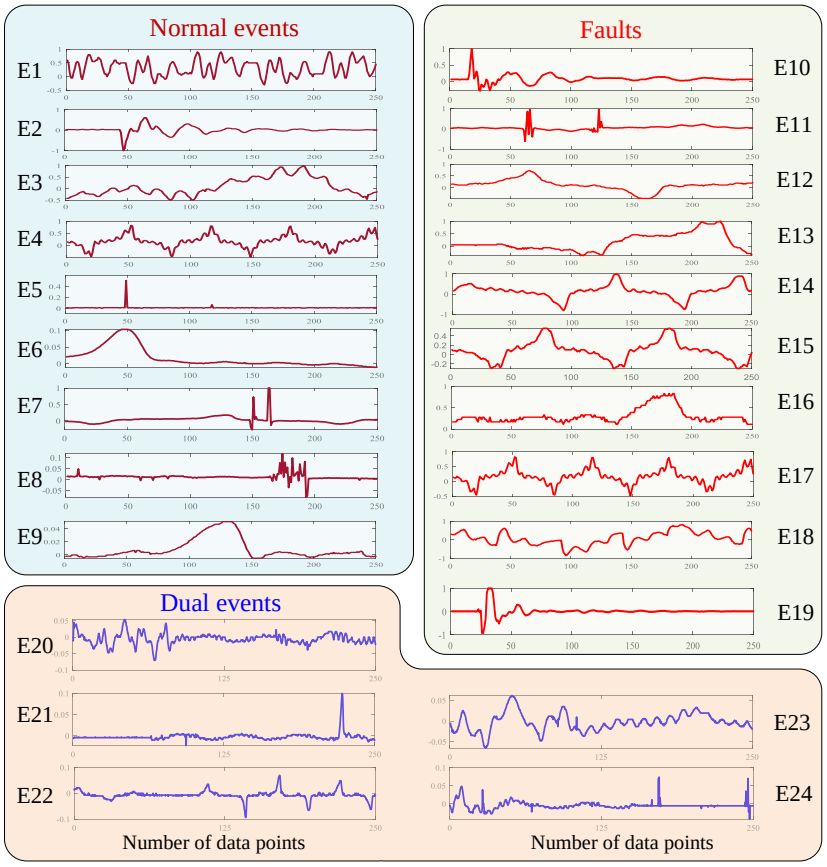

Figure 4.15: Recorded 24 disturbance signals one from each event

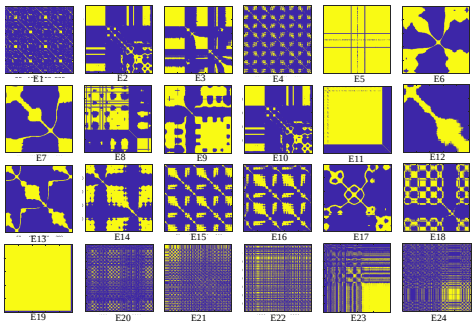

Figure 4.16: Recurrence plots (RP) for all 24 events

Table 4.10: 4800×6 recurrence quantification (RQ) feature matrix

Disturbances	Q1	Q2	Q3	Q4	Q5	Q6	Event Type
D1	0.020955	0.604184	0.082154	0.178164	0.625718	0.000909	E1
D2	0.020316	0.623164	0.111284	0.152712	0.665648	0.00084	E1
D3	0.024784	0.686835	0.134737	0.089831	0.601412	0.000851	E1
D4799	0.223028	0.958634	0.48478	0.13082	0.093278	0.416273	E24
D4800	0.196048	0.947381	0.451602	0.107773	0.10487	0.464971	E24

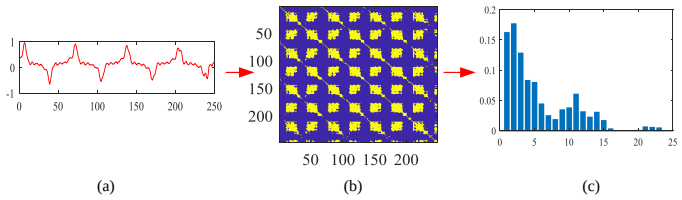

Figure 4.17: Recurrence Quantification analysis. (a) Disturbance signal for sudden load change (E4), (b) its recurrence plot and (c) histogram of diagonal line length

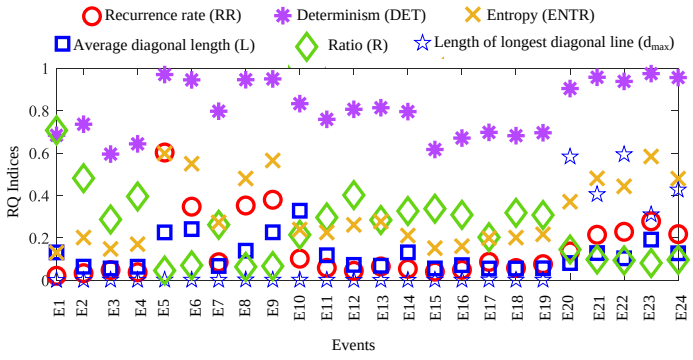

Figure 4.18: Event-wise six recurrence indices

In this study, a total of 4800 disturbance signals and their respective RP were created. At a time, 30 images are fed to the network in a batch. As an optimizer, adaptive moment estimation (*adam*) has been chosen. Figure 4.19 shows the loss function vanishes at 300 iterations and the classifier's validation accuracy reaches its saturation at 98.91%. The total learnable parameters and memory requirement are 6449336 and 24.6 MB respectively.

In Figure 4.20, the outputs at every stage, from feature extraction to final classification, are shown for three events in three major categories. For instance, Figure 4.20(a) depicts that 227×227 RP for capacitance

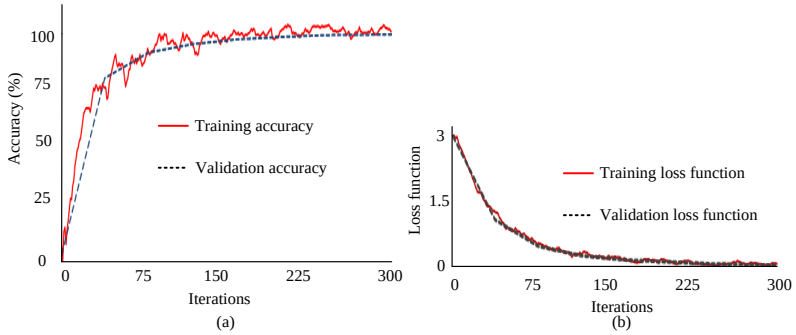

Figure 4.19: Training and validation accuracy and loss function variation with iteration count

switching (E1) has been converted to $red - green - blue$ (RGB) three-channel image to make it compliant with convolution operation. 3×3, 16 kernel filters are convoluted with this RGB image and $227 \times 227 \times 16$ feature maps are obtained. Then a max-pooling operation is performed to simplify the maps to form 113×113 of the same number of maps. In this way, three times convolution-max pooling operations are performed and finally, a flattened layer of 50176 neurons is fed to the deep neural network (DNN) and a $softmax$ classifier is applied. Besides, a double line to ground fault (E13) and a dual event of islanding followed by single phasing (E24) have also been depicted in Figure 4.20(b) and (c).

4.3.2.4 Performance Evaluation

The most common event-wise performance indices, like true positive (TP), true negative (TN), false positive (FP), and false negative (FN) are calculated from the confusion matrix shown in Figure 4.21 using the formulae given from (4.21) to (4.25) of Section 4.2.2.4.

Here, j indicates the prediction event index, i stands for the actual event index, and $c_{i,j}$ is the value at i^{th} row and j^{th} column. Figure 4.22 depicts performance indices for all 24 events.

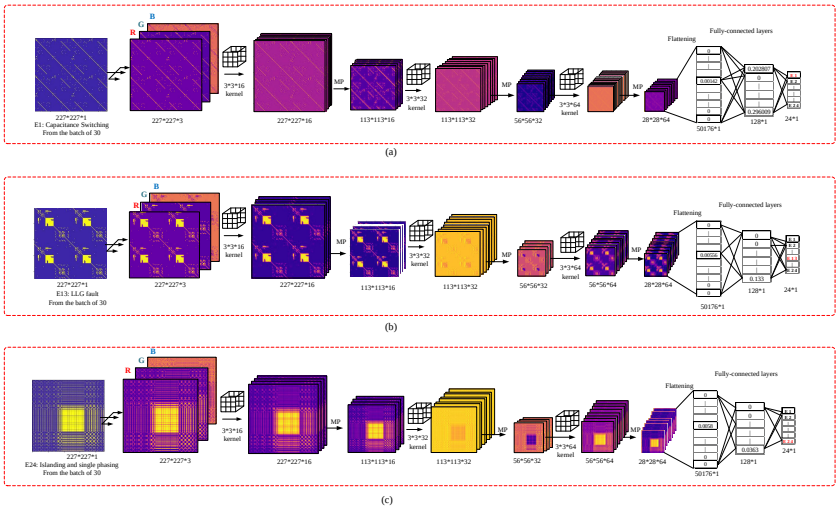

Figure 4.20: Feature extraction and classification from recurrence plot (RP) for (a) capacitor switching (E1) (b) double line to ground fault (E13) and (c) dual events of islanding and load shedding (E24)

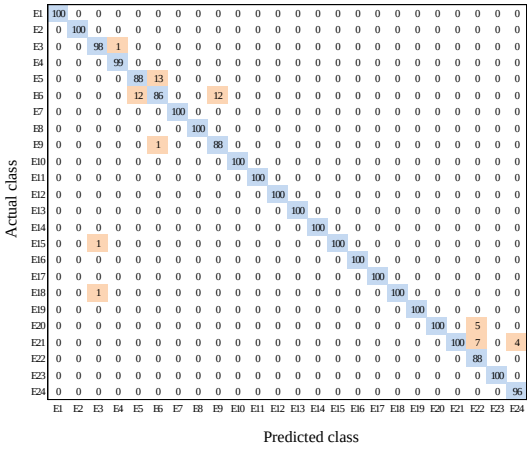

Figure 4.21: Confusion matrix

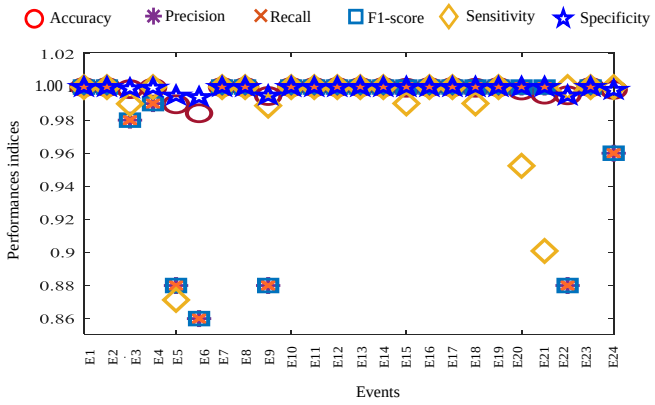

Figure 4.22: Event-wise six performance evaluation indices

The proposed classifier has been tested for different training data and has been compared with other benchmark machine learning and deep learning techniques, as shown in Table 4.11.

Table 4.11: Variation of accuracy concerning percentage of training data

Percentage of training data	Validation accuracy (in %) for different methods		
	RQA+SVM	RP+BILSTM	**Proposed RP+CNN**
50%	79.04	95.96	**97.25**
60%	81.35	97.24	**97.58**
70%	82.09	97.85	**97.97**
80%	83.12	98	**98.91**

The performance of the proposed classifier has also been observed under various noise levels, and the results show its ability to perform more than 97% under highly noisy conditions.

In this study, five multi-event disturbances were considered in addition to the single individual events and the classification tasks have been carried out in two different parts. At the initial stage, twenty-one mixed disturbances were successfully classified using the CNN-BiLSTM-based RNN algorithm with 98.57% accuracy. At the end all twenty-four

Table 4.12: Performance of the proposed method under noisy environment

SNR level (in dB)	Accuracy (in %)
Without noise	98.91
80	98.72
60	98.05
40	97.89
20	97.79

mixed disturbances were considered. A Recurrence plot-based image processing technique has been implemented for feature extraction and a customised CNN algorithm was designed. An accuracy level of 98.91% has been achieved and the proposed classifier performs the classification task satisfactorily in high noise conditions.

4.4 Classification of Multiple PSD Events using DWT-DFA-RQA Features Employing UMAP Analysis

In this section, a total of 24 different power system disturbances commonly occurring in the DG-based grid-connected network have been detected. A category-wise visual representation on a 2D plane has been provided using the Uniform Manifold Approximation and Projection (UMAP) technique. This technique has been applied on a feature matrix obtained from three signal-processing tools. Using Discrete Wavelet Transform (DWT), statistical features of approximate and detail coefficients of each disturbance signal are merged with the features obtained from Detrended Fluctuation Analysis (DFA) and Recurrence Quantization Analysis (RQA) to form 4800×74 feature matrix along with the labelled categories. The UMAP model has been trained by this labelled feature matrix. This non-linear model helps to reduce the dimension of

the problem and provides a categorical projection in the 2D plane. The category-wise visual 2D representation clearly proves the effectiveness of the model in identifying each class of power system disturbances.

In this context, several research works are going on for the analysis of different power system disturbance events, faults and its classification [140, 141, 65, 142, 71]. In [140], it has been reported about the transmission line fault classification of a DG-based network using a deep belief network and Discrete Wavelet Transform (DWT). Similarly, in [141], the islanding and power quality disturbances of microgrid networks, consisting of PV generations, have been classified using a signal processing-based regression classifier. In [65], the authors analysed the multiple power quality disturbances by extreme machine learning technique which is based on morphological operation and kernel parameter optimization. The power quality events of smart grids have been sensed remotely and classified using AI tools, reported in [142]. A few pieces of literature addressed the multi-disturbance classification, consists of various faults, power quality situations, islanding, mechanical power interruption, and switching transients, using machine learning methods. A deep learning method based on customized Alexnet algorithm has been reported in [71]. In the aforementioned articles, the researchers have considered only single disturbance type events happened at a time. However, in a practical scenario, an alarming situation may arise when more than one type of disturbances happen at the same time. Hence, it is also necessary to identify that condition and classify that events from the other disturbance events. However, there are very few articles in which those large numbers and categories of disturbance have been studied.

In this study, a total of 24 disturbance classes have been considered and identified using Uniform Manifold Approximation and Projection (UMAP). It is completely a new idea for power system disturbance classification without using any deep learning-based classifiers.

The UMAP can perform both dimensionality reduction and classification tasks through data visualization [143]-[146]. Therefore, no machine learning classifier is necessary for the classification job. The effective performance of the UMAP algorithm requires a high-dimensional feature matrix. Here, three different signal processing techniques—DWT, detrended fluctuation analysis (DFA), and recurrence quantification analysis (RQA) have been applied to extract a large number of features from disturbance signals that are sensed by the data acquisition system in the experimental setup. The signals have been decomposed through DWT since most of the disturbance signals are non-stationary in nature. The DWT coefficients provide significant information about each signal, as in [147]- [150]. The trending features of each signal can be visualised using DFA in a better way [72] and [74]. Recurrence plot (RP) indices describing the repeatability of the states with some tolerances have been included in the feature matrix to get in-depth information on time series data [151] - [153].

4.5 Disturbance Signal Creation

In the process of experimentation, a 3 kW distributed Generator (DG) operated from a DC shunt motor has been considered for supplying power to different loads and also utilised for connecting with the main grid as shown in Figure 2.1 of Chapter 2, Section 2.1.1.1.

In this study, the disturbances of different major categories have been considered. A total of 24 different disturbance classes of events (D1 to D24) have been created as tabulated in Table 4.13. Out of those, D1 to D9 fall under normal events, D10 to D19 fall in the fault category, and D20 to D24 have been created by combining two events. For each class, 200 events have been generated. A total of 4800 signals from 4800 events have been recorded for the analysis.

Table 4.13: All considered disturbance categories

Class Code	Disturbance Type	Class Code	Disturbance Type
D1	kVAR greater switching	D13	Two-line conductors shorted with ground
D2	kVAR greater switching	D14	3-phase fault at no load
D3	Power Electronic Devices	D15	3-phase fault at heating load
D4	Load Demand Variation	D16	LLL fault with inductive load
D5	Battery Charging	D17	Sudden single phasing
D6	Rotating machine Starting	D18	DG input power interrupted
D7	Sudden islanding at no load	D19	High Impedance Fault (HIF)
D8	Sudden isolating when load matches with generation	D20	Sudden islanding with Battery Charge
D9	Sudden isolating when DG feeding Grid	D21	Sudden islanding with Load Shedding
D10	Single Line to Ground Fault	D22	Sudden islanding with IM starting
D11	SLG with star point is solidly grounded	D23	Sudden islanding with open circuit fault
D12	Any two lines shorted	D24	Sudden islanding with sudden single-phasing

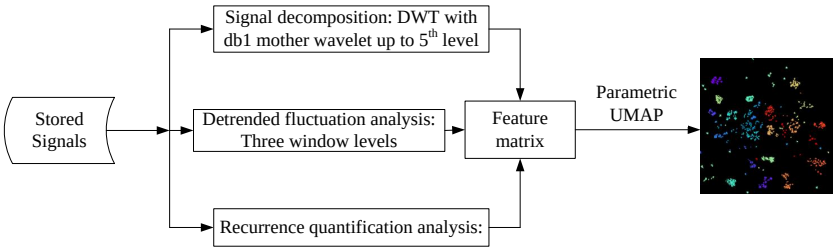

Figure 4.23: Whole process of dimentionality reduction and data visualisation

4.6 Methodology

All the stored signals have been fed to three distinct algorithms as shown in Figure 4.23. In the first algorithm, signals were decomposed up to the fifth level using discrete wavelet transform (DWT) with *db1* mother wavelet. In the second phase, Detrended Fluctuation Analysis (DFA) has been conducted to obtain the trending profile of all signals and at the final stage, recurrence qualification analysis (RQA) has been used to obtain the recurrence features which as a whole describes the repeatability pattern of different discrete states of a signal. For each signal, the features obtained from these three algorithms have been combined together to form a 74-dimensional vector. A labeled featured matrix of (4800×74) has been fed to a suitably tuned Uniform Manifold Approximation and Projection (UMAP) algorithm.

4.6.1 DWT-based Feature Extraction

The normalized discrete signal, $\mathbf{X}$ has been decomposed with the help of $db1$ mother wavelet up to fifth order using Equations (4.33) and (4.34) [147].

$$A_{\phi}[i_0, j] = \frac{1}{\sqrt{S}} \sum_{n} x[n] \phi_{i_0,j}[n] \tag{4.33}$$

$$D_{\psi}[i,j] = \frac{1}{\sqrt{S}} \sum_{n} x[n]\psi_{i,j}[n] \tag{4.34}$$

Where S is the number of samples and equals 2^i. i stands for the number of transform levels. ϕ and ψ are scaling factor and wavelet function, respectively, as indicated in Equations (4.35) and (4.36).

$$\phi_{i,j}[n] = 2^{\frac{i}{2}}\phi[2^i n - j] \tag{4.35}$$

$$\psi_{i,j}[n] = 2^{\frac{i}{2}}\psi[2^i n - j] \tag{4.36}$$

Therefore, each signal $\mathbf{X}$ comprises approximate and detailed coefficients up to the fifth level as given in Equation (4.37)

$$\mathbf{X} = \mathbf{A}_{\phi}5 + \mathbf{D}_{\psi}1 + \mathbf{D}_{\psi}2 + \mathbf{D}_{\psi}3 + \mathbf{D}_{\psi}4 + \mathbf{D}_{\psi}5 \tag{4.37}$$

In this study, ten statistical attributes for each decomposed component have been considered. These are Maximum value, minimum value, peak-to-peak value, mean, variance, standard deviation, median, rms, kurtosis, and skewness. The derived feature matrix, $\mathbf{X}_{DWT}$ would have a dimension of 4800×60 for all 4800 events.

4.6.2 DFA-based Feature Extraction

Detrended Fluctuation Analysis (DFA) has been carried out to extract the trending features of each signal [72]. In this method, a trending profile of any signal *x(i)* has been expressed using Equation (4.38).

$$y(k) = \sum_{i=1}^{k} x(i) - \hat{x} \tag{4.38}$$

This trending profile *y(k)* has been divided into a number of non-overlapping windows of size n, so that the product of n and s will be the nearest

integer of N. (i.e. $N \geq n \times s$). The mean square fluctuation for window $z(n,p)$ is given by Equation (4.39)

$$z(n,p) = \frac{1}{n}\sum_{p=1}^{s}\sum_{i=1}^{n} y_{i,p} \tag{4.39}$$

The corresponding RMS value has been derived using Equation (4.40).

$$U(n) = \left[\sum_{p=1}^{s} z(n,p)\right]^{\frac{1}{2}} \tag{4.40}$$

The RMS value of this trending signal $U(n)$ has been expressed in terms of the power of the window size n as shown in Equation (4.41)

$$U(n) \propto n^{\alpha} \tag{4.41}$$

$$or, U(n) = Cn^{\alpha} \tag{4.42}$$

taking log_e,

$$log_e U(n) = \alpha\ log_e n + log_e C \tag{4.43}$$

which reduces to,

$$y' = \alpha x' + \beta \tag{4.44}$$

This linear equation has been formed for three window-size regions, as given in the Figure 3.4 of Chapter 3, Section 3.2.1.2. The line segments PQ, RS and TV are characterized by their slopes $(\alpha_s, \alpha_m, \alpha_l)$, intersections $(\beta_s, \beta_m, \beta_l)$ and the time series dimension (D). Thus, the DFA-based feature matrix $\mathbf{X}_{DFA}$ of 4800×7 has been formed using the formulae given in Figure 3.3 of Chapter 3, Section 3.2.1.2.

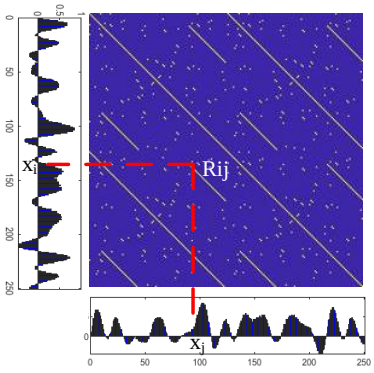

Figure 4.24: Recurrence Plot formation

4.6.3 RQA-based Feature Extraction

Each time series data has been characterized by seven Recurrence Plot (RP) indices, which in turn describe the occurrences of different states in the acquired signal. The entry in the RP matrix corresponding to i^{th} and j^{th} sample points (i.e. x_i and x_j) can be obtained using Equation (4.45) by applying *Heaviside* function ($\mathcal{H}$) on the state difference with a constant cut-off (ϵ) known as threshold distance [151].

$$R_{ij} = \mathcal{H}\left(\epsilon - ||x_i - x_j||\right) \tag{4.45}$$

Here $||.||$ is the Euclidean norm. The RP indices –recurrence rate (Q_1), determinism (Q_2), ratio (Q_3), average length of the diagonal lines (Q_4), entropy (Q_5), largest diagonal line (Q_6) are calculated using Equations (4.27) to (4.32) of Section 4.3.1.4 and another index – laminarity (Q_7) is calculated using Equation (4.46). An RQA-based feature matrix $\mathbf{X}_{RQA}$ of 4800×7 has been formed.

4.6.3.1 Laminarity, Q7:

$$Q7 = \frac{\sum_{v=v_{min}}^{N} vp(v)}{\sum_{v=1}^{N} vp(v)} \tag{4.46}$$

Where v_{min} stands for minimum vertical length.

These three feature matrices, as mentioned in the three consecutive subsections are combined together to form a complete feature matrix, $\mathbf{X}$ of 4800×74 with their respective classes placed at 75^{th} column as given in Equation (4.47).

$$\mathbf{X} = [\mathbf{X}_{DWT} \quad \mathbf{X}_{DFA} \quad \mathbf{X}_{RQA} \quad \mathbf{label}]_{4800\times 75} \tag{4.47}$$

4.6.4 Dimensionality Reduction and data visualization by UMAP

An advanced state-of-the-art dimensionality reduction technique, known as Uniform Manifold Approximation and projection (UMAP) has been applied to visualize the data set in 2D. This technique involves the following two major steps.

4.6.4.0.1 Formation of Simplicial Structure: For each data point, x_i, the Euclidean distances of all the considered neighbors are calculated and therefrom, the similarity scores have been evaluated.

The Euclidean distance between x_i and x_j is given by Equation (4.48).

$$d(x_i, x_j) = \left[\sum_{l=1}^{L} (f_{il} - f_{jl})^2\right]^{\frac{1}{2}} \tag{4.48}$$

Where, f_{ik} and f_{jk} are k^{th} feature of x_i and x_j data points, and $d(x_i, x_j) = d(x_j, x_i)$ $\forall$ i and j $\in$ [1 to 4800], but i $\neq$ j.

The relative edge values (w_{ij}) of x_j with respect to x_i point is given using Equation (4.49).

$$w_{ij} = exp\left[-\left(\frac{d(x_i, x_j) - \rho_i}{\sigma_i}\right)\right] \tag{4.49}$$

The similarity score for x_i can be given by Equation (4.50).

$$w_i = \sum_{j=1}^{k} exp\left[-\left(\frac{d(x_i, x_j) - \rho_i}{\sigma_i}\right)\right] \tag{4.50}$$

Here, σ_i is *Euclidean* distance of the nearest neighbor from x_i and it is obtained using Equation (4.51)

$$\rho_i = min\{d(x_i, x_j)\} \tag{4.51}$$

where 1 $\leq$ j $\leq$ k but, i $\neq$ j and ρ_i is a scaling factor and has been tuned iteratively to a value so that the similarity score for each data point becomes $log_2(k)$. As shown in Figure 4.25, all the data points have been arranged with respect to x_i. Out of the considered 1500 neighbours, $x_{i,n}$ is the nearest neighbour at a distance $d(x_{i,n}) = \rho_i$. With an exponential kernel its similarity score with respect to x_i is unity. Beyond this nearest neighbour, this value decreases exponentially. The scaling factor σ_i has been tuned after each iteration to ensure that the sum of the similarity scores becomes 10.55 (i.e. $log_2 1500$). Therefore, the condition in Equation (4.52) has to be ensured.

$$1 + \sum_{j=2}^{1500} w_{ij}^{(r)} = log_2 1500 = 10.55 \tag{4.52}$$

A total of 4800 1-simplex graphs of 1500 data points are formed. From these 4800, simplex graphs, a Fuzzy Simplicial set has been constructed using a fuzzy membership function as indicated in Equation

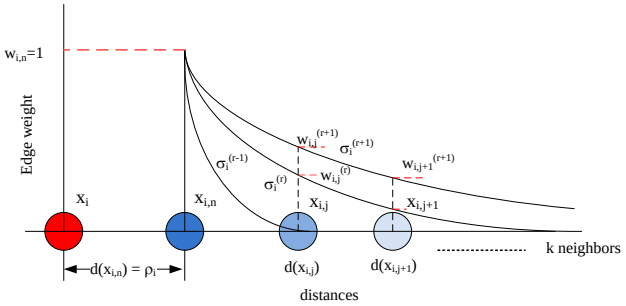

Figure 4.25: Variation of similarity scores w_{ij} with scaling factor σ_i in different iteration (r)

(4.53).

$$Fuzzy\ simplicial\ set = \bigcup_{i=1}^{N} FinSing(\mathbf{X}, w_i) \tag{4.53}$$

The combined edge weight matrix $\mathbf{W}_c$ is obtained using the merging approach, according to which the combined edge weight is obtained by subtracting the probability that no edge exists from the probability of the edges that exist as given in Equation (4.54).

$$\mathbf{W}_c = \mathbf{W} + \mathbf{W}^T - \mathbf{W}.\mathbf{W}^T \tag{4.54}$$

4.6.4.0.2 Layout Optimisation: The simplicial set has been optimized by comparing the edge probability matrices of high (H) and low (L) dimensional sets.

$$H = \begin{bmatrix} w_h(1,1) & w_h(1,2) & .. & w_h(1,4800) \\ w_h(2,1) & .... & ... & w_h(2,4800) \\ .... & ..... & ... & ... \\ .... & ..... & ... & ... \\ w_h(4800,1) & ..... & .... & w_h(4800,4800) \end{bmatrix} \tag{4.55}$$

$$L = \begin{bmatrix} w_l(1,1) & w_l(1,2) & ..... & w_l(1,4800) \\ w_l(2,1) & .... & ..... & w_l(2,4800) \\ .... & ..... & ..... & ..... \\ .... & ..... & ..... & ..... \\ w_l(4800,1) & ..... & .... & w_l(4800,4800) \end{bmatrix} \tag{4.56}$$

The loss function has been formulated using cross-entropy by comparing the edge probabilities of H and L, as given in Equation (4.57).

$$\mathcal{L} = \sum_{e=1}^{E} \left[w_h(e)\ log\frac{w_h(e)}{w_l(e)} + (1 - w_h(e))\ log\frac{(1 - w_h(e))}{(1 - w_l(e))} \right] \tag{4.57}$$

The first and second terms are called attraction force (push) and repulsion force (pull), respectively. The higher the edge probability between two data points, the larger would be the attractive force, and the lower would be the repulsive force. As a result, these two data points come closer to each other. The reverse happens when edge probability decreases. For minimizing the loss function ($\mathcal{L}$), the stochastic gradient descent (SGD) method has been adopted.

4.7 Results

In this section, initially, the extracted features have been presented sequentially and a composite feature matrix has been shown in brief. In the later part, category-wise visual classification has been made.

4.7.1 DWT-based features

All 4800 stored signals were decomposed using discrete wavelet transform (DWT) with the help of *db*1 mother wavelet up to the fifth level. One normalized specimen signal (E1) for capacitance switching (D1)

has been shown in Figure 4.26(a). For better visibility, the sample range from 50 to 140 has been shown. From the detailed (DT1 to DT5) and approximate (A5) coefficients as shown in Figure 4.26(b), the respective histograms have been introduced in Figure 4.26(c). Therefore, the feature vector $\mathbf{X}_{DWT,E1}$ of dimension 60 has been formed by combining 10 statistical features for each of the six histograms. Thus, the derived $\mathbf{X}_{DWT,E1}$ vector, so obtained, has been given in Equation (4.58)

$$\mathbf{X}_{DWT,E1} = [0.0146 \quad 0.00057 \quad 0.01076 \quad ..... \quad -0.00104]^T \tag{4.58}$$

As an output of the DWT algorithm, 4800 such 60-dimensional vectors (i.e. $\mathbf{X}_{DWT,E1}$ to $\mathbf{X}_{DWT,E4800}$) are obtained.

4.7.2 DFA-based features

Detrended fluctuation curves have been constructed for all signals, considering three ranges of window numbers: $4 \leq n \leq 164$, $164 \leq n \leq 324$ and $324 \leq n \leq 484$. Here, in the Figure 4.27(b), detrended fluctuation curve has been shown for the event in the category D7 given in Figure 4.27(a) where the disturbance due to islanding has been shown. From the detrended curve, all seven defined features ($D, \alpha_s, \alpha_m, \alpha_l, \beta_s, \beta_m$ and β_l) have been tabulated in Figure 4.27(c). In the end, the DFA algorithm results in 4800 DFA vectors of 7 dimensions (i.e. $\mathbf{X}_{DFA,E1}$ to $\mathbf{X}_{DFA,E4800}$)

4.7.3 RQA-based features

The recurrence plot (RP) for all 4800 signals has been constructed. From the histogram of diagonal and vertical lengths, seven non-correlated quantities (Q1 to Q7) have been found with the threshold, ϵ equal to 0.5. The RP of the event from the dual disturbance, D22 (i.e. islanding followed by induction motor starting) has been shown in Figure 4.28(b).

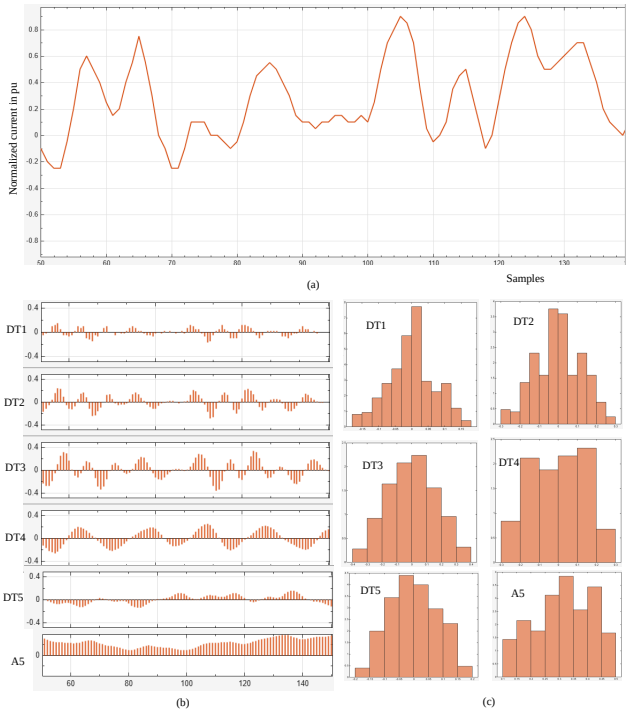

Figure 4.26: DWT-based extracted features. (a) Acquired signal of the event, E1 from the D1 category. (b) Approximate and detailed discrete coefficients up to the fifth level. (c) Histogram of all decomposed signals.

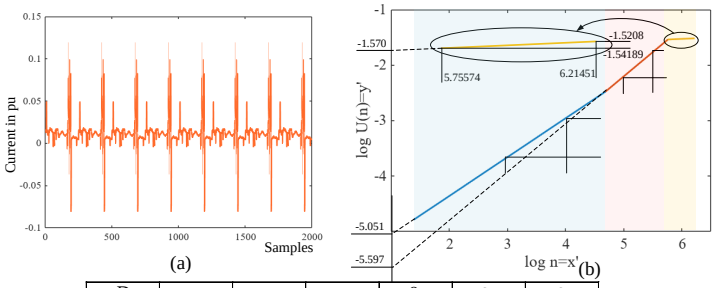

D	α_s	α_m	α_l	β_s	β_m	β_l
2.3	0.7	0.8752	0.046	-5.051	-5.597	-1.570

(c)

Figure 4.27: DFA-based features (a) Line current for sudden islanding (D7). (b) Its detrended fluctuation curve with all characteristic parameters (c) seven DFA parameters in tabular form

The stored current signal has been shown in Figure 4.28(a) and derived recurrence quantities have been tabulated in Figure 4.28(c). Thus, the RP algorithm output gives $\mathbf{X}_{RP,E1}$ to $\mathbf{X}_{RP,E4800}$, a total of 4800 seven-dimensional vectors.

4.7.4 Composite 4800× 74 feature matrix

DWT, DFA and RP-based 60, 7 and 7 features, respectively have been combined together to form 4800× 74 feature matrix as shown in Figure 4.29. All the elements of the feature matrix have been normalized and a label vector has been added to form 4800×75 labeled feature matrix.

Mutual correlation among the features has been investigated and presented in Figure 4.30. Out of the 74 features, the correlation has been shown for 6 features. Among these, enlarged view of the correlation between f1 and f2 features have been shown for the sake of visibility.

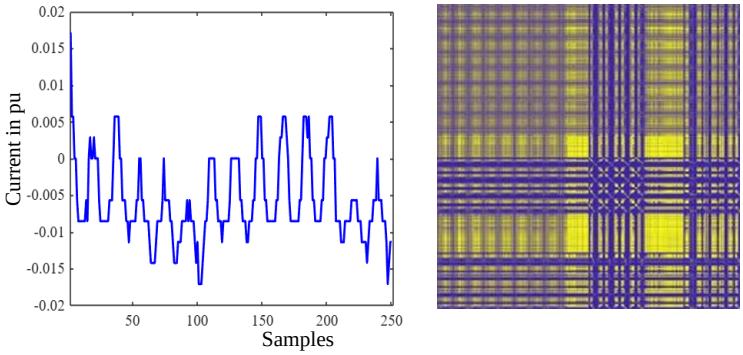

(a) (b)

Q1	Q2	Q3	Q4	Q5	Q6	Q7
0.0118633	0.0206785	0.0168093	0.0066833	0.0204124	0.0177345	0.0143659

(c)

Figure 4.28: RP extracted features (a) current signal of a dual event from category D22 (b) respective recurrence plot (c) RP quantification features

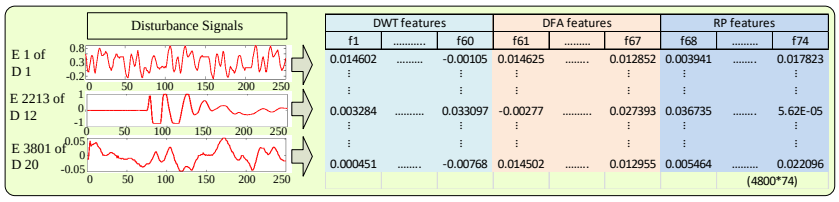

Figure 4.29: Disturbance signals and their combined features

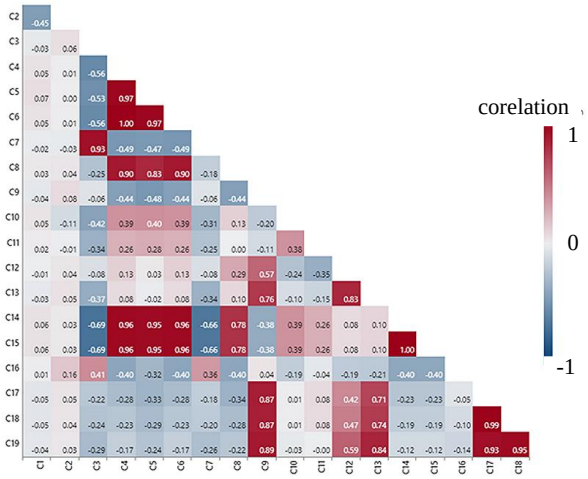

Figure 4.30: Graphical presentation of the correlation among the features

Table 4.14: Relative distance matrix of all 4800 data points

Column index →

Row index ↓	0	1	…….	4797	4798	4799
0	0	0.081915	…	0.061581	0.066727	0.056176
1	0.081915	0	…	0.08734	0.088468	0.088118
2	0.069204	0.077726	…	0.083954	0.089545	0.073304
3	0.102517	0.112665	…	0.095331	0.111501	0.100096
4	0.089396	0.120473	…	0.09072	0.12214	0.091228
...	...	...	…	...	...	...
4795	0.165063	0.178716	…	0.165438	0.162614	0.16115
4796	0.061038	0.084127	…	0.079604	0.0541	0.074562
4797	0.061581	0.08734	…	0	0.080966	0.029975
4798	0.066727	0.088468	…	0.080966	0	0.076746
4799	0.056176	0.088118	…	0.029975	0.076746	0

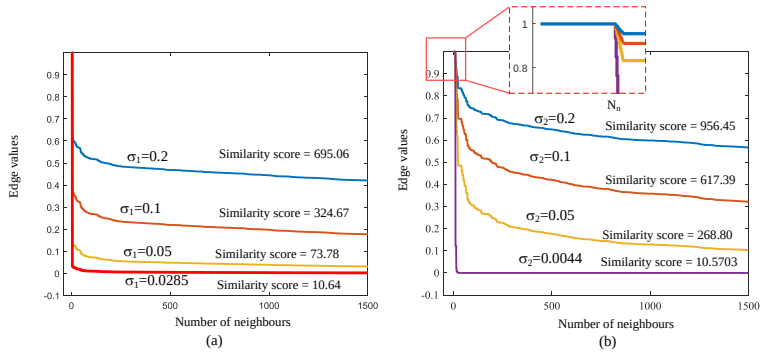

Figure 4.31: Relative edge values for event data points (a) 1 and (b) 2 with 1500 neighbors for different scaling factors, σ

4.7.5 Distance matrix

The Euclidean distances describing the mutual positions of the data points in 74-dimensional space have been evaluated and presented in Table 4.14.

With respect to each data point, other data points have been placed in similarity scores versus the Euclidean distance curve. The scaling factor has been tuned to a value for which the sum of the similarity scores of 1500 neighbors becomes 10.55. two such curves for the first two data points have been shown in Figure 4.31(a) and (b). It is obvious from the curves that the similarity score for the nearest neighbor is unity. It is also observed that the values of σ_1 and σ_2 are 0.0285 and 0.0044 respectively for the number of neighbors to be 1500.

Initially, with the hyperparameters mentioned in Table 4.15, the UMAP algorithm has been applied to 60 DWT-based features. Figure 4.32 shows the labelled and colour-shaded data points. This visual output clearly indicates that only DWT features are not enough to segregate the categories distinctly. Then, with the same hyperparameters, a uniform manifold has been obtained using DWT, DFA and RP-based 74 features. Figure 4.33 (c) shows the data points with a minimum distance

Table 4.15: Considered hyperparameters for UMAP dimensionality reduction and data visualization

Hyperparameter	**Value**
Number of neighbors	1500
Number of components	2
Minimum distance	0.9
Metric	Euclidean distance
Loss function	Cross entropy
Optimization method	SGD

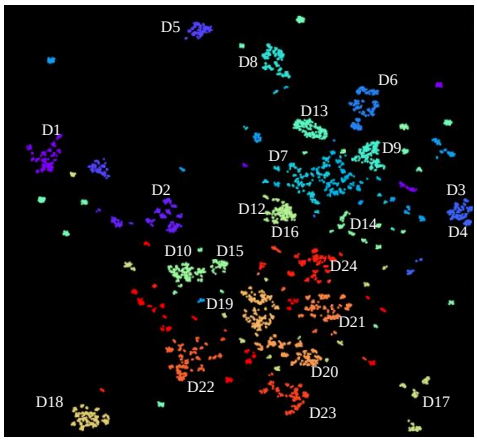

Figure 4.32: UMAP-based clustering using 60 DWT features

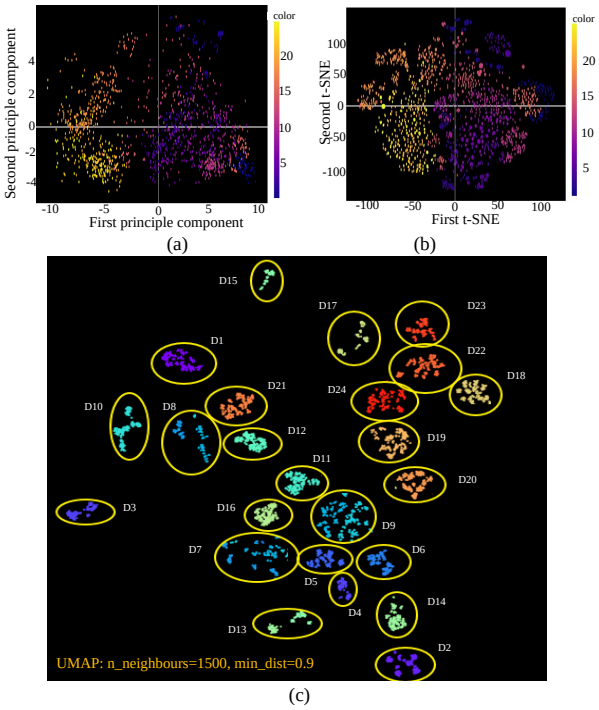

Figure 4.33: Supervised data clustering in 2D embedding. (a) PCA-based clustering (b) t-SNE-based data clustering (c) UMAP-based clustering.

of 0.9 and all 24 categories are distinctly located in 2D. The other two well-established dimensionality reduction techniques- Principal Component Analysis and t-distributed Stochastic Neighbor Embedding, have also been studied for comparison and their 2D outputs have been shown in Figure 4.33 (a) and (b). Figure 4.33 (c) clearly reveals that each category has been visually classified in 2D embedding.

In this work, the visual classifications of a total of 24 power system disturbances in 2D have been presented. For this, an advanced dimensional reduction and data visualization technique, UMAP has been applied. A total of 74 features were extracted from three different signal analysis methods. A feature matrix of 4800×74 size has been successfully fed to the UMAP algorithm to recognize 24 distinct classes separately. Besides, other two-dimension reduction algorithms have been studied to show this method's superiority over others and the visual classification performance has been investigated for the different number of features. Another important speciality of the method is its ability to classify all categories effectively for a large number of features. To validate this, the same algorithm has been applied to the same events with only 60 DWT-based features.

CHAPTER 5

Conclusion & Future Work Recommendations

5.1 Conclusion

In this thesis, all possible power system disturbances due to the advancement of power networks with respect to infrastructural development, DG integration, and the havoc use of power electronic devices were investigated and studied. This study has been done for power system monitoring and protection. To identify the disturbance category, a few AI-based disturbance classifiers have been proposed. In different stages of the study, different numbers and types of disturbance categories were considered. The performance of the proposed classifiers was evaluated using conventional performance indices and a confusion matrix. In all the cases, the designed classifiers were compared with other variants. Besides, the proposed models have also been compared with other state-of-the-art techniques addressed by researchers working in the same field. In the introductory chapter, the origins of all power system disturbances were identified, and the causes have been defined by disturbance terminologies. Few adverse effects of such disturbances were briefed. As the

work has progressed, more disturbance categories have been included in the study.

In Chapter 2, a laboratory-based circuit for grid-connected distributed generation has been presented. All switching and fault-creating arrangements have been prepared for disturbance creation. Some of the disturbances, named dual events, have been created using two different events, creating both at a time or simultaneously.

A very simple, robust, and accurate machine-learning method for the detection of the most commonly occurring power system disturbances in microgrid systems was dealt in chapter 3. The problem with a lower number of experimental events due to thermal restriction has been handled using binary unsupervised k-mean clustering, which enables the generation of big data. The signal trend and fluctuation pattern have been analysed by its DFA characteristics feature and a PCA-based dimensionality reduction technique helped us reduce the feature matrix from seven to four. This technique also helped in reducing the memory requirement and also made 1-NN machine learning to predict a signal with 97.18% accuracy in less time. However, this work is limited to the eleven classes of disturbance as mentioned. The other significant disturbances that happen in MG systems, such as single phasing, high impedance faults, etc., have been incorporated into the study to enhance their potentiality.

With a comparatively larger number of classes, an MM-based method for sensing PSD using principal component analysis-aided support vector machines has been used. This disturbance study is pertinent for the reliable operation of power system networks. MM operators have been used to extract significant features from experimentally recorded signals. The input vectors to train the classifier have been formed by reducing the data dimensionality of extracted features using PCA. Selected 14 PCs are used for sensing the PSD using quadratic kernel function-based

SVM. The result shows that the proposed method is capable of sensing PSD with reasonable accuracy and smaller computation time compared to the other methods present in the literature. The performance of the proposed method has been validated by using a confusion matrix. All feasible power system disturbances have been identified and classified by this algorithm with 99.3 % accuracy.

At the later stage of the study, a deep learning-based classifier has been proposed to classify power system disturbances. k-mean clustering technique has been applied to the recorded current signals for filtration. This helped in the generation of huge data that has made the training and validation process easier. With the *sgdm* optimizer and 30 batch size, a learning rate of 0.0003 results loss function to converge to an optimal value in minimum computational time and an accuracy of 98.46% has been achieved. It would be challenging to choose the proper combination of batch size and learning rate to train this classifier with a large number of data sets.

Finally, in chapter 4, five dual events have been added with categories considered in previous chapters. A customized CNN-BiLSTM-based RNN algorithm has been proposed. The performance indices of this classifier have been assessed to validate this technique. The overall accuracy obtained from the class-wise confusion matrix is 98.57%. The extraction and prediction methods of other classification techniques and their corresponding accuracy have also been compared with those of the proposed technique and very satisfactory results have been achieved for PSD classification. Besides, the classifier's performance is found to be acceptable even at high noise levels.

Besides, all the power system events have been classified with 98.91% accuracy by an RP-based customized CNN algorithm. This classification

study has also been performed using two other methods, considering different training datasets for comparison. Event-wise performance indices have been derived, which proves the efficacy of the proposed classifier. This classifier also performs satisfactorily in high noise conditions. The conventional monitoring system and the protection scheme can be revised by integrating this kind of algorithm to improve the flexibility and power quality in DG-based networks.

At the end of chapter 4, visual classifications of a total of 24 power system disturbances in 2D are presented. For this, an advanced dimensional reduction and data visualization technique, UMAP has been applied. A total of 74 features were extracted from three different signal analysis methods. A feature matrix of 4800×74 size has been successfully fed to the UMAP algorithm to recognise 24 distinct classes separately. Besides, other two-dimension reduction algorithms have been studied to show this method's superiority over others, and also the visual classification performance has been investigated for different numbers of features. Another important speciality of the method is its ability to classify all categories effectively for a large number of features. To validate this, the same algorithm has been applied to the same events with only 60 DWT-based features.

5.2 Future Work Recommendations

This study deals with the identification of different power system disturbances that occur because of some faults and normal operations. This work can further be extended as its continuation in the direction of disturbance mitigation and system protection. In this regard, a few recommendations have been highlighted below:

- Incorporation of the proposed classifiers into the low-cost proces-

sor at the point of common coupling (PCC) and fetching the classifier's output to the remote operating centre is still challenging.

• The severity of all types of disturbances is still left to be studied, and accordingly, the disturbance technique needs to be modified.

• Fast identification of any switching operation and mitigation of high-frequency transients to maintain the power system stability is still a challenging task.

• Coordination among the PCCs and the remotely located monitoring centre in view of the disturbance mitigation is left for further study.

Bibliography

[1] Wenxi, *et al*, "Analysis and proactive application of power disturbance data in modern power grid", Automatic Electric Power System, 45(04), 1–11 (2021).

[2] 1159-2009-IEEE Recommended Practice for Monitoring Electric Power Quality.

[3] Wenyuan, *et al*," Synchronized waveforms—A frontier of data-based power system and apparatus monitoring, protection, and control. IEEE Transactions, Power Delivery 37(1), 3–17 (2022).

[4] M. A. Saket, N. Shafiei and M. Ordonez, "Member, IEEE LLC Converters With Planar Transformers: Issues and Mitigation," IEEE Transactions on Power Electronics, vol. 32, no. 6, June 2017.

[5] IEEE Guide for the Application of Metal-Oxide Surge Arresters for Alternating-Current Systems, IEEE std. C62.22-1997 (New York: The Institute of Electrical and Electronics Engineers, http://standards.ieee.org/1998).

[6] Electrical Transients in Power Systems, Allan Greenwood.

[7] T.A. Short, Electric Power Distribution Handbook, Boca Raton, FL: CRC Press, 2004, ISBN 0-8493-1791-6.

[8] 2009 Victorian Bushfires Royal Commission, “Final report”, July 2010.

[9] Inspec: Trusted content and precision analytics, The Institution of Engineering and Technology.

[10] Electricity Grid Schematic” by MBizon R. Ott, “Power quality measurements,” in Proc. IEC 77A Low Frequency Phenomena, Working Group 9, 1999.

[11] A.A.B. Rújula, “Future development of the electricity systems with distributed generation,” Energy, vol. 34, no. 3, pp. 377-383, 2009.

[12] R. Igual, C. Medrano, “Research challenges in the real-time classification of power quality disturbances applicable to microgrids: A systematic review,” Renewable and Sustainable Energy Reviews, vol. 132, pp. 110050, 2020.

[13] Q.H. Wu, Z. Lu, T.Y. Ji, “Protective relaying of power systems using mathematical morphology,” Springer-Verlag, London, 2009.

[14] A.F. Bastos and S. Santoso, "Universal Waveshape-Based Disturbance Detection in Power Quality Data Using Similarity Metrics" IEEE trans. on Power Del., vol. 35, no. 4, August 2020.

[15] P. Khetarpal *et al*, "Power Quality Disturbances Detection and Classification Based on Deep Convolution Auto-Encoder Networks" IEEE Access, vol. 11, 2023.

[16] T. Zhong *et al*, "Power Quality Disturbance Recognition Based on Multiresolution S-Transform and Decision Tree" IEEE Access, vol. 7, pp. 88381, 2019.

[17] Y. Xu *et al*,"Detection and Classification of Power Quality Disturbances in Distribution Networks Based on VMD and DFA",

CSEE Journal of Power and Energy Systems, vol. 6, no. 1, pp. 122-131, 2020.

[18] R. Narayanaswami, D. Sundaresan and V.R. Prema,"The Mystery Curve: A Signal Processing Based Power Quality Disturbance Detection", IEEE Transactions on Industrial Electronics, vol. 68, no. 10, pp. 10078-10085, 2021.

[19] L. Lin *et al*, "Power Quality Disturbance Feature Selection and Pattern Recognition Based on Image Enhancement Techniques", IEEE Access, vol. 7, pp. 67889 - 67904, 2019.

[20] Z. Yang, H. Hua and J. Cao, "Multiple Impact Factor Based Accuracy Analysis for Power Quality Disturbance Detection", CSEE Journal of Power and Energy Systems, vol. 9, no. 1, pp. 88-100, 2023.

[21] N. Kishor *et al*, "Evolving Disturbances Detection and Classification in Real-time for Grid-Connected System", IEEE Transactions on Industrial Electronics, vol. 68, no. 9, pp. 8265-8273, 2021.

[22] T. Ravi and K.S. Kumar," Detection and Classification of Power Quality Disturbances Using Stockwell Transform and Improved Grey Wolf Optimization-Based Kernel Extreme Learning Machine" IEEE Access, vol. 11, pp. 61710- 61727, 2023.

[23] C. Cui *et al*,"Detection and Classification of Multiple Power Quality Disturbances Using Stockwell Transform and Deep Learning", IEEE Transactions on Instrumentation and Measurement, vol. 71, pp. 2519912 -2519923, 2022.

[24] S. Roy and S. Debnath," PSD based high impedance fault detection and classification in distribution system", Elsevier, Measurement, pp 108366- 108382, 2021.

[25] M. Paul and S. Debnath, "Fault Detection and Classification Scheme for Transmission Lines Connecting Windfarm Using Single end Impedance", IETE Journal of Research, 2021.

[26] Q. Zhou, *et al*, "Disturbance Classification Method for Microgrids Based on EEMD-Transformer-SVM," IEEE Access, vol. 11, 2023.

[27] Z. Li, H. Liu, J. Zhao, T. Bi and Q. Yang, "A Power System Disturbance Classification Method Robust to PMU Data Quality Issues," IEEE Transactions on Industrial Informatics, vol. 18, no. 1, pp. 130-142, Jan. 2022.

[28] S. Z. Hou, W. Guo, Z. Q. Wang and Y. T. Liu, "Deep-Learning-Based Fault Type Identification Using Modified CEEMDAN and Image Augmentation in Distribution Power Grid," IEEE Sensors Journal, vol. 22, no. 2, pp. 1583-1596, 15 Jan.15, 2022.

[29] J. Arrillaga, M. H. J. Bollen, and N. R. Watson. Power quality following deregulation. Proceedings IEEE, 88(2): 46–261, February, 2000.

[30] Saxena.D, Verma K. S and Singh S. N "Power quality event classification: an overview and key issues. IntJEngSciTechnol2010;2(3):186–99

[31] S. S. Roy, A. Paramane, J. Singh, S. Chatterjee, and A. K. Das, "Accurate Sensing of Insulator Surface Contamination Using Customized Convolutional Neural Network," IEEE Sensors Letters, vol. 7, no. 1, 2023.

[32] S. Chatterjee, A. Banik, S. Dalai, and B. Chatterjee, "Identification of salt and salinity level of 11kV contaminated porcelain disc insulator using STD-MRA analysis of leakage current," in Proc. Int. Conf. Condition Assessment Techn. Elect. Syst., 2015, pp. 242–246.

[33] A. K. Das, S. Deb, S. Chatterjee, B. Chatterjee and S. Dalai, "Convolutional neural network and Bi-directional long short memory hybrid deep network aided infrared image classification framework for non-contact monitoring of overhead insulators," IET Signal Processing, pp. 615-732, 2022.

[34] V. Pandya, U. P. Shukla, and A. M. Joshi, "Novel Features Extraction From EEG Signals for Epilepsy Detection Using Machine Learning Model," IEEE Sensors Letters, vol. 7, no. 10, October 2023.

[35] W. Li, Y. Tian, J. Dong and C. Fang, "A Hierarchical Three-Dimensional MLP-Based Model for EEG Emotion Recognition," IEEE Sensors Letters, vol. 7, no. 10, October 2023.

[36] P. Warule, S. P. Mishra, and S. Deb, "Frequency Analysis of Speech Signal Using Wavelet Synchrosqueezing Transform for Automatic Detection of Parkinson's Disease," IEEE Sensors Letters, vol. 7, no. 10, October 2023.

[37] T. Martins, *et al.*,"Detection of Power Quality Disturbance Using a Multidimensional Approach in an Embedded System," IEEE Latin America Transactions, vol. 17, no. 7, pp. 1102-1108, July 2019.

[38] A. Chakraborty, S. Chatterjee and R. Mandal, "Power Quality recognition in noisy environment employ- ing deep feature extraction from Cross Stockwell Spectrum Time-Frequency Images," Electrical Engineering, Springer Nature, September 2023.

[39] O. P. Mahela, A. G. Shaik, and N. Gupta, "A critical review of detection and classification of power quality events," Renew. Sustain. Energy Rev., vol. 41, pp. 495-505, January 2015.

[40] A. Thapar, T.K. Saha and Z.Y. Dong, "Investigation of power quality categorization and simulating its impact on sensitive electronic equipment," IEEE Power Energy Soc Gen Meet 2004;1:528–33.

[41] R.C. Dugan, M. F. McGranaghan and H. W. Beaty, "Electrical power systems quality," New York: McGraw-Hill; 1996; 1–38.

[42] R.A. Flore, "State of the art in the classification of power quality events, an overview," 10th international conference on harmonics and quality of power, vol. 1; 2002. p. 17–20.

[43] B. Morris, F. Roberto and T. Enrico, "A new proposal for power quality and custom power improvement: open UPQC," IEEE Trans Power Deliv 2009;24(October (4)):2107-1.

[44] T. Ahmet, S. Litfu and T. Mehmet, "A novel reference signal generation method for power quality improve ment of unified power quality conditioner," IEEE Trans Power Deliv 2011;26(October (4)):2205–14.

[45] D. Sovan *et al.* Rough-set-based feature selection and classification for power quality sensing device employing correlation techniques," IEEE Sens J2013;13 February.

[46] S. Daniel *et al* "Power quality factor for networks supplying unbalanced nonlinear loads." IEEE Trans Instrum Meas 2008;57 June:1268–74.

[47] B. Biswal *et al*, "A hybrid ant colony optimization technique for power signal pattern classification," Expert Syst Appl, 2011;38:6368–75.

[48] K. K. Hoong *et al* "An output regulation-based unified power quality conditioner with Kalman filters"IEEE Trans Ind Electron 2012, 59 November:4248–62.

[49] Wang Xiaoyu, Y. Jing, X. Wilsun and F. Walmir, "Practical power quality charts for motor starting assessment," IEEE Trans Power Deliv 2011;26(April (2)):799–808.

[50] Z. Ming, L. Kaicheng and H. Yisheng, "A real-time classification method of power quality disturbances," Electr Power Syst Res 2011;81:660–6.

[51] S. Kumar, T. W. S. Chow, and M. Pecht, "Approach to fault identification for electronic products using Mahalanobis distance," IEEE Transactions Instrumentation and Measurement, vol.59, no.8, pp.2055-2064,2010.

[52] T. A. George and D. Bones, "Harmonic power flow determination using the fast Fourier transform," IEEE Transactions Power Delivery, vol.6, pp.530-535, 1991.

[53] S.Santoso, et.al,"Power quality assessment via wavelet transform analysis." IEEE Transactions on Power Delivery, vol. 18, No. 2, pp.924-930, (1996).

[54] P.K.Dash, B.K.Panigrahi and G.Panda, "Power quality analysis using s-transform," IEEE Transactions Power Delivery, vol.18, no.2, pp.406-411, 2003.

[55] M.Zhang, K.C.Li and W.B.Hu "Automated classification of power quality disturbances using the S-transform," International Conference on Wavelet Analysis and Pattern Recognition, 2008.

[56] C. Venkatesh, D.V.S.S. Siva Sanna, and M. Sydulu, "Detection of voltage sag/swell and harmonics using discrete S-transform," TENCON 2008 -2008 IEEE Region Conference,2008.

[57] S.H.Cho, G.Jang and S.H. Kwon,"Time-frequency analysis of power-quality disturbances via the Gabor Wigner transform, "IEEE Transactions Power Delivery, vol.25, no.l, pp.494-499, 2010.

[58]] L.Yang, J.Yu and Y.Lai, "Disturbance Source Identification of Voltage Sags Based On Hilbert-Huang Transform," IEEE Power and Energy Engineering Conference (APPEEC) Asia-Pacific, 2010, pp.1-4.

[59] S.Kaewarsa, "Classification of power quality disturbances using S−transform based artificial neural networks," IEEE International Conference on Intelligent Computing and Intelligent Systems. pp.566-570, 2009.

[60] S. Ganguly and D. Samajpati, "Distributed Generation Allocation on Radial Distribution Networks Under Uncertainties of Load and Generation Using Genetic Algorithm", IEEE Transactions on Sustainable Energy, vol.6, no. 3, July 2015.

[61] L. I. Dulau, Mihail Abrudean, Dorin Bic, "Effects of Distributed Generation on Electric Power Systems", Procedia Technology, vol. 12, pp. 681-686, 2014.

[62] Khamis, Y. Xu, Z. Y. Dong and R. Zhang, "Faster Detection of Microgrid Islanding Events Using an Adaptive Ensemble Classifier," IEEE Transactions on Smart Grid, vol. 9, no. 3, pp. 1889-1899, May 2018.

[63] T. Cheng, et al, "Machine learning enabled learning based optimization algorithm in digital twin simulator for management of smart islanded solar-based microgrids", Solar Energy, vol. 250, pp. 241-247, 2023,

[64] M. F. Guo, N. C. Yang and W. F. Chen, "Deep-Learning-Based Fault Classification Using Hilbert Huang Transform and Convolutional Neural Network in Power Distribution Systems", IEEE Sensors Journal, vol. 19, no. 16, pp. 6905-6913, Aug., 2019.

[65] P.K. Dash, et al, "Multiple power quality disturbances analysis in photovoltaic integrated direct current microgrid using adaptive morphological filter with deep learning algorithm", Applied Energy, vol. 309, pp. 118454, 2022.

[66] A. Nasiri, *et al*, "Ball-Bearing Fault Detection of Squirrel-Cage Induction Motors Based on Single-Phase Stator Current Using Wavelet Packet Decomposition and Statistical Features", IEEE Transactions on Energy Conversion, pp. 1-10, 16 September 2024.

[67] V. Rafiei, *et al*, "Detection of Inter-turn Short Circuit in Stator Windings of Electric Machines using Magnetic Symmetry Index and Machine Learning Methods", IEEE Transactions on Energy Conversion, pp. 1-11, 26 July 2024.

[68] R. Pascual, *et al*, "Brushless Synchronous Machine Field Winding Interturn Fault Severity Estimation Through Deep Neural Networks, IEEE Transactions on Energy Conversion, pp. 1341-1351,01 December 2023.

[69] C. Fan *et al*, "Data-Driven Fault Detection of Multiple Open-Circuit Faults for MMC Systems Based on Long Short-Term Memory Networks ", CSEE Journal of Power and Energy Systems, vol. 10, no. 4, pp. 1563-1574, May 2024.

[70] Y. Xu, *et al*, "Power Quality Dectection and Classification in Active Distribution Networks Based on Improved Empiricial Wavelet Transform and Disperson Entropy ", CSEE Journal of Power and Energy Systems, vol. 8, no.6, pp. 1646-1658, October 2020.

[71] C. Jana, S. Banerjee, S. Maur, and S. Dalai, "Power system disturbance classification using CWT-guided tailor-made AlexNet CNN," IEEE Sensors Letters, 2024

[72] S. Das, *et al*, "Diagnosis of Power Quality Events Based on Detrended Fluctuation Analysis", IEEE Transactions on Industrial Electronics, vol. 65, no. 9, September 2018.

[73] P. A. Absal, *et al*, "Nonlinear analysis of cardiac rhythm fluctuations using DFA method", Physica Elsevier, 1999, 235-244.

[74] Y.Cui, *et al*, "Multiscale Adaptive Multifractal Detrended Fluctuation Analysis-Based Source Identification of Synchrophasor Data", IEEE Transactions on Smart Grid, vol. 13, no. 6, November 2022.

[75] W.Du, *et al*, "Fault Diagnosis Using Adaptive Multifractal Detrended Fluctuation Analysis" IEEE Transactions on Industrial Electronics, vol. 67, no. 3, March 2020.

[76] IEC Short-circuit currents in three-phase a.c. systems- Part 0: Calculation of currents, IEC Standard 60909-0:2016.

[77] G. R. Naik, "Advances in Principal Component Analysis-Research and Development," Springer, ISBN 978-981-10-6704-4, 2018

[78] P. Sanguansat, "Principal Component Analysis - Engineering Applications", Intech, ISBN 978-953-51-0182-6, 2012

[79] R. Zhai, J. Zeng and Z. Ge, "Structured Principal Component Analysis Model with Variable Correlation Constraint," IEEE Transactions on Control Systems Technology, vol. 30, no. 2, pp. 558-569, 2022

[80] T. Dimitrovska, U. Rudez and R. Mihalic, "Indirect Power-System Contingency Screening for Real-Time Applications Based on PCA,"

IEEE Transactions on Power Systems, vol. 33, no. 1, pp. 1080-1081, 2018

[81] J. Xie, *et al*, "An Efficient Global K-means Clustering Algorithm", Journal of Computers 6(2):271-279 February 2011

[82] M. Ali, *et al*, "Open switch fault diagnosis of cascade H-bridge multi-level inverter in distributed power generators by machine learning algorithms," Elsevier, Energy Reports 7, pp. 8929–8942, 2021.

[83] I.T. Jolliffe, "Principal Component Analysis," Second Edition, *Springer*, ISBN 0-387-95442-2, 2002.

[84] I.T.. Jolliffe, "Principal Component Analysis," Second Edition, Springer, ISBN 0-387-95442-2, 2002.

[85] M. Khodayar *et al*. "Deep learning in power systems research: A review," CSEE Journal of Power and Energy Systems, vol. 7, no. 2, pp. 209-220, March 2021.

[86] Z. Li *et al*. "A Power System Disturbance Classification Method Robust to PMU Data Quality Issues," IEEE Transactions on Industrial Informatics, vol. 18, no. 1, pp. 130-142, Jan. 2022.

[87] K. Özcanlı,*et al*. "Deep learning methods and applications for electrical power systems: A comprehensive review." International Journal of Energy Research. 44. 10.1002/er.5331, 2020.

[88] S Wang, H. Chen, "A novel deep learning method for the classification of power quality disturbances using deep convolutional neural network", Applied Energy, Volume 235, 2019, Pages 1126-1140.

[89] Mishra and Manohar, "Power quality disturbance detection and classification using signal processing and soft computing techniques:

A comprehensive review. *International Transactions on Electrical Energy Systems*. 2019.

[90] M. Wei, *et al*. "Distortion-Based Detection of High Impedance Fault in Distribution Systems," IEEE Transactions on Power Delivery, vol. 36, no. 3, pp. 1603-1618, June 2021.

[91] E. Styvaktakis, M. H. J. Bolen and I. Y. H. Gu, "Expert System for Classification and Analysis of Power System Events," IEEE Power Engineering Review, vol. 22, no. 2, pp. 64-64, Feb. 2002.

[92] S. Banerjee and P. S. Bhowmik, "Multiclass transient event classification in hybrid distribution network based on co-training of fine KNN and ensemble KNN classifier", Smart Science, Taylor & Francis, 2023.

[93] S. Z. Hou, W. Guo, Z. Q. Wang and Y. T. Liu, "Deep-Learning-Based Fault Type Identification Using Modified CEEMDAN and Image Augmentation in Distribution Power Grid," IEEE Sensors Journal, vol. 22, no. 2, pp. 1583-1596, Jan., 2022.

[94] S. Chatterjee, S. S. Roy, K. Samanta and S. Modak, "Sensing Wettability Condition of Insulation Surface Employing Convolutional Neural Network," IEEE Sensors Letters, vol. 4, no. 7, pp. 1-4, July 2020.

[95] Y. Guo *et al*. "An Improved AlexNet for Power Edge Transmission Line Anomaly Detection", IEEE Access, Vol. 8, pp. 97830 - 97838, 20 May 2020.

[96] J. G. S. Carvalho, et al, "High-impedance fault modeling and classification in power distribution networks", Electric Power Systems Research, 2022.

[97] D. Celeita, J. D. Perez and G. Ramos, "Assessment of a Decaying DC Offset Detector on CTs Measurements Applying Mathematical Morphology," IEEE Transactions on Industry Applications, vol. 55, no. 1, pp. 248-255, 2019.

[98] A. K. Das *et al*, "Sensing Surface Contamination of Metal Oxide Surge Arrester Through Resistive Leakage Current Signal Analysis by Mathematical Morphology," IEEE Sensors Journal, vol. 20, no. 16, pp. 9460-9468, 2020.

[99] H. H. Eldeeb *et al*, "Differential Mathematical Morphological-Based Online Diagnosis of Stator Interturn Failures in Direct Torque Control Drive Systems," IEEE Transactions on Industry Applications, vol. 56, no. 6, pp. 6272-6285, 2020.

[100] B.S. Chow, "Mathematical Morphology for Applications to Sensor Networks," IEEE Sensors Journal, vol. 12, no. 12, pp. 3473-3479, 2012.

[101] R. Godse and S. Bhat, "Mathematical Morphology-Based Feature-Extraction Technique for Detection and Classification of Faults on Power Transmission Line," IEEE Access, vol. 8, pp. 38459-38471, 2020.

[102] G.R. Naik, "Advances in Principal Component Analysis-Research and Development," Springer, ISBN 978-981-10-6704-4, 2018.

[103] M. Alamin *et al*, "Principal Component Analysis of Pulsed Eddy Current Response from Corrosion in Mild Steel," IEEE Sensors Journal, vol. 12, no. 8, pp. 2548-2553, 2012.

[104] J. Jiang *et al*, "Series Arc Detection and Complex Load Recognition Based on Principal Component Analysis and Support Vector Machine," IEEE Access, vol. 7, pp. 47221-47229, 2019.

[105] S. Xia *et al*, "A Spare Support Vector Machine Based Fault Detection Strategy on Key Lubricating Interfaces of Axial Piston Pumps," IEEE Access, vol. 7, pp. 178177-178186, 2019.

[106] S. T. Kandukuri *et al*, "A Two-Stage Fault Detection and Classification Scheme for Electrical Pitch Drives in Offshore Wind Farms Using Support Vector Machine," IEEE Transactions on Industry Applications, vol. 55, no. 5, pp. 5109-5118, 2019.

[107] Prof. Dr. Shigeo Abe, "Support Vector Machines for Pattern Classification" Springer London Dordrecht Heidelberg New York, ISSN 1617-7916, ISBN 978-1-84996-097-7 e-ISBN 978-1-84996-098-4.

[108] Cristianini, N. and Shawe-Taylor, J. , An Introduction to Support Vector Machines and Other Kernel-Based Learning Methods , Cambridge University Press, United Kingdom, , 2000 .

[109] S. Banerjee, P. S. Bhowmik, "Multiclass transient event classification in hybrid distribution network based on co-training of fine KNN and ensemble KNN classifier", Smart Science, Taylor & Francis, pp. 744-758, 2023.

[110] K Özcanlı, Asiye & Yaprakdal, Fatma & Baysal, Mustafa.. "Deep learning methods and applications for electrical power systems", A comprehensive review. International Journal of Energy Research. 2020.

[111] S. Wang, H. Chen, A novel deep learning method for the classification of power quality disturbances using deep convolutional neural network, Applied Energy, vol. 235, 2019, pp. 1126-1140, ISSN 0306-2619, 2018.

[112] M. Wei, W. Liu, H. Zhang, F. Shi and W. Chen, "Distortion-Based Detection of High Impedance Fault in Distribution Systems," in

IEEE Transactions on Power Delivery, vol. 36, no. 3, pp. 1603-1618, June 2021.

[113] S.Banerjee, P.S.Bhowmik (2023) A machine learning approach based on decision tree algorithm for classification of transient events in microgrid. Electrical Engineering, vol. 105, pp. 2083–2093.

[114] X. Liu, L. Xia, J. Shi, L. Zhang, L. Bai and S. Wang, "A Fault Diagnosis Method of Rolling Bearing Based on Improved Recurrence Plot and Convolutional Neural Network," in IEEE Sensors Journal, vol. 23, no. 10, pp. 10767-10775, 15 May, 2023.

[115] Zhao, *et al*, "Classification of multiple power quality disturbances based on CNN-BiLSTM-Attention", vol. 27, no. 7, pp. 2757—2766, November 2023.

[116] P. Rai, N. D. Londhe, R. Raj, "Fault classification in power system distribution network integrated with distributed generators using CNN", Electric Power Systems Research, vol. 192, 2021.

[117] B. B. Atitallah *et al.*, "Hand Sign Recognition System Based on EIT Imaging and Robust CNN Classification," IEEE Sensors Journal, vol. 22, no. 2, pp. 1729-1737, 15 Jan. 2022.

[118] A. Zhang, Q. Li, Z. Li and J. Li, "Multimodal Fusion Convolutional Neural Network Based on sEMG and Accelerometer Signals for Intersubject Upper Limb Movement Classification," IEEE Sensors Journal, vol. 23, no. 11, pp. 12334-12345, 1 June 2023.

[119] A. Bhattacharya *et al.*, "Deep feature selection using adaptive β-Hill Climbing aided whale optimization algorithm for lung and colon cancer detection", Biomedical Signal Processing and Control, vol. 83, 2023.

[120] Y. Gao *et al.*, "A Novel BILSTM-CNN Method for Pattern Recognition in Real Time Under Triple Physical Loads in Lower Extremity Exoskeleton," IEEE Sensors Journal, vol. 23, no. 14, pp. 15689-15701, July 2023.

[121] C. Xu *et al.*, "A Hybrid Model Integrating CNN–BiLSTM and CBAM for Anchor Damage Events Recognition of Submarine Cables," IEEE Transactions on Instrumentation and Measurement, vol. 72, pp. 1-11, 2023.

[122] Y. Keshun, Q. Guangqi and G. Yingkui, "A 3D Attention-enhanced Hybrid Neural Network for Turbofan Engine Remaining Life Prediction Using CNN and BiLSTM Models," IEEE Sensors Journal, 2023.

[123] Z. Zhang, *et al.*, "A probabilistic neural network assessment method for insulator pollution level based on discharge noise."

[124] International Energy Agency, Distributed generation in liberalized electricity market, 2002.

[125] S. Banerjee and P. S. Bhowmik (2023), "Multiclass transient event classification in hybrid distribution network based on co-training of fine KNN and ensemble KNN classifier", Smart Science, 2023.

[126] L. I. Dulău, Mihail Abrudean, Dorin Bică, "Effects of Distributed Generation on Electric Power Systems", Procedia Technology, vol. 12, pp. 681-686, 2014.

[127] M. Mishra, R. R. Panigrahi, and P. K. Rout, "A combined mathematical morphology and extreme machine learning techniques based approach to micro-grid protection," Ain Shams Engineering Journal, vol. 10, pp. 307-318, 2019.

[128] A. E. L. Rivas, and T. Abrão, “Faults in smart grid systems: Monitoring, detection, and classification. Electric Power Systems Research,” vol. 189, pp. 106602, 2020.

[129] S. R. Fahim, *et al*, “A Novel Wavelet Aided Probabilistic Generative Model for Fault Detection and Classification of High Voltage Transmission Line,” 2nd International Conference on Smart Power & Internet Energy Systems (SPIES), Bangkok, Thailand, pp. 94-99, 2020.

[130] M. A. Akhand, *et al*, “A Deep Learning through DBN Enabled Transmission Line Fault Transient Classification Framework for Multimachine Microgrid Systems,” International Transactions on Electrical Energy Systems. Vol. 2022, 2022.

[131] T. Chakravorti, *et al*, “A new robust kernel ridge regression classifier for islanding and power quality disturbances in a multi distributed generation based microgrid,” Renewable Energy Focus, Vol. 28, pp. 78-99, 2019.

[132] R. K. Beniwal,*et al*, “A Critical Analysis of Methodologies for Detection and Classification of Power Quality Events in Smart Grid,” IEEE Access, vol. 9, pp. 83507-83534, 2021.

[133] G. Jain, R. Ghosh and S. Dalai, " Identification of Power System Transients using Recurrence Plot Analysis"

[134] A. Amiri, H. Samet and T. Ghanbari, "Recurrence Plots Based Method for Detecting Series Arc Faults in Photovoltaic Systems," IEEE Transactions on Industrial Electronics, vol. 69, no. 6, pp. 6308-6315, June 2022,

[135] B. Cannas, *et al*, "Recurrence Plots for Dynamic Analysis of Type-I ELMs at JET With a Carbon Wall," IEEE Transactions on Plasma Science, vol. 47, no. 4, pp. 1871-1877, April 2019.

[136] J. Lu and K. -Y. Tong, "Robust Single Accelerometer-Based Activity Recognition Using Modified Recurrence Plot," IEEE Sensors Journal, vol. 19, no. 15, pp. 6317-6324, 1 Aug.1, 2019.

[137] A. L. Moraes and R. A. S. Fernandes, "Recurrence Plots: A Novel Feature Engineering Technique to Analyze Power Quality Disturbances," 2020 IEEE Power & Energy Society General Meeting (PESGM), Montreal, QC, Canada, pp. 1-5, 2020.

[138] Y. Hirata, "Recurrence plots for characterizing random dynamical systems", Communications in Nonlinear Science and Numerical Simulation, vol. 94, 2021, 105552,

[139] X. Liu, *et al*, "A Fault Diagnosis Method of Rolling Bearing Based on Improved Recurrence Plot and Convolutional Neural Network," IEEE Sensors Journal, vol. 23, no. 10, pp. 10767-10775, 15 May, 2023.

[140] M. A. Akhand, *et al*, "A Deep Learning through DBN Enabled Transmission Line Fault Transient Classification Framework for Multimachine Microgrid Systems," International Transactions on Electrical Energy Systems, vol. 2022, 2022.

[141] T. Chakravorti, *et al*, "A new robust kernel ridge regression classifier for islanding and power quality disturbances in a multi-distributed generation-based microgrid," Renewable Energy Focus, Vol. 28, pp. 78-99, 2019.

[142] R. K. Beniwal, *et al*, "A Critical Analysis of Methodologies for Detection and Classification of Power Quality Events in Smart Grid", IEEE Access, vol. 9, pp. 83507-83534, 2021.

[143] Z. Xu, *et al*, "A Boundary Aware WiFi Localization Scheme Based on UMAP and KNN", IEEE Communications Letters, vol. 26, no. 8, August 2022.

[144] J. An, *et al*, "Deep Clustering Bearing Fault Diagnosis Method Based on Local Manifold Learning of an Autoencoder Embedding", IEEE Access, February 2021.

[145] J. Chen, *et al*, Deep Reinforcement Learning Based Resource Allocation in Multi-UAV-Aided MEC Networks", IEEE Transaction on Communications, vol. 71, no. 1, January 2023.

[146] F. Trozzi, *et al*, "UMAP as a Dimensionality Reduction Tool for Molecular Dynamics Simulations of Biomacromolecules: A Comparison Study", Journal of Physical Chemistry B, 125, pp. 5022-5034, 2021.

[147] A.Jensen and A.la Cour-Harbo, Ripples in Mathematics: The Discrete Wavelet Transform, Springer, 2002.

[148] D. Sundararajan, Discrete Wavelet Transform: A Signal Processing Approach, Wiley, 2015.

[149] H. Demirel, "Discrete Wavelet Transform-Based Satellite Image Resolution Enhancement", IEEE Transactions on Geoscience and Remote Sensing, vol. 49, no. 6 June 2011.

[150] N. Y. Abed and O. A. Mohammed, "Modeling and Characterization of Transformers Internal Faults Using Finite Element and Discrete Wavelet Transforms", IEEE Transactions on Magnetics, vol. 43, no. 4, April 2007.

[151] A. Amiri, *et al*, "Recurrence Plots Based Method for Detecting Series Arc Faults in Photovoltaic Systems, IEEE Transactions on Industrial Electronics", vol. 69, no. 6, June 2022.

[152] B. Cannas, *et al*, "Recurrence Plots for Dynamic Analysis of Type-I ELMs at JET With a Carbon Wall",IEEE Transactions on Plasma Science, vol. 47, no. 4, April 2019.

[153] J. Lu, *et al*, "Robust Single Accelerometer-Based Activity Recognition Using Modified Recurrence Plot", IEEE Sensors Journal, vol. 19, no. 15, August 1, 2019.

Chandan Jana Chandan Jana

Signature of the Candidate : ----------

(Author's Name)

Date : 24.06.2025.